Contrasting Features and Volcanostratigraphy of the Mafic-Hosted Mandoos and Shinas Volcanogenic Massive Sulfide Deposits, Samail Ophiolite, Oman

André Cravinho, Ana Jesus, Bruno Moreira, António Mateus, Bernhard Pracejus, Jorge Figueiras, Mathieu Benoit, Wilfried Bauer, Fernando Rocha

Economic Geology, v. 118, no. 5, pp. 1085–1124

Contrasting Features and Volcanostratigraphy of the Mafic-Hosted Mandoos and Shinas Volcanogenic Massive Sulfide Deposits, Samail Ophiolite, Oman

André Cravinho,[1,†] Ana P. Jesus,[1] Bruno Moreira,[2] António Mateus,[1] Bernhard Pracejus,[3] Jorge Figueiras,[1] Mathieu Benoit,[4] Wilfried Bauer,[5] and Fernando Rocha[6]

[1]*University of Lisbon, Faculdade de Ciências, Instituto Dom Luiz (IDL), Campo-Grande, Lisbon 1749-016, Portugal*

[2]*Lusorecursos Portugal Lithium Rua Direita, 30, Montalegre 5470-245, Portugal*

[3]*Earth Science Department, Sultan Qaboos University, P.O. Box 36, 123 Al-Khoud, Muscat, Oman*

[4]*Université de Toulouse, Géosciences Environnement Toulouse-Observatoire Midi-Pyrénées (GET-OMP), Université Paul-Sabatier- Centre national de la recherche scientifique - Institut de Recherche pour le Développement (CNRS-IRD), 14 avenue Edouard Belin, Toulouse 31400, France*

[5]*Applied Geosciences (AGEO) Department, GUtech: German University of Technology in Oman, P.O. Box 1816, Athaibah 130, Oman*

[6]*Geobiotec, Departamento de Geociências, Universidade de Aveiro, Aveiro 3810-193, Portugal*

Abstract

Despite the substantial amount of research on the Cretaceous Samail ophiolite in Oman, the factors controlling the size and metal endowment of the mafic-hosted, Cu-Au(-Zn-Ag) volcanogenic massive sulfide (VMS) deposits remain elusive. This work shows that the volcanostratigraphic position, hydrothermal venting style, and oxidation processes are critical factors controlling the distinct features of the Shinas and Mandoos deposits.

Mandoos is a large (8 Mt, 1.8 wt % Cu, 0.18 g/ton Au) orebody preserving abundant primary vent-related features formed via mound growth and collapse within a wide hydrothermal field, overlying a poorly developed stockwork. The smaller Shinas deposit (0.8 Mt, 2.6 wt % Cu, 0.63 g/t Au) represents a higher-temperature system evolving from low fS_2/fO_2 conditions, locally sealed by jaspers, to a mound growth stage with widespread subseafloor brecciation/replacement with associated zone refining. Mandoos formed at the onset of the postaxial stage (Geotimes-Tholeiitic Alley transition), and Shinas is hosted within the Alley units. Volcanism in Samail was seemingly continuous, and the low ε_{Nd} and Nb/Ta of the Shinas hanging-wall lavas record the onset of significant modifications of the mantle source during the postaxial stage.

Mandoos is enriched in Te + As + Se ± Zn ± Ga ± Sb relative to Shinas, where higher Cu + Au + Tl ± Mo grades possibly reflect leaching of protoarc-like lavas. Rare earth element patterns in the ores mimicking the deposit footwall can be employed to constrain volcanostratigraphic positioning and indicate that the footwall lavas may also represent a source of metals. Formation of metal-rich ochres at the sea floor likely led to Cu + Au upgrading in the ores during seawater-induced oxidation, which was enhanced during subaerial gossan formation.

Introduction

The Samail ophiolite is one of the most outstanding expressions of the Tethyan ophiolite belt and hosts a world-class, mafic- or Cyprus-type volcanogenic massive sulfide (VMS) province (Galley and Koski, 1997), in a volcanic belt three times larger than the one in the Troodos ophiolite. During the 1980s, several deposits were mined for copper and gold. Since 2009, the use of airborne Versatile Time Domain Electromagnetic (VTEM) geophysical surveys boosted the number of discoveries concealed under postobduction sediments.

There are 17 mined-out deposits in the northern sector of the Samail ophiolite, mostly distributed along the Batinah coast and two (Al Bishara and Rakka) in the western domain (Fig. 1A). The known VMS deposits contain 50 Mt sulfide ores with an average grade of 2.3 wt % Cu and 0.4 g/ton (t) Au (Gilgen et al., 2014). The recent discovery of the Al Hadeetha deposit adds 9.7 Mt at 0.88% Cu and 0.22 g/t Au to Oman's portfolio (Fig. 1A).

†Corresponding author: e-mail, acravinhosantos@gmail.com

The volcanostratigraphy of the Samail ophiolite (Fig. 1A) has been the focus of numerous investigations. The importance of locating the orebodies within the extrusive sequence was recognized early (Alabaster and Pearce, 1985) and has been revised by Gilgen et al. (2014). The stratigraphic level identified to have the highest potential corresponds to the transition between the first volcanic stage (V1, Geotimes unit) and the overlying volcanic units (V2, Lasail and Tholeiitic/Boninitic Alley units; Alabaster et al., 1982; Ernewein et al., 1988). However, every volcanic quiescence period can potentially host a VMS deposit (Gilgen et al., 2014). Deposit tonnage does not vary systematically with volcanostratigraphic position, but higher Cu grades occur in orebodies hosted within the V1 stage and V1/V2 transition, whereas higher Au grades are associated with deposits hosted in the uppermost V2 protoarc-like Boninitic Alley unit (Gilgen et al., 2014). Such observations are consistent with the known association of high gold concentrations in sea-floor massive sulfides (SMS; Hannington et al., 2011) hosted in arc settings (Herzig and Hannington, 1995). Higher Au grades can result from leaching of Au-rich volcanic rocks, hydrothermal

ISSN 0361-0128; doi:10.5382/econgeo.5006; 40 p.
Digital appendices are available in the online Supplements section.

Submitted: March 14, 2022 / Accepted: October 7, 2022

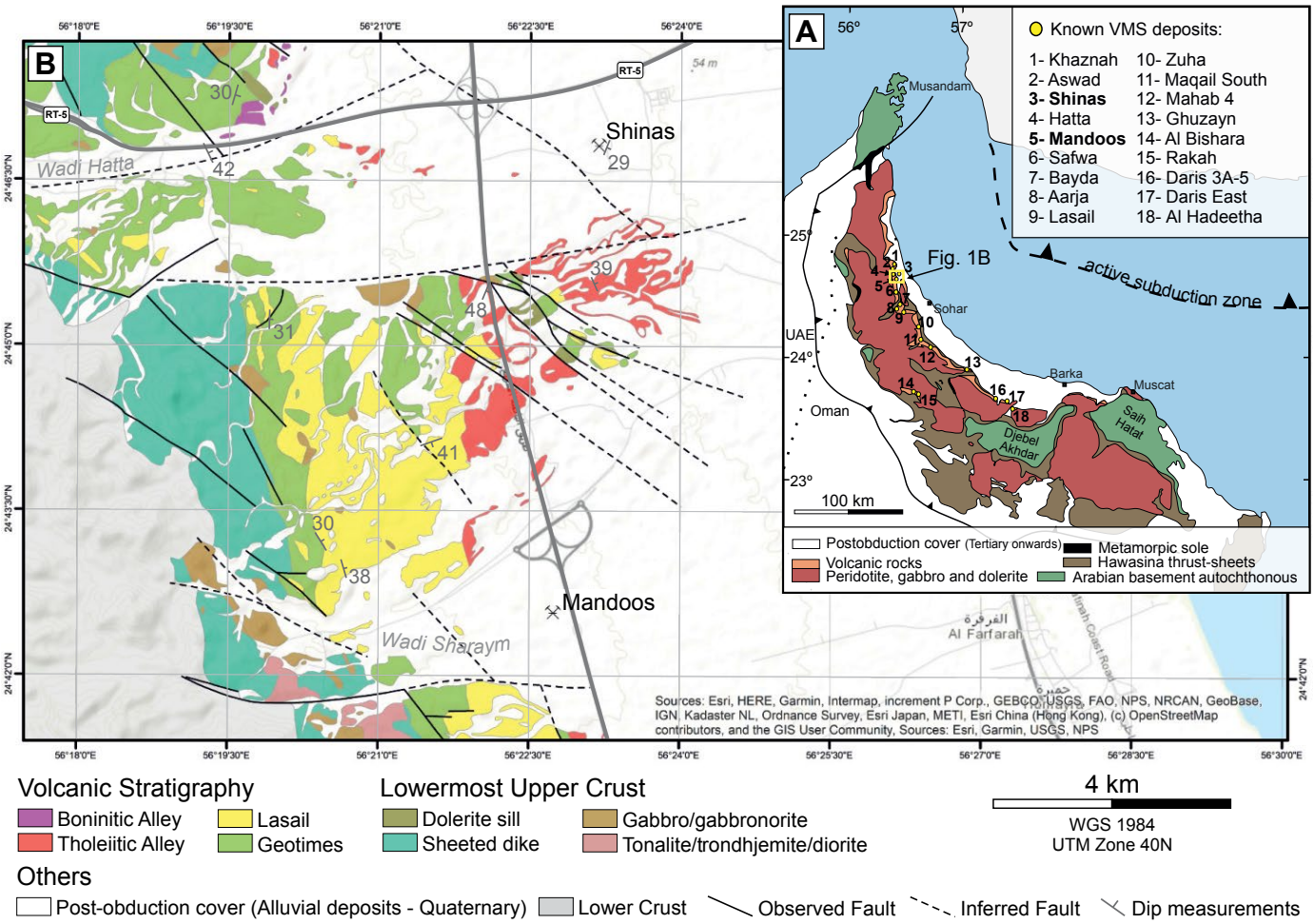

Fig. 1. (A) Main units of the Samail ophiolite and volcanogenic massive sulfide (VMS) deposits (adapted from Gilgen et al., 2014). (B) Geologic map of the Fizh block showing the location of the Mandoos and Shinas VMS deposits (adapted from Belgrano et al., 2019).

fluids boiling close to the sea floor, or magmatic degassing processes (Huston, 2000; Mercier-Langevin et al., 2011; Fuchs et al., 2019). However, the high water depths postulated for the extrusion of the Samail lavas preclude boiling of the hydrothermal fluids (>3,000 m; Belgrano et al., 2021), whereas high-sulfidation mineral assemblages are only reported as tennantite in the Aarja deposit (Haymon et al., 1984, 1989; Ixer et al., 1984). Mineralogical and geochemical data of ochres and gossans from the Oman VMS deposits are also crucial to distinguish upgrading of base metal and gold concentrations by supergene (Boyle, 2003) and seawater-induced oxidation processes (Herzig et al., 1991; Hannington et al., 1998).

Studies on VMS deposits in the Samail ophiolite are essentially restricted to the mineralogy of the Aarja, Lasail, and Bayda orebodies (Ixer et al., 1984). Data on the deposits discovered after 2000 are noticeably lacking, considering the amount of research focused on the magmatic, geodynamic, and hydrothermal history of the Samail ophiolite. Mafic-type VMS deposits are thought to have been formed in black smoker sulfide mounds, similar to present-day SMS (Ixer et al., 1984). Based on the absence of breccia-dominated ores in the Aarja deposit, some authors argued against a sulfide-mound model and suggested that the Oman VMS deposits formed in reduced anoxic basin settings (Hannington et al., 1998). Such uncertainties stem from the lack of detailed and updated studies on the formation and evolution of other VMS deposits in Oman.

The Mandoos and Shinas deposits (Fig. 1B) were discovered through airborne VTEM surveys and mined by Mawarid Mining LLC until 2015 and 2011, respectively. Mandoos is one of the largest deposits in Oman with reported resources (Gilgen et al., 2014) of 6.73 Mt at average 1.66 wt % Cu, 0.15 g/t Au, along with Lasail or Al Ghuzayn-3 and Al Hadeetha, which are under development. Shinas is a small (~1 Mt) high-grade deposit (2 wt % Cu, 0.17 g/t Au) within the size range of most Omani VMS deposits. Based on whole-rock and pyroxene chemistry, Gilgen et al. (2014) suggested that both deposits are hosted within the Alley unit. The hanging wall of the Shinas deposit was subsequently assigned to a transitional Tholeiitic-Boninitic Alley unit (Belgrano et al., 2019). These deposits are thus ideal targets to unravel the influence of the depleted, hydrous magmatism on VMS formation. The deposit's dissimilar size, lithological features, and metal endowments enable refinement of metallogenic models and assessment of the relative influ-

ence of the source rocks versus local ore-forming conditions (e.g., venting styles, subsurface hydrologic features) on hydrothermal and mineralization processes. Both deposits were affected by postmineralization oxidation that led to important metal enrichments, the timing of which is unclear. Constraining both late and primary genetic features can provide support to ongoing exploration activities in the Samail ophiolite. We present a comprehensive study that includes mineralogical (petrography, mineral chemistry, X-ray diffraction [XRD]) and geochemical data (major and trace elements, Sr-Nd isotopes) on the lithological spectrum of the hanging-wall and footwall volcanic sequence, massive sulfide ores, jaspers, ochres, and umbers. Additionally, a large data set of mining assays enables assessment of 3-D base metal distributions at the deposit scale.

Geologic Background

The Cretaceous Samail ophiolite is part of the Mesozoic Neo-Tethyan ophiolite belt (Dilek and Furnes, 2011). The ophiolite is gently folded and preserves most of the primary structures and contacts, including a thick mantle and lower crustal section with layered, foliated gabbro and discontinuous isotropic/high-level gabbros, which correspond to the axial melt lens where the sheeted-dike complex is rooted (Nicolas et al., 2000; Goodenough et al., 2014). The sheeted dikes represent the magmatic feeders of the volcanic upper crustal section, which is broadly divided in two main stages (Ernewein et al., 1988), V1 and V2, locally covered by Cenomanian-Turonian pelagic sediments (93.9 Ma; Fleet and Robertson, 1980). A third magmatic series, V3 (Godard et al., 2003), covering pelagic sediments, is restricted to the north.

The nomenclature of the volcanic sequence varies according to different authors. In this work we follow the revised volcanostratigraphic scheme proposed by Gilgen et al. (2014) and Belgrano et al. (2019) and use GB1/GB2 for axial and postaxial intrusives. The extrusive section is divided into four units, detailed descriptions of which can be found in Belgrano et al. (2019). The Geotimes unit corresponds to the voluminous V1 axial stage, and the Lasail and the two Alley units form the V2 off-axial stage (Ernewein et al., 1988; Godard et al., 2003), although the eruption of Lasail lavas began during the early stages of axial volcanism, thus representing the transition from V1 to V2 stages (Belgrano and Diamond, 2019). The V3 unit comprises transitional to alkaline flows and likely represents preobduction intraplate magmatism (Alabaster et al., 1982; Ernewein et al., 1988). All units, except the Boninitic Alley, present tholeiitic features and show increasing depletion in incompatible elements (particularly Ti, Nb, and Ta) toward the top of the sequence. Alteration effects in the volcanic units range from zeolite to greenschist facies assemblages.

The crustal intrusive units referred above (GB1) are intruded by late magmatic bodies (GB2; Benoit et al., 1996, 1999; Nicolle et al., 2016), which, like the V2 volcanic sequence, show depletion in incompatible elements, high-Mg, and hydrous character.

The significance of the two magmatic stages has led to considerable debate regarding the geodynamic setting of the Samail ophiolite. The V1/GB1 magmatism represents the crustal accretion stage, generated at a mid-ocean ridge (MOR)-like spreading center, whereas the interpretation of V2/GB2 magmatism is historically controversial, representing either (1) a protoarc setting developed above a shallow subduction zone, as proposed for most Tethyan ophiolites (Alabaster et al., 1982; Ishikawa et al., 2005; Goodenough et al., 2014; Kusano et al., 2014), or (2) second-stage melting of the V1/GB1 mantle source, modified by deep hydrothermal fluid circulation during intraoceanic thrusting (Ernewein et al., 1988; Benoit et al., 1996, 1999; Einaudi et al., 2000; Godard et al., 2006; Nicolle et al., 2016). Furthermore, recent data suggest that the magmatic evolution of the Samail differs from a typical MOR setting since its earliest stages. Significantly, the hydrous nature of axial magmatism, together with mild Nb-Ta negative anomalies and Ba enrichments, in comparison to typical MORB, suggests a subduction initiation setting, which evolved to the typical oceanic-arc geochemical signatures of V2/GB2 (MacLeod et al., 2013; Kusano et al., 2017). Available U-Pb zircon data from plagiogranitic and gabbroic rocks also support the formation of oceanic crust in two main stages: 96.1 to 95.6 and 95.6 to 95.2 Ma (Rioux et al., 2021).

The Mandoos and Shinas deposits herein studied are located in the northern Fizh block, beneath the gravels of Wadi Sharaym and Wadi Hatta, respectively (Fig. 1B).

Sampling and Analytical Techniques

Grab samples were collected in the Mandoos open pit shortly after mining operations ceased (profiles in Fig. 2). The main set of samples was retrieved from exploration drill cores (Shinas = 3, Mandoos = 6), offered to GUtech by Mawarid LLC, relogged, and sampled; sample labeling in Mandoos (MD) and Shinas (SH) drill cores is followed by downhole depth. Samples were characterized macroscopically, and representative portions were selected for thin sections or polished mounts and whole-rock geochemistry analyses: hanging-wall and footwall (Mandoos = 40, Shinas = 19), jaspers (Mandoos = 2, Shinas = 2), ochres (Mandoos = 42, Shinas = 3), umbers (Mandoos = 4), gossan (Shinas = 1), and ores (Mandoos = 10, Shinas = 6). For Shinas heterogeneous footwall breccias, quarter cores <20 cm long were processed. Surfaces were abraded with emery or SiC before coarse crushing in a hardened steel roll mill and pulverizing in agate mills.

Deposit modeling

Base metal 3-D modeling of the orebodies was made using the Micromine-2014 software. For Mandoos, data represent 33 drill cores: 29 on a 50- × 50-m square grid in the open-pit area, one ~1 km to the north, and three ~250 m to the southeast. The Shinas deposit was modeled with data from 175 drill cores, irregularly spaced. The open-pit design of both deposits and orebody shape and cross sections of Mandoos were provided by Mawarid LLC. The Shinas orebody shape was obtained by the authors, using the "Vein" and "Grade" functions, merging the mine units "massive sulfide" and "silica massive sulfide." This allowed computing the spatial distribution of Cu and Zn grades. The thresholds used to define the color-coded cutoff grades were the statistical values for minimum, first quartile, median, and third quartile. Due to the low Zn grades in Shinas, two thresholds were sufficient, and one maximum outlier was discarded.

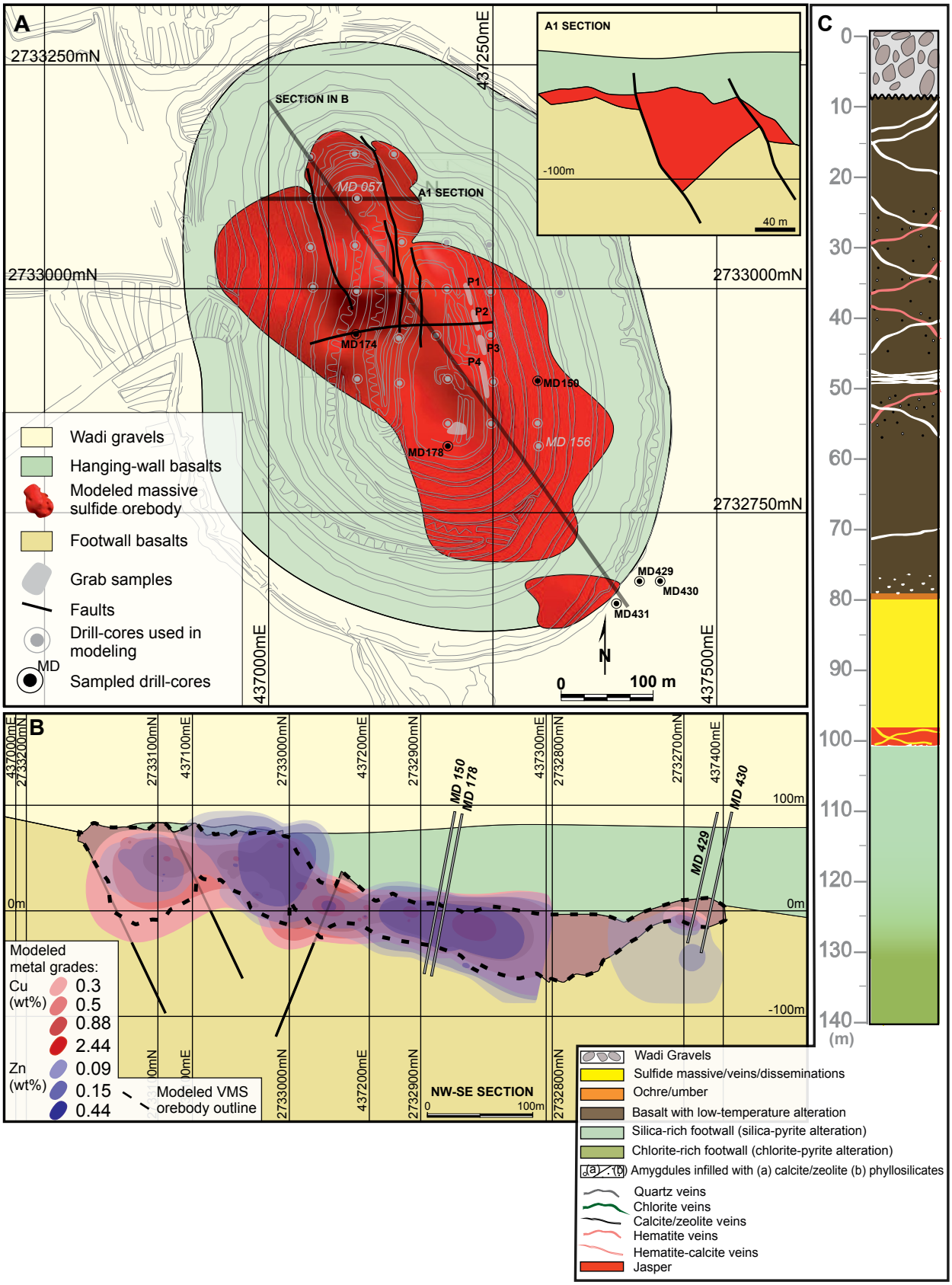

Fig. 2. Geology of the Mandoos deposit. (A) Location of the drill cores used for modeling and sampling. (B) Cross section with projected Cu and Zn mine assay modeled grades. (C) Lithostratigraphic column based on this work's logging. VMS = volcanogenic massive sulfide.

Mine assay data

The lithological classification of assayed intervals for the ores, jaspers, Fe sediments (umber + ochres), and gossans followed those reported by Mawarid LLC. Basalts were further discriminated into hanging wall and footwall with respect to the ore lens or to gossans and Fe sediment layers, which mark the ore horizon. Assayed intervals are 1 m in length, occasionally longer for hanging-wall basalts, and tighter for Fe sediments and ores to avoid sampling multiple rock types in a single analysis. Samples were analyzed by atomic absorption (AAS-55B Agilent) at the Mawarid in-house lab of the copper concentrator plant in Sohar. Random duplicates were regularly sent to SGS Oman for quality assurance/quality control (QA/QC) certification.

A total of 1,563 and 10,596 assayed intervals for Fe, Cu, Zn, Au, and Ag concentrations were processed for Mandoos and Shinas, respectively. Arsenic, Mn, and Cd concentrations are additionally available at Shinas, where some detection limits (Au and Ag) are slightly lower. Mineral volume percents estimated considering average base metal concentrations are presented in Table 1, as well as the different ore-type proportions in each deposit (Mandoos = 100% massive sulfide; Shinas = 63% silica massive sulfide + 37% massive sulfide). Calculations were made as follows: (1) Cu grades were used to calculate chalcopyrite volume percent, to which a proportional amount of Fe was allotted; (2) Zn grades were used to estimate the proportion of sphalerite; (3) the remaining Fe wt % was assigned to pyrite and the remainder modal volume to quartz volume percent.

Electron probe microanalyzer (EPMA)

Mineral chemistry data were obtained from polished thin sections and mounts, covered in 20-nm-thick carbon coatings, at the Insituto Dom Luiz–Faculdade de Ciências da Universidade de Lisboa (IDL-FCUL) using a JEOL-JXA 8200 microprobe equipped with four wavelength-dispersive spectrometers (WDS), six analyzing crystals (LIF, LIFH, PET, PETH, TAP, and LDED2), plus secondary and retrodiffused electron detectors coupled to an energy-dispersive spectrometer (EDS). Measurements were made with a 20-s acquisition time for the peaks and 5 s for the background. The accelerating voltage was 15 kV with a current beam of 25 nA and a beam spot diameter of 5 µm. Natural mineral and metallic standards were used, provided by Astimex Scientific Ltd. The standard analytical errors (2σ) are ~2% relative to major elements; for sulfides see Appendix 1. Representative chemical analyses of all mineral phases are reported in Table 2 and Appendix 1.

X-ray diffraction (XRD)

Selected domains were sampled with a microdrill, whereas whole-rock powders were used to identify the phyllosilicates in the lavas. Twenty-six samples were processed at IDL-FCUL with a Rigaku MiniFlex II diffractometer using Cu Kα radiation with an output voltage and current of 30 kV and 15 mA, a graphite crystal monochromator, and a detector with a NaI(T1) scintillator and a Be window. Samples were scanned in the 3° to 90° range with 0.02° steps in continuous mode at a 0.40°/min rate. Data reduction and mineral identification was performed with QualX software (Altomare et al., 2008).

X-ray fluorescence (XRF)

Whole-rock major elements and base metal concentrations (Si, Al, Mg, Na, K, P, S, Ca, Ti, Mn, Fe, Cu, and Zn) were determined at Geobiotec using an Axios PANalytical spectrometer equipped with an Rh tube, argon/methane gas, and IQ+ processing program. Loss on ignition (LOI) was determined for nonmineralized (hanging-wall) rocks by heating 1 g of sample at 1,000°C for 1 h in a furnace.

Inductively coupled plasma-mass spectrometry (ICP-MS)

Whole-rock trace element concentrations were obtained using an HR-ICP-MS ELEMENT XR at Géosciences Environnement Toulouse-Observatoire Midi-Pyrénées (GET-OMP), following the procedure reported in Barrat et al. (2007). Sample preparation consisted of an HF-$HClO_4$ digestion procedure (Yokoyama et al., 1999) combined with a thulium (Tm) addition (Barrat et al., 1996). The Tm addition allowed the calculation of trace element compositions based on the Tm positive anomaly in rare earth element (REE) patterns. Therefore, there is no correction for any elemental loss during the chemical procedure. Following digestion, samples were diluted and analyzed to obtain all trace element concentrations. BHVO-2 was used as external standard following Barrat et al. (2007). The yield was monitored and concentrations calculated using the Tm anomaly (Barrat et al., 1996). MG-PMS and UBN geostandards were measured using the same procedure. Analytical blanks were systematically subtracted to BHVO-2 and sample counts per second (cps).

Nd-Sr isotopes

Isotopic data were obtained at GET-OMP: 100 mg of whole-rock powder was weighed in a Teflon beaker and dissolved in an HF/HNO_3/HCl 2:1:1 mixture. Neodymium and Sr were extracted from the matrix using a combination of Sr-Spec, Thru-Spec, and Ln-Spec resins. An equivalent of 500 ng Sr and 150 ng Nd were run on a MAT261 Finnigan mass spectrometer, except Shinas samples, which were measured on a TRITON+ Thermo-Scientific mass spectrometer following the protocols of C.F. Li et al. (2011, 2012) after Sr and REE purification. NBS987 and La Jolla isotopic standards were regularly run during measurements. Standard reproducibility is 0.510855 ± 18 (n = 50) for La Jolla and 0.710250 ± 35 (n = 70) for NBS987. Typical blanks are 50 pg for Nd and 150 pg for Sr.

Geology of the Mandoos Deposit

Orebody morphology and base metal distribution

The Mandoos orebody is unconformably overlain by 4- to 34-m-thick fluvial carbonate-cemented gravels (*wadi* gravels). The SE-dipping orebody extends for a length of ~550 m and a maximum width of 370 m. The thickness of the lenticular orebody ranges from 1 to 90 m and is locally controlled by a set of north-south to northwest-southeast faults, dipping 55° to 70° to the east-northeast, generating a half-graben paleotopography (Fig. 2A; Apps. 2, 3).

Considering the main sulfide phases known to occur in the massive sulfides, a calculated mineralogy based on the Fe, Cu, and Zn assay average concentrations in massive sulfides indicates a composition of 83 vol % pyrite, 11 vol % quartz, 5.4 vol % chalcopyrite, and 0.9 vol % sphalerite, consistent

Table 1. Mine Assay Data Statistical Parameters

	Mandoos						Shinas									
Jasper	Cu	Zn	Fe	Au	Ag		Cu	Zn	Pb	Fe	Au	Ag	As	Mn	Cd	Cr
n = 2	(wt %)	(wt %)	(wt %)	(µg/g)	(µg/g)	n = 16	(wt %)	(wt %)	(wt %)	(wt %)	(µg/g)	(µg/g)	(µg/g)	(µg/g)	(µg/g)	(µg/g)
Min	0.45	0.06	17.2	0.06	2.5	Min	0.004	0.01	0.0001	0.7	0.01	0.1	5	68	0.3	6
Max	4.38	0.20	28.6	0.23	8.0	Max	0.13	0.02	0.082	12.7	0.64	3.4	366	311	0.3	66
Average						Average	0.04	0.01	0.006	4.7	0.20	1.0	68	136	0.3	24
Median						Median	0.02	0.01	0.001	2.2	0.13	0.7	42	111	0.3	14
Stand dev						Stand dev	0.04	0.00	0.020	4.0	0.19	1.0	86	71	-	21
Fe sediment (umbers + ochres)																
n = 25						n = 277										
Min	0.01	0.01	4.9	0.01	2.3	Min	0.01	0.01	0.000	0.6	0.01	0.1	4	50	0.3	3
Max	0.28	0.14	48.8	0.14	12.0	Max	7.70	1.75	0.025	43.3	5.25	84.9	866	37,900	23.4	235
Average	0.07	0.03	24.2	0.03	3.1	Average	0.27	0.07	0.006	11.7	0.10	2.8	81	6,844	1.8	49
Median	0.06	0.03	22.4	0.01	2.5	Median	0.03	0.03	0.005	9.8	0.01	2.5	60	3,895	0.3	23
Stand dev	0.06	0.04	13.2	0.03	2.2	Stand dev	0.72	0.14	0.006	5.9	0.50	7.4	107	8,097	3.8	58
Gossan																
n = 10						n = 296										
Min	0.01	0.01	6.3	0.01	2.5	Min	0.001	0.01	0.000	0.9	0.01	0.1	3	10	0.3	3
Max	0.01	0.04	17.6	0.05	2.5	Max	10.95	0.57	0.215	50.0	11.70	100.0	1,960	15,900	271.0	407
Average	0.01	0.01	13.1	0.01	2.5	Average	0.37	0.04	0.007	11.5	0.88	6.9	168	533	3.1	63
Median	0.01	0.01	14.7	0.01	2.5	Median	0.09	0.01	0.002	8.1	0.34	2.5	74	107	0.3	42
Stand dev	0.00	0.01	3.9	0.01	-	Stand dev	0.97	0.07	0.021	10.9	1.49	13.0	269	1,627	19.7	73
Silica massive sulfide																
n = 6						n = 417										
Min	0.16	0.19	27.5	0.01	2.5	Min	0.01	0.01	0.000	3.3	0.03	0.3	8	8	0.3	1
Max	1.23	1.09	37.4	0.01	2.5	Max	15.32	3.29	0.029	30.6	3.53	101.0	466	2,520	164.5	453
Average	0.51	0.42	31.5	0.01	2.5	Average	2.24	0.17	0.006	17.5	0.55	8.8	135	127	7.5	43
Median	0.39	0.26	31.2	0.01	2.5	Median	1.63	0.05	0.005	18.0	0.43	7.2	126	63	1.8	26
Stand dev	0.39	0.35	3.7	-	-	Stand dev	2.35	0.31	0.003	6.1	0.47	7.6	67	218	16.8	59
Massive sulfide																
n = 349						n = 249										
Min	0.01	0.01	0.0	0.01	2.5	Min	0.01	0.01	0.000	4.4	0.01	0.1	1	8	0.3	1
Max	33.92	11.12	50.8	2.12	129.0	Max	25.40	3.11	0.038	39.6	4.41	73.0	460	5,190	127.0	254
Average	1.82	0.59	39.7	0.18	11.6	Average	3.07	0.43	0.009	25.9	0.76	14.0	198	189	19.1	27
Median	0.80	0.14	40.8	0.06	8.0	Median	2.08	0.20	0.009	27.0	0.60	10.9	188	57	9.3	10
Stand dev	2.64	1.31	6.7	0.30	13.5	Stand dev	3.51	0.52	0.005	5.5	0.59	11.1	78	576	22.9	40

Table 1. (*Cont.*)

Hanging-wall volcanic rocks													
n = 279					n = 609								
Min	0.01	0.01	1.7	0.01	2.5	Min	0.00	0.01	0.000	2.8	0.01	0.1	1	50	0.3	5
Max	5.89	1.29	41.2	0.90	39.0	Max	9.25	2.71	0.032	50.0	1.46	29.1	1,115	13,100	76.0	293
Average	0.05	0.04	8.2	0.02	2.8	Average	0.11	0.04	0.002	7.2	0.03	2.2	25	2,235	4	35
Median	0.01	0.01	6.6	0.01	2.5	Median	0.01	0.01	0.000	6.7	0.01	2.5	5	1,580	1	23
Stand dev	0.36	0.11	5.2	0.07	3.0	Stand dev	0.61	0.13	0.004	3.5	0.10	2.1	100	2,155	10	47
Footwall volcanic rocks																
n = 822						n = 5,090										
Min	0.01	0.01	0.0	0.01	2.5	Min	0.002	0.01	0.000	0.0	0.01	0.1	1	10	0.3	1
Max	7.15	10.53	50.1	4.83	77.0	Max	15.00	2.12	0.036	34.6	6.48	97.9	511	46,800	191.0	384
Average	0.20	0.15	14.3	0.03	3.5	Average	0.32	0.05	0.001	9.1	0.07	1.7	30	999	3	17
Median	0.03	0.02	12.0	0.01	2.5	Median	0.05	0.01	0.001	8.0	0.02	2.2	17	815	0	8
Stand dev	0.60	0.55	7.7	0.18	4.6	Stand dev	0.79	0.11	0.002	3.9	0.19	2.2	37	1,286	8	29
						Orebody weighted average = 63% Si massive sulf + 37% massive sulf										
						n = 666										
						Average	2.55	0.27	0.007	20.61	0.63	10.7	158	150	11.8	36.9

Note: Dashes indicate no standard deviation could be calculated

with petrographic observations. Considering the orebody volume provided by Mawarid Mining LLC, a total of 8 Mt of massive sulfides is calculated at an average Cu = 1.8 wt % and Zn = 0.6 wt %, using the 0.3 wt % Cu cutoff grade. The orebody was not completely mined, and there may be potential for underground mining. The northern area of the open pit corresponds to the thickest domain of sulfide ore (~90 m) and is bounded by northwest-southeast to north-south faults. Other sulfide accumulations occur along the northeast-southwest axis (~5 m) and at the southeast distal area (<5 m). The thickest ore domain does not correlate with the highest Cu-Zn grades, which are found toward the center of the open pit (Fig. 2; Apps. 2, 3). Copper- and Zn-rich domains mostly overlap except to the southeast of the thickest sulfide accumulation, where the ores are Cu rich but Zn poor (Fig. 2B; Apps. 2, 3).

Massive sulfide mineralization, jaspers, ochres, and umbers

Massive sulfide ores from Mandoos are mostly composed of heterometric (mm to cm), poorly sorted sulfide breccias, where jigsaw-fit-like textures are locally preserved (Fig. 3A, B). The sulfide breccias are cemented by quartz, carbonate, chlorite, fine-grained pyrite and chalcopyrite, and rare laumontite. Ore mineralogy is dominated by pyrite and marcasite (≈80 vol %) with variable amounts of chalcopyrite and sphalerite, Cu-rich phases (e.g., bornite, spionkopite), and traces of galena. Several features preserved within the breccia clasts represent pristine hydrothermal textures, namely (1) pyritized tube-worm sections (Fig. 4A), (2) framboidal pyrite aggregates (≤100 µm), usually enclosed by idiomorphic pyrite + chalcopyrite and less commonly by sphalerite or Cu-rich sulfides (Fig. 4B, C, E), and (3) banded (Fig. 4D), colloform, or euhedral laths comprising pyrite, marcasite (Fig. 4F), and Cu-rich sulfides with marcasite and sphalerite inclusions. Primary pyrite-rich textures are often recrystallized to coarse-grained crystals where the growth zoning is outlined by alternating porous/recrystallized domains, sphalerite or marcasite inclusions, and brecciated chalcopyrite (Fig. 4C, E). Marcasite occurs as large, bladed crystals in pyrite-rich samples (Fig. 4F). Textures in sphalerite and chalcopyrite-rich ores comprise euhedral wurtzite replaced by sphalerite with chalcopyrite inclusions (Fig. 4G) and sphalerite masses with oriented chalcopyrite intergrowths; open spaces are infilled by idiomorphic and massive pyrite. Galena occurs sparsely as small inclusions in sphalerite and pyrite. Early formed Fe-Cu sulfides (e.g., cubanite) are replaced by chalcopyrite. Chalcopyrite is locally replaced by bornite (Fig. 4C, G) and spionkopite. Rare Mn-rich jasper clasts comprise euhedral pyrolusite in a cryptocrystalline silica matrix crossed by romanechite veins.

The ores are locally altered to ochres (Fig. 3D) displaying breccia-like textures reminiscent of the sulfide breccias: clasts of hematite and goethite (replacing pyrite aggregates) are cemented by a cryptocrystalline silica-rich matrix with finely disseminated goethite and hematite (Fig. 4H). Relic chalcopyrite is occasionally replaced by spionkopite and bornite, and atacamite fills vugs with Fe hydroxides (Fig. 4I). XRD analyses also indicate the presence of jarosite.

The massive sulfides are locally interbedded with metalliferous mudstones (umbers; Fig. 3C, E), which comprise layers of fine-grained phyllosilicates and Fe (oxy)hydroxides. Close

Table 2. Electron Probe Microanalyses of Sulfides from the Mandoos and Shinas Deposits (wt %)

Mandoos

Pyrite n = 309

	S	Fe	Cu	Zn	Pb	Co	Mn	As	Au	Ag	Se	In	Sb	Σ
Min	47.82	41.09	<0.03	<0.06	<0.06	<0.02	<0.02	<0.02	<0.02	<0.02	<0.02	<0.03	<0.03	97.06
Max	54.05	47.07	8.98	2.79	0.71	0.84	0.64	0.57	0.07	0.45	0.27	0.10	0.10	101.1
Average	52.92	45.97	0.37	0.14	<0.06	0.03	0.03	0.03	<0.02	<0.02	<0.02	<0.03	<0.03	99.68
Median	53.10	46.25	<0.03	<0.06	<0.06	<0.02	<0.02	<0.02	<0.02	<0.02	<0.02	<0.03	<0.03	99.83
Std Dev	0.69	0.85	1.03	0.37	0.08	0.06	0.08	0.07	<0.02	0.03	0.03	<0.03	<0.03	0.74

Marcasite

	S	Fe	Cu	Zn	Pb	Co	Mn	As	Au	Ag	Se	In	Sb	Σ
Min	51.27	42.93	<0.03	<0.06	<0.06	<0.02	<0.02	<0.02	<0.02	<0.02	<0.02	<0.03	<0.03	97.84
Max	53.87	46.91	3.98	0.98	0.39	0.08	1.37	0.47	0.10	0.06	0.05	0.08	0.05	101.1
Average	53.03	45.99	0.18	0.08	<0.06	<0.02	0.07	0.02	<0.02	<0.02	<0.02	<0.03	<0.03	99.56
Median	53.13	46.15	<0.03	<0.06	<0.06	<0.02	<0.02	<0.02	<0.02	<0.02	<0.02	<0.03	<0.03	99.60
Std Dev	0.46	0.61	0.49	0.16	0.06	<0.02	0.20	0.05	0.02	0.02	0.01	0.02	0.01	0.65

Chalcopyrite

	S	Fe	Cu	Zn	Pb	Co	Mn	As	Au	Ag	Se	In	Sb	Σ
Min	32.60	26.83	31.61	<0.06	<0.06	<0.03	<0.02	<0.02	<0.03	<0.03	<0.02	<0.03	<0.03	97.41
Max	36.43	32.59	38.14	5.03	0.27	0.21	0.11	0.07	0.07	0.07	0.10	0.10	0.10	101.6
Average	34.86	30.20	34.20	0.44	<0.06	<0.03	<0.02	<0.02	<0.03	<0.03	0.02	<0.03	<0.03	99.94
Median	34.93	30.33	34.30	0.09	<0.06	<0.03	<0.02	<0.02	<0.03	<0.03	<0.02	<0.03	<0.03	100.2
Std Dev	0.37	0.61	0.91	0.76	<0.06	0.04	0.02	0.02	<0.03	<0.03	0.02	<0.03	<0.03	0.84

Sphalerite

	S	Fe	Cu	Zn	Pb	Mn	As	Au	Ag	Cd	Σ	Fe/Zn	mol % FeS	T
Min	31.90	<0.02	<0.03	45.99	<0.06	<0.03	<0.02	<0.02	<0.03	<0.03	97.40	0.00	0.00	227
Max	39.10	14.29	1.90	67.89	0.50	4.13	0.20	0.10	0.10	0.70	101.9	0.31	26.67	387
Average	33.33	1.95	0.39	63.78	<0.06	0.17	<0.02	<0.02	<0.03	0.25	100.1	0.03	3.69	251
Median	33.30	1.19	0.24	64.36	<0.06	<0.03	<0.02	<0.02	<0.03	0.22	100.2	0.02	2.15	241
Std Dev	0.53	2.17	0.44	3.02	0.06	0.02	<0.02	0.02	0.02	0.16	1.01	0.04	4.25	27

Galena

	S	Fe	Cu	Zn	Pb	Sb	Ge	Ag	As	Au	Mn	Se	Co	Σ
Min	12.95	0.07	0.09	0.47	85.68	<0.04	<0.02	<0.03	<0.03	<0.04	<0.04	<0.03	<0.03	100.2
Max	13.63	0.34	0.50	2.06	87.25	0.27	0.04	<0.03	<0.03	<0.04	<0.04	0.07	0.04	102.7
Average	13.45	0.15	0.32	1.06	86.31	0.14	<0.02	<0.03	<0.03	<0.04	<0.04	<0.03	<0.03	101.5
Median	13.59	0.11	0.38	0.56	86.39	0.11	<0.02	<0.03	<0.03	<0.04	<0.04	<0.03	<0.03	101.5
Std Dev	0.28	0.11	0.19	0.63	0.65	0.11	0.02	<0.03	<0.03	<0.04	<0.04	0.03	<0.03	1.12

Bornite

	S	Fe	Cu	Zn	Pb	As	Au	Ag	In	Sb	Cd	Se	Mn	Σ
Min	26.09	11.30	61.32	<0.06	<0.05	<0.02	<0.03	<0.03	<0.03	<0.03	<0.03	<0.02	<0.03	100.0
Max	26.64	12.18	64.00	0.91	0.14	0.04	0.04	0.05	0.08	0.04	0.04	0.04	0.04	102.0
Average	26.27	11.46	63.20	0.19	0.09	<0.02	<0.03	<0.03	<0.03	<0.03	<0.03	<0.02	<0.03	101.3
Median	26.27	11.58	62.85	0.24	0.08	<0.02	<0.03	<0.03	<0.03	<0.03	<0.03	<0.02	<0.03	101.2
Std Dev	0.14	0.26	0.88	0.26	0.06	<0.02	<0.03	<0.03	<0.03	<0.03	<0.03	<0.02	<0.03	0.69

Other Cu sulfides

	S	Fe	Cu	Zn	Pb	As	Au	Ag	Sb	Co	Cd	Mn	Σ
Min	24.93	1.25	22.36	<0.07	<0.06	<0.02	<0.02	<0.02	<0.03	<0.02	<0.03	<0.03	91.09
Max	41.09	34.72	72.77	25.07	0.29	12.64	0.07	0.13	1.03	0.05	0.05	0.11	102.0
Average	30.39	13.67	50.95	2.47	0.06	1.13	<0.02	0.03	0.11	<0.02	<0.03	<0.03	99.24
Median	30.71	13.64	53.34	0.42	0.06	0.00	<0.02	0.02	<0.03	<0.02	<0.03	<0.03	99.47
Std Dev	3.40	6.77	11.45	4.77	0.06	2.78	0.02	0.03	0.25	<0.02	<0.03	<0.03	1.67

Shinas

Pyrite

	S	Fe	Cu	Zn	Pb	Co	Mn	As	Au	Ag	Se	In	Sb	Σ
Min	50.90	42.34	<0.03	<0.06	<0.06	<0.02	<0.02	<0.02	<0.02	<0.02	<0.02	<0.03	<0.03	98.17
Max	53.86	47.41	1.69	5.97	0.31	0.65	0.12	1.50	0.07	0.07	0.10	0.08	0.06	101.3
Average	53.04	46.42	0.07	0.10	<0.06	0.06	<0.02	0.03	<0.02	<0.02	<0.02	<0.03	<0.03	99.82
Median	53.12	46.53	<0.03	<0.06	<0.06	0.03	<0.02	<0.02	<0.02	<0.02	<0.02	<0.03	<0.03	99.92
Std Dev	0.43	0.57	<0.03	0.48	0.06	0.10	<0.02	0.12	0.02	0.02	0.02	0.02	0.02	0.68

Table 2. (*Cont.*)

Shinas

Chalcopyrite	S	Fe	Cu	Zn	Pb	Mn	As	Au	Ag	Cd	Se	In	Sb	Σ
Min	34.26	29.63	33.33	<0.06	<0.06	<0.03	<0.02	<0.02	<0.03	<0.03	<0.02	<0.03	<0.03	98.75
Max	35.27	30.91	36.73	0.40	0.24	0.06	0.06	0.05	0.06	0.05	0.11	0.06	0.05	101.5
Average	34.84	30.40	34.68	0.06	<0.06	<0.03	<0.02	<0.02	<0.03	<0.03	0.02	<0.03	<0.03	100.1
Median	34.85	30.44	34.62	<0.06	<0.06	<0.03	<0.02	<0.02	<0.03	<0.03	0.02	<0.03	<0.03	100.1
Std Dev	0.24	0.30	0.64	0.07	<0.06	<0.03	<0.02	<0.02	<0.03	<0.03	0.03	<0.03	<0.03	0.73

Sphalerite 1	S	Fe	Cu	Zn	Pb	Mn	As	Au	Ag	Cd	Σ	Fe/Zn	mol % FeS	T
Min	33.45	0.86	<0.03	51.07	<0.06	<0.03	<0.02	<0.02	<0.03	<0.03	98.21	0.01	1.61	238
Max	34.07	12.95	1.42	63.50	0.05	0.03	0.02	<0.02	0.06	1.75	100.4	0.25	22.90	372
Average	33.70	6.38	0.66	57.60	<0.06	<0.03	<0.02	<0.02	<0.03	0.46	98.93	0.12	11.40	285
Median	33.66	3.88	0.56	59.60	<0.06	<0.03	<0.02	<0.02	<0.03	0.21	98.70	0.06	6.67	276
Std Dev	0.20	4.60	0.66	4.89	<0.06	<0.03	<0.02	<0.02	<0.03	0.58	0.83	0.09	8.16	51

Sphalerite 2	S	Fe	Cu	Zn	Pb	Mn	As	Au	Ag	Cd	Σ	Fe/Zn	mol % FeS	T
Min	33.10	0.01	<0.03	58.50	<0.06	<0.03	<0.02	<0.02	<0.03	<0.03	98.00	0.001	0.12	228
Max	35.20	6.50	1.30	65.40	0.20	<0.03	<0.02	<0.02	0.10	1.10	101.2	0.11	11.55	313
Average	33.61	1.45	0.19	63.31	<0.06	<0.03	<0.02	<0.02	<0.03	0.20	98.91	0.02	2.61	245
Median	33.61	1.19	0.09	63.53	<0.06	<0.03	<0.02	<0.02	<0.03	0.14	98.89	0.02	2.14	242
Std Dev	0.35	1.42	0.27	1.60	<0.06	<0.03	<0.02	<0.02	<0.03	0.23	0.66	0.02	2.54	18

Chalcocite	S	Fe	Cu	Zn	Pb	Cd	Mn	As	Au	Ag	Se	In	Sb	Σ
Min	19.79	0.02	76.02	<0.07	<0.06	<0.03	<0.03	<0.02	<0.02	<0.02	<0.02	<0.03	<0.03	98.60
Max	21.72	2.61	80.63	0.18	0.09	0.04	0.03	0.06	0.05	0.10	0.03	0.06	0.06	102.7
Average	21.23	0.57	79.41	<0.07	<0.06	<0.03	<0.03	0.02	<0.02	0.03	<0.02	<0.03	<0.03	101.4
Median	21.30	0.18	79.83	<0.07	<0.06	<0.03	<0.03	<0.02	<0.02	0.03	<0.02	<0.03	<0.03	101.6
Std Dev	0.48	0.78	1.24	<0.07	<0.06	<0.03	<0.03	0.02	0.02	0.03	<0.02	<0.03	<0.03	1.09

to the contact with massive sulfides, the Fe (oxy)hydroxide layers are interbedded with sulfide-rich layers (pyrite + chalcopyrite + sphalerite + covellite). Umbers within the hanging-wall sequence contact with the volcanic rocks via intense hematite dissemination in the igneous matrix and are crosscut by late calcite veinlets (Fig. 3E).

Host rocks and hydrothermal alteration

Footwall: The footwall sequence is composed of massive and pillowed basaltic lavas strongly overprinted by hydrothermal alteration. The primary mineralogy and textures are mostly obliterated, except for swallowtailed plagioclase microlites, where albite cores are overgrown by quartz (Fig. 5A). Silicification, pyrite dissemination, albitization, and Al-rich clays (beidellite) are more common in domains closest to the orebody (Fig. 3F). The silicified rocks are affected by a tight network of quartz veins (often with comb texture) with pyrite + chalcopyrite ± sphalerite ± galena. These veins develop into microcrystalline quartz bands sometimes reopened via crack-seal mechanisms and infilled by late calcite or zeolites + pyrite (Fig. 5C, D). The silica + pyrite alteration halos are surrounded by chlorite + quartz + pyrite alteration zones (Fig. 5B). In these chlorite + quartz + pyrite zones, chlorite is more Mg rich (#Mg 0.59–0.74) than chlorite cementing the ore breccias (#Mg 0.46–0.53), which display a trend of decreasing Al/Si with FeO/(FeO + MgO) (App. 4).

Hematite + quartz veinlets and mineralized jaspers are common in the footwall (Fig. 3H). The jaspers have disseminated pyrite + sphalerite ± chalcopyrite (altered to Cu-rich sulfides) within the microcrystalline silica + hematite matrix. Footwall jaspers are crisscrossed by quartz + chalcopyrite + pyrite ± sphalerite veins with bleaching halos (Fig. 5E).

Hanging wall: The hanging-wall sequence comprises pervasively altered (>90% of the primary phases) massive and pillowed lava flows. Rare monomict autoclastic breccias occur at the top of lava flows and/or at the contact between individual pillow lavas.

The basaltic rocks are vesicular microporphyritic, and primary textures are poorly preserved (Fig. 3I, J). Plagioclase ($An_{37.0–84.9}$; An = anorthite) and clinopyroxene ($En_{34–56}Wo_{28–44}Fs_{8–38}$; En = enstatite, Fs = forsterite, Wo = wollastonite) microphenocrysts occur as unzoned single crystals and as glomerophyric clusters in a matrix composed of plagioclase, clinopyroxene microlites, and disseminated magnetite (Fig. 5F-H). The matrix is extensively altered to brownish-greenish clays (corrensite; Apps. 1, 4; Fig. 5F-I; Mosser-Ruck et al., 2016) and is locally intergrown with fine-grained quartz. Pyroxene is replaced by chlorite and clays (Fig. 5G) and plagioclase by patches of albite ($Ab_{82.1–99.6}$). Vesicles are filled with brown-greenish corrensite, calcite, or quartz (Fig. 5I). Veinlets in the hanging wall are filled with zeolites (epistilbite + laumontite), calcite, and minor chlorite. Hematite ± carbonate (Fig. 5J) and hematite + quartz + chlorite veinlets are common in the extrusive section of the ophiolite and thought to postdate obduction (Belgrano et al., 2019).

The footwall sequence is intruded by dolerite dikes, presumably the feeders of the hanging-wall volcanic sequence. These display well-developed intersertal textures, with clino-

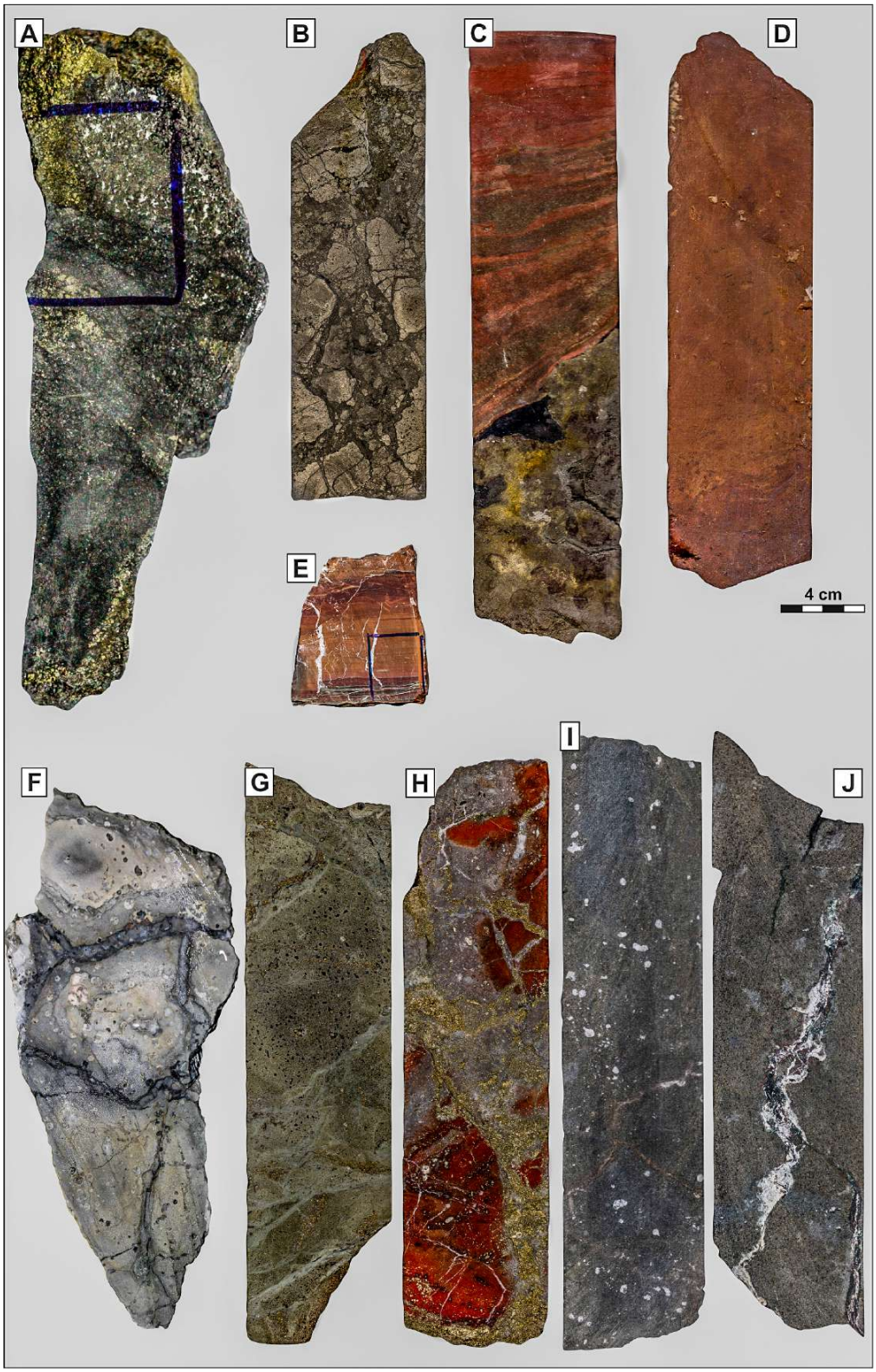

Fig. 3. Representative samples of the Mandoos deposit. (A) Sphalerite- and chalcopyrite-rich massive sulfide breccia, with pyrite + chalcopyrite clasts, set in a fine-grained pyrite + quartz + sphalerite matrix. (B) Sulfide breccia with jigsaw-fit texture: pyrite clasts cemented by quartz + pyrite matrix. (C) Contact between sulfide breccia (with sphalerite-rich clasts) and sulfide-rich umber. (D) Fe (oxy)hydroxide ochre. (E) Umber with carbonate veinlets. (F) Silicified footwall with disseminated pyrite and quartz + zeolite veins. (G) Chloritized footwall with pyrite dissemination, and quartz + pyrite veins. (H) Mineralized jasper with quartz + sulfide veins. (I) Microporphyrytic basalt (hanging wall) with carbonate amygdules and veins. (J) Microporphyritic basalt (hanging wall) with carbonate + hematite + chlorite vein.

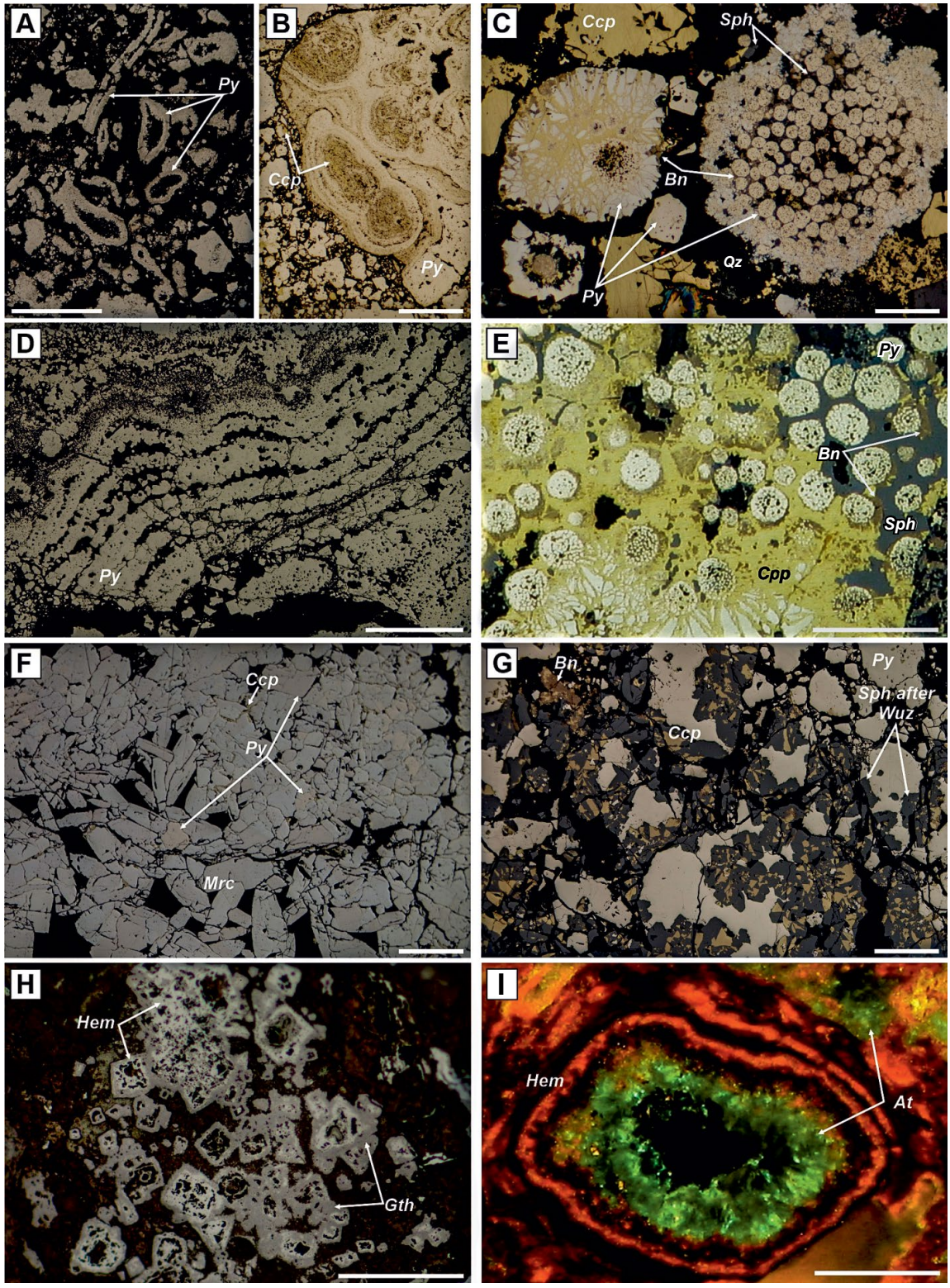

Fig. 4. Mineralogical and textural features of Mandoos ores and ochres. (A) Pyrite (Py)-rich breccia cemented by quartz (Qz) with pyritized worm tube burrow sections. (B) Clast with colloform texture in pyrite + chalcopyrite (Ccp) breccia. (C) Pyrite + chalcopyrite breccia cemented by quartz: brecciated pyrite clasts cemented by chalcopyrite (left) and framboidal pyrite aggregates (right), with sphalerite (Sph) and chalcopyrite replaced by bornite (Bn). (D) Banded colloform pyrite aggregates. (E) Framboidal and brecciated idiomorphic pyrite replaced by chalcopyrite (locally replaced by bornite). (F) Marcasite laths (Mrc) and pyrite intergrown with quartz. (G) Sphalerite after wurtzite (Wur); hexagonal sections with chalcopyrite inclusions (locally replaced by bornite). (H) Hematite (Hem) and goethite (Gth) after pyrite in ochre. (I) Atacamite (At) crystals within pyrite pseudomorph. Scale bars = 400 µm.

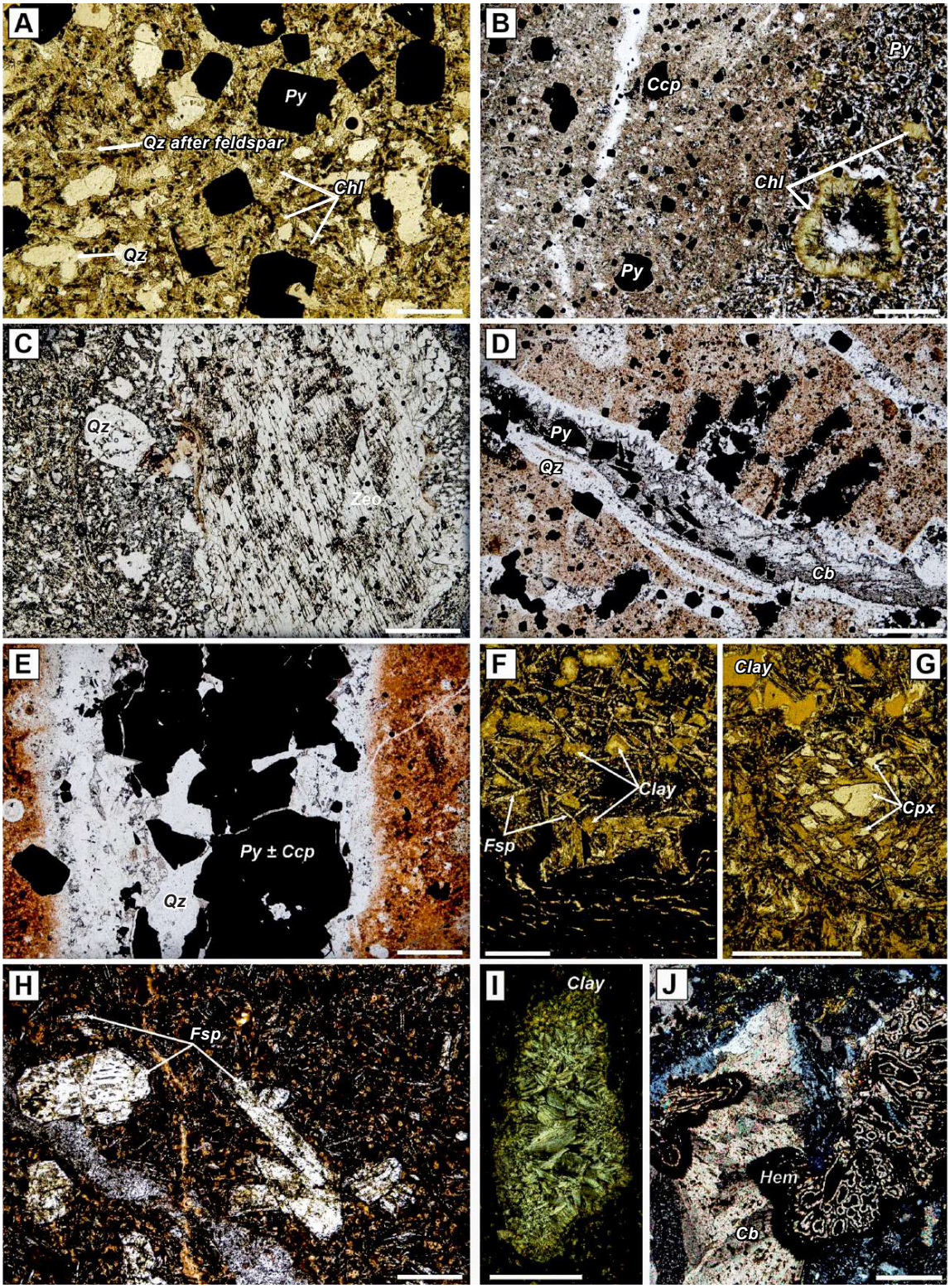

Fig. 5. Mineralogical and textural features of Mandoos footwall (A-E) and hanging-wall (F-J) volcanic rocks. (A) Chlorite + quartz + pyrite alteration with disseminated pyrite (Py) with quartz (Qz) and silicified feldspar. (B) Microcrystalline quartz veinlet, with pyrite + chalcopyrite (Ccp) in moderately silicified footwall. (C) Quartz + zeolites (Zeo) filling a vesicle in silicified footwall. (D) Crack-and-seal vein in jasper: quartz + sulfide followed by carbonate (Cb) + pyrite. (E) Quartz + pyrite + chalcopyrite vein showing a bleached halo at the contact with the jasper. (F) Microporphyritic basalt with feldspar (Fsp) microlites in clay-altered matrix. (G, H) Clay alteration in the matrix; clinopyroxene and feldspar microphenocrysts. (I) Clay-infilled vesicle. (J) Carbonate + hematite veins. Scale bars = 400 µm. Abbreviations: Chl = chlorite, Cpx = clinopyroxene, Hem = hematite.

pyroxene and plagioclase microphenocrysts in a brownish clay-rich altered matrix, including magnetite and accessory acicular apatite.

Geology of the Shinas Deposit

Orebody morphology and base metal distribution

The Shinas deposit comprises a northwest-southeast lenticular, elongated massive sulfide orebody (~160 m), gently dipping to the southeast. Two central pipe-like feeder zones extending down to 120 m underlie the orebody, which ranges in thickness from 25 to 40 m beneath the southeast feeder (Fig. 6; Apps. 3, 5). Calculated mineralogy using mine assay data for sulfide ores indicates an average composition of 40 vol % pyrite, 52 vol % quartz, 7.5 vol % chalcopyrite, and 0.4 vol % sphalerite, consistent with petrographic observations. Considering our calculated orebody volume of 0.82 Mt and the relative proportion of silica-rich/massive sulfide ores using a 0.3 wt % Cu cutoff grade, an average Cu = 2.6 wt %, and Zn = 0.3 wt % are calculated.

The spatial distribution of Cu and Zn grades shows that the feeder zones and the overlying orebody are Cu rich (>2 wt %). A smaller sulfide accumulation to the southwest (not integrated in the model) also has significant Cu grades (>1.19 wt %). Higher Cu concentrations (>3.6 wt %) likely represent areas of secondary enrichment. Zinc grades roughly overlap the Cu-rich domains near the feeder zones but are higher (>0.36 wt %) in the periphery of the orebody (Apps. 3, 5).

Massive sulfide mineralization and ochres

Shinas massive ores comprise breccias with heterometric sulfide clasts embedded in a quartz-rich matrix with disseminated sulfide (Fig. 7A; silica-sulfide). Sulfide clasts are elliptical or form coarsely banded structures (Fig. 7A, B) and microscopically correspond to subhedral pyrite aggregates engulfed by anhedral chalcopyrite (Fig. 8A). Less common textures include bladed, radial pyrite arrays (Fig. 8B) and massive pyrite cut by radial vein networks of chalcopyrite (Fig. 8C, here replaced by chalcocite). Sphalerite occurs as minute inclusions in pyrite or larger grains associated with chalcopyrite (Fig. 8A). The granular quartz matrix (≤0.5 mm) locally forms colloform bands on sulfides (Fig. 7A, B).

Two jasper generations are observed throughout the deposit: (1) jasper I, dark red/maroon, mostly forming the matrix of the footwall breccia (see below; Fig. 7C), and (2) jasper II, bright red, commonly veining the massive ores (Fig. 7B). Most of the deposit is capped by ~1-m-thick ochre (hematite + quartz). An oxidation paleosurface is marked by a vuggy skeletal silica-rich gossan preserving earthy-orange aggregates from sulfide oxidation. The effects of oxidation fade out downhole for ~20 m to oxidized ores where chalcopyrite was replaced by chalcocite (Fig. 8C).

Host rocks and hydrothermal alteration

Footwall: The footwall comprises hydrothermal breccias (Fig. 6), classified as matrix supported and clast supported. The matrix-supported breccia grades down from the massive sulfides through ~30 m and comprises fragmented, fully altered, and often rounded basalt clasts (Fig. 7D, E) plus rare clasts from the underlying clast-supported breccia (Fig. 7F). The matrix-supported breccia comprises trails of yellow Al-rich phyllosilicates (beidellite; Fig. 8D, E). The basalt clasts include silicified plagioclase laths within a dark quartz-rich chlorite matrix (Fig. 8F; #Mg 0.63–0.65) with sparsely disseminated pyrite and micron-sized TiO_2 oxides.

The contact between both breccia units is gradational over a few meters with progressively larger clast-supported breccia lithoclasts included in the matrix-supported breccia assemblage (Fig. 7G). The clast-supported breccia has greenish basalt clasts (≤50 mm) with jigsaw-fit texture cemented by discolored jasper I (Fig. 8G) and cut by sulfide + quartz veins. Across the clast-supported breccia unit, chlorite #Mg decreases downhole (0.52–0.62). Sulfide abundance decreases sharply downhole, from 30 vol % at the matrix-supported breccia-massive sulfide contact down to ~3 vol % in the clast-supported breccia unit. Mineralization is associated with the vein network crosscutting the clast-supported breccia unit (quartz + pyrite + chalcopyrite ± sphalerite; Fig. 7H) that coalesces to form the quartz-rich matrix of the matrix-supported breccia unit; basalt lithoclasts bear only pyrite. Late veining in the matrix-supported breccia unit comprises (1) early jasper I veins rimmed by brecciated pyrite (Fig. 7D) and (2) wispy, microgranular quartz veinlets.

Hanging wall: The hanging wall comprises vesicular basaltic facies with intergranular texture where up to 70 vol % of the original assemblage was replaced by secondary minerals. Plagioclase ($An_{23.0–89.6}$) forms a 0.2-mm lath network that is 70 to 80% altered to albite + quartz. Pyroxene ($En_{36–50}Wo_{35–44}Fs_{10–26}$) develops anhedral to prismatic grains extensively altered (>80%) to green-brown fibrous phyllosilicate aggregates (corrensite; Apps. 1, 4; Fig. 8I). Oxidized magnetite, quartz, and sulfides occur in decreasing relative amounts. The dolerite dikes have similar textural and mineralogical features relative to the basaltic rocks, with coarser-grained minerals and lower alteration (~40%). Scarce veinlets of Mn-bearing siderite + Fe oxides + quartz + clays crosscut the hanging-wall sequence.

Composition of Sulfides

The chemical composition of sulfide phases is summarized in Table 2.

Pyrite and marcasite

Pyrite shows mild enrichment in a few minor elements (<2 wt %) that are distinct for each deposit (Table 2). In Mandoos, pyrite is consistently enriched in Cu, Zn, and Mn relative to Shinas. Framboidal aggregates (Fig. 4C) display higher Cu concentrations relative to colloform or massive/euhedral pyrite (Fig. 4A, C, D, G), which has higher Zn/Cu ratios. Pyrite from Shinas (Fig. 8A, B) displays a systematic Co enrichment and similar As concentrations relative to Mandoos. Average concentrations for other elements lie close or below the detection limit of the EPMA (Table 2). Marcasite (Fig. 4F) occurs only in Mandoos and presents similar compositional features as pyrite, except for lower Cu and As and higher Mn concentrations.

Cu sulfides

Chalcopyrite from Mandoos (Fig. 4B, C) shows a negative correlation between Cu and Zn concentrations, suggesting

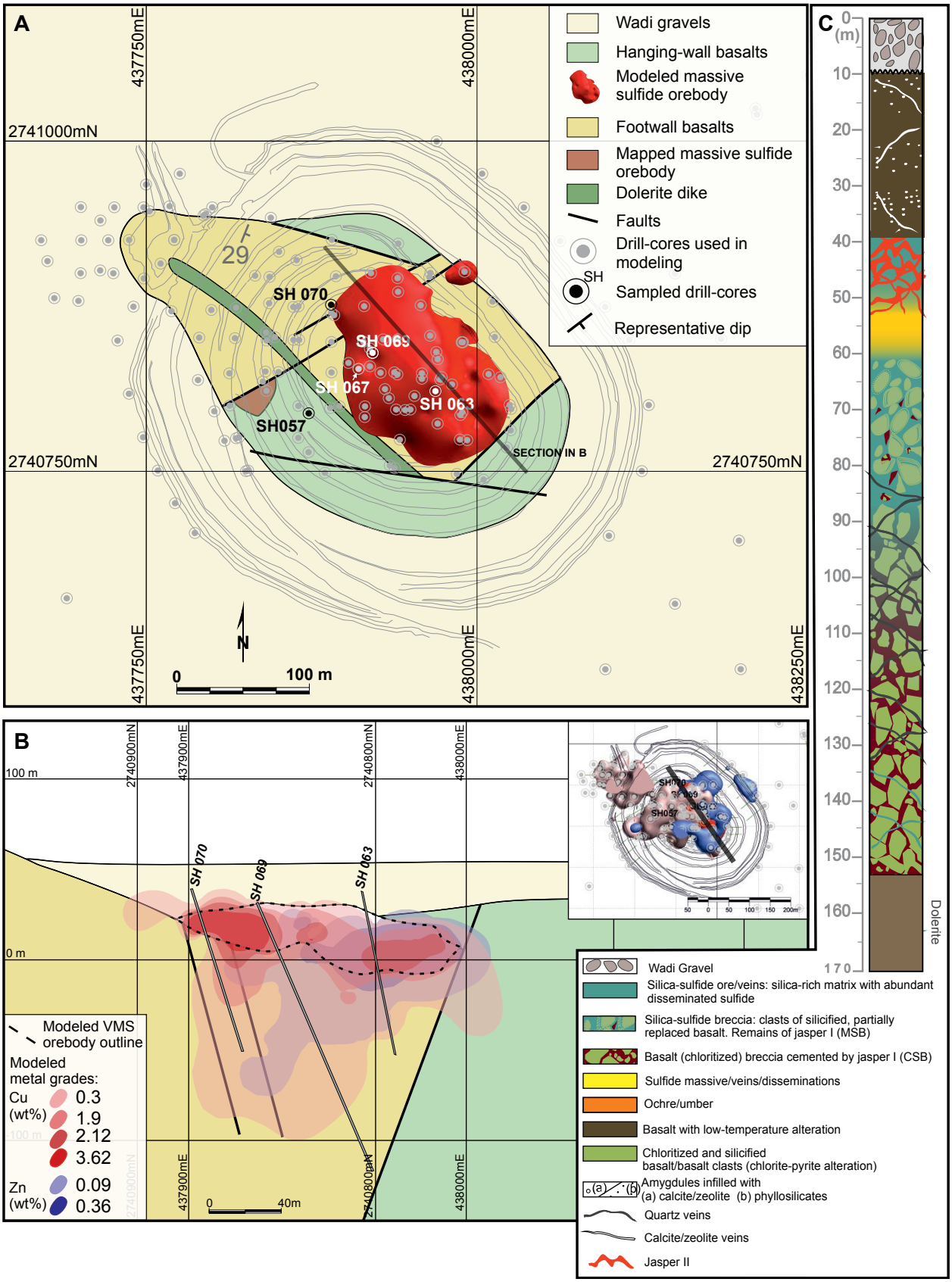

Fig. 6. Geology of the Shinas deposit. (A) Location of the drill cores used for modeling and sampling. (B) Cross section with projected Cu and Zn mine assay modeled grades. (C) Lithostratigraphic column based on this work's logging. VMS = volcanogenic massive sulfide.

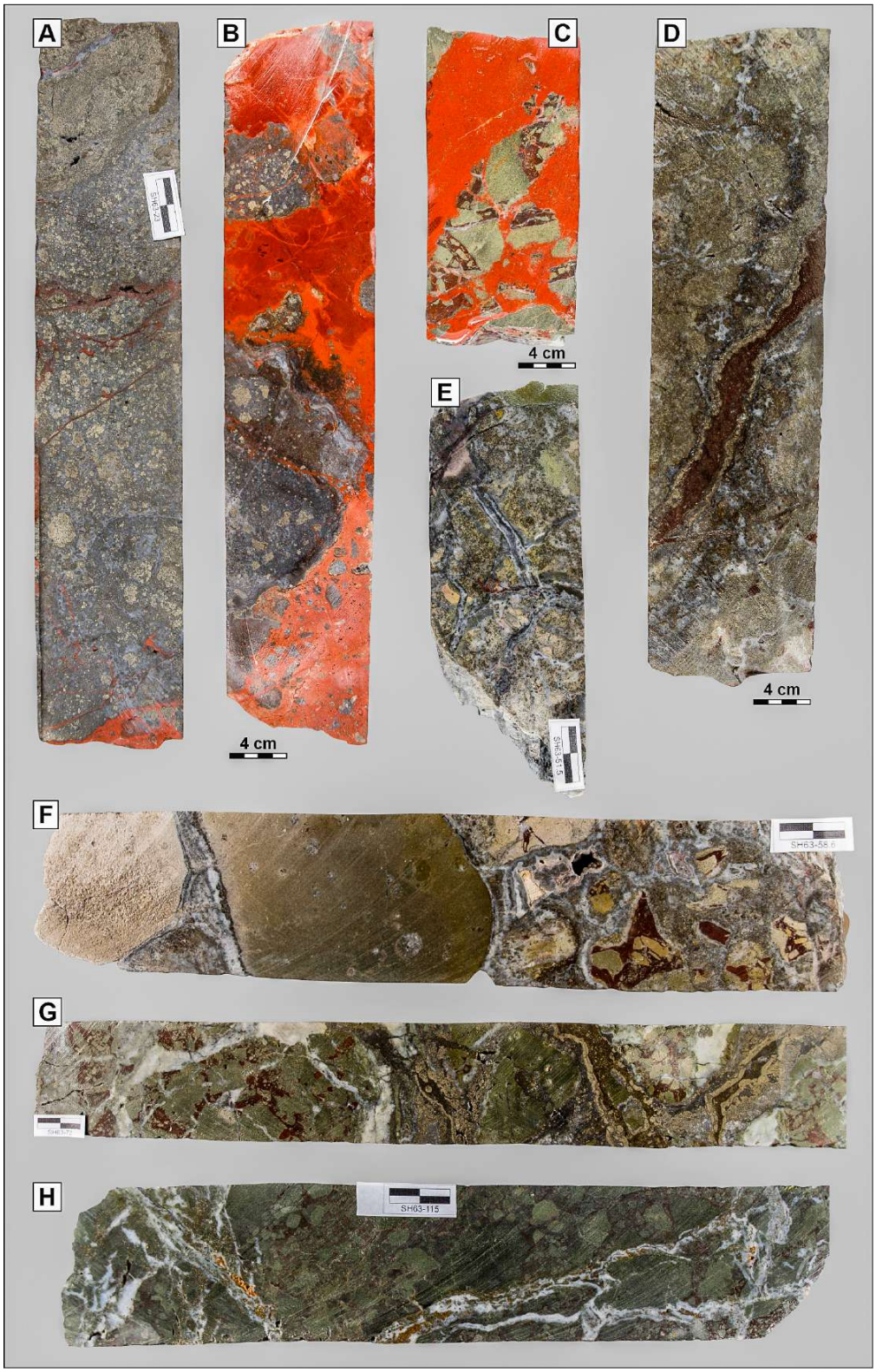

Fig. 7. Macroscopic features in Shinas ores and footwall. (A, B) Silica-massive sulfide with sulfide fragments embedded in a quartz matrix, crosscut by jasper II. (C) Crosscutting relationships between jasper I (matrix of the clast supported breccia) and jasper II. (D, E) Matrix-supported breccia: disaggregated basalt clasts within pyrite + chalcopyrite + quartz matrix; jasper I vein rimmed by sulfides + quartz. (F) Matrix-supported breccia: rounded basalt and clast-supported breccia lithoclasts. (G) Transition between breccia units: large clast-supported breccia lithoclasts veined by quartz + phyllosilicate + sulfide that make up the matrix-supported breccia matrix. (H) Clast-supported breccia: angular basalt lithoclasts brecciated by jasper I.

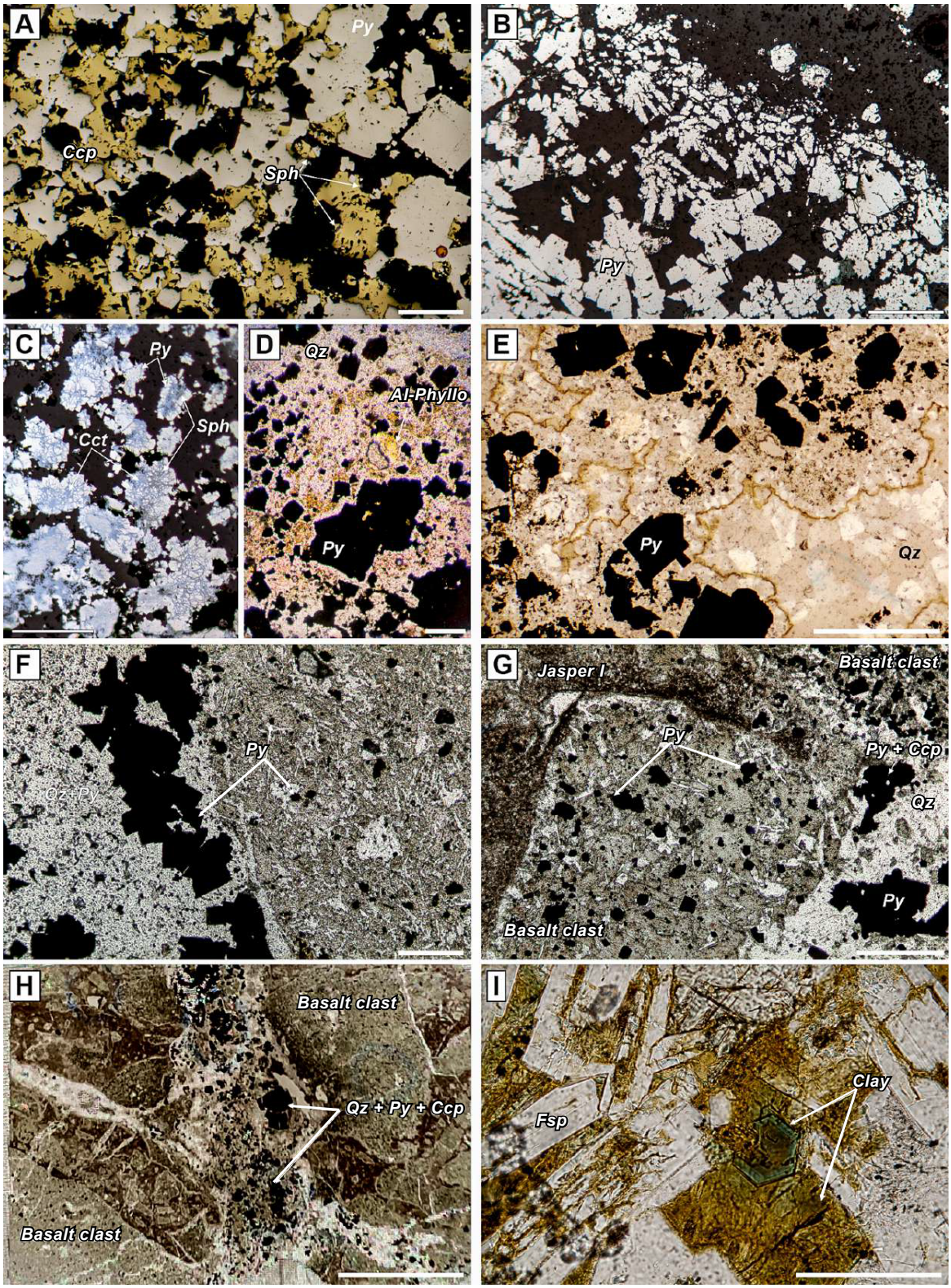

Fig. 8. Mineralogical and textural features of Shinas deposit. (A) Massive ore: pyrite (Py) replaced by chalcopyrite (Ccp) with small sphalerite (Sph) grains. (B) Bladed pyrite in massive ore. (C) Brecciated pyrite cemented by chalcocite (Cct) after chalcopyrite. (D, E) Matrix-supported breccia quartz matrix with interspersed yellow phyllosilicates and quartz (Qz) colomorphic bands around pyrite. (F) Matrix-supported breccia basalt lithoclasts (right) showing silicified plagioclase laths in quartz + phyllosilicate matrix with disseminated pyrite, cut by quartz + pyrite vein (left). (G, H) Clast-supported breccia: basalt lithoclast (silicified plagioclase in chlorite + pyrite matrix) in jasper I matrix cut by mineralized quartz + pyrite + chalcopyrite vein. (I) Dolerite matrix altered to corrensite. Scale bars = 400 μm. Fsp = feldspar.

lattice replacement. Zinc concentrations are comparatively lower in samples from Shinas (Table 2).

Bornite (Fig. 4C, E, G) in Mandoos samples is close to the ideal stoichiometry, with low Zn and Pb concentrations, similar to the precursor chalcopyrite. Other Cu sulfides from Mandoos (optically indistinguishable) yield nonstoichiometric compositions along two main trends: (1) from fukuchilite- and cubanite-like compositions toward chalcopyrite and (2) replacing chalcopyrite toward bornite, covellite, and spionkopite (App. 4).

Sphalerite

Sphalerite from Mandoos ores (Fig. 4E, G) has a relatively homogeneous composition, with low Fe concentrations, leading to average Fe/Zn ratios and FeS mol % of 0.04 and 3.8, respectively (App. 4). Sphalerite in veins, replacing wurtzite, or intergrown with chalcopyrite shows more limited variation in Fe (≤1.4 wt %). The Cu concentrations of sphalerite without chalcopyrite disease are below 2 wt %. A few sphalerite masses have significant Mn (<4.1 wt %) and Fe (1.4–8.7 wt %). Minor elements in Mandoos include Cd and Pb. The composition of sphalerite in the footwall rocks closely resembles that of the ores with average (X) Fe/Zn and FeS mol % X = 0.02 and 2.8, respectively, and minor concentrations of Cu, Cd, and Mn (Table 2).

In Shinas (Fig. 8C), two groups of sphalerite can be distinguished: (1) sphalerite inclusions in pyrite show higher Fe and Cu leading to high FeS mol % (X = 11.4), and (2) sphalerite coprecipitating with pyrite and chalcopyrite has significantly lower Fe (FeS mol % X = 0.03). All analyses show minor Cd concentrations (Table 2).

Galena

Galena in the Mandoos footwall and Zn-rich ores has minor concentrations of Zn, Cu, Fe, and Sb (Table 2).

Whole-Rock Geochemistry

Host volcanic rocks

Major and trace element analyses of the hanging-wall and footwall volcanic rocks are reported in Table 3. Major element concentrations referred to in the text and plotted in Figure 9 were normalized to an anhydrous (AN) basis. Based on textural and mineralogical criteria previously presented we can distinguish between footwall rocks that show chlorite-dominated alteration and those where silicification prevails; for the Shinas deposit, this equates to the clast-supported breccia and matrix-supported breccia, respectively.

The footwall rocks from Mandoos are the only rocks with TiO_2 > 1 wt %$_{-AN}$. All analyzed rocks show fractionation trends from basalt to andesite with tholeiitic affinity (App. 6; Pearce, 1996; Ross and Bédard, 2009).

Hanging-wall lavas and dolerites: Average loss on ignition (LOI) values are 4.36 wt % for Mandoos and 3.16 wt % for Shinas and as high as 13.9 wt %, indicating that all rocks underwent extensive alteration. In Mandoos, SiO_2 is positively correlated with Na_2O, TiO_2, P_2O_5, and Zr and negatively correlated with MgO, Al_2O_3, CaO, and Fe_2O_3, forming trends reminiscent of magmatic differentiation processes combined with alteration effects. Such trends are less evident in Shinas rocks because of more limited sampling of hanging-wall lavas (Fig. 9). Mandoos lavas have a wider range of #Mg (molar Mg/Mg + Fe: 43–67) relative to Shinas (48–64). Chromium and Ni concentrations follow similar trends with a large and generally more evolved span for Mandoos (X = 25 ± 43, 15 ± 15 µg/g) relative to Shinas (X = 58 ± 24, 34 ± 5 µg/g; ± referring to 1σ standard deviation). For both deposits, Na_2O concentrations at given MgO lie at the lower range of mid-ocean ridge basalt (MORB; White and Klein, 2014); CaO shows marked depletion (X_{MORB} = 11.46 ± 0.91 wt %) and K_2O is enriched well above MORB (X_{MORB} = 0.19 ± 0.18 wt %) reflecting the combined effects of pyroxene breakdown, clay formation, and plagioclase albitization.

Chondrite (CN)-normalized REE patterns for Mandoos samples (Fig. 10A) are characterized by enrichments between $(2–22)_{CN}$ and a broad range of light (L)REE depletion ($(La/Sm)_{CN}$ = 0.42–0.62) throughout the thick hanging-wall sequence. Small negative Eu anomalies ($Eu/Eu^* = Eu_{CN}/(Sm_{CN} \times Gd_{CN})^{0.5}$, $X_{Mandoos\ (MD)}$ = 0.89) suggest plagioclase fractionation. The REE patterns for Shinas hanging-wall display lower bulk REE abundances $(5–14)_{CN}$ but milder LREE depletion $(La/Sm)_{CN}$ = 0.78–0.81 (Fig. 10B). Dolerites have lower REE abundances and show less pronounced Ti negative anomalies in primitive mantle (PM)-normalized plots, indicating they represent less fractionated equivalents, as expected for the putative feeders of their hanging-wall lavas.

All lavas display small Ce negative anomalies ($Ce/Ce^* = 3 \times Ce_{CN}/(2 \times La_{CN} + Nd_{CN}$; X_{MD} = 0.92; $X_{Shinas\ (SH)}$ = 0.97) and significant enrichments in Cs, Rb, Sr, Pb, and U typical of seawater interaction (Staudigel, 2014). Differences in high field strength element (HFSE) ratios between elements with similar degrees of incompatibility suggest distinct magmatic affiliations for the hanging-wall lavas in each deposit: Zr/Hf X_{MD} = 29.1 ± 1.7; X_{SH} = 35.4 ± 1.1; Nb/Ta X_{MD} = 14.1 ± 0.6; X_{SH} = 11.6 ± 0.4.

Footwall lavas: For both deposits, the highly silicified rocks (matrix-supported breccia in Shinas) show features that depart from magmatic trends of their hanging-wall suite, whereas chlorite-dominated rocks in Mandoos preserve igneous features to various extents. As alteration intensifies, there is progressive loss of alkalis (Na, K, Cs, Rb) and Ca (Figs. 9A, E, 10E, F) and a bulk decrease in incompatible element abundances, leading to highly irregular patterns (Fig. 10C-F). Uranium and Pb positive anomalies are similar in both types of alteration, whereas the most pronounced negative Ce anomalies are recorded in intensely silicified rocks.

In Mandoos, silica concentrations in the chlorite-rich footwall overlap the lower range of the silicified domains where carbonate veining accounts for the lowest silica concentrations. Chlorite-rich rocks have lower base metal concentrations (Cu + Zn + Pb X = 1,506 µg/g) compared to those in silicified domains (X = 2,558 µg/g), which correlate with an increase in the proportion of chalcopyrite + sphalerite. Chlorite-dominated footwall rocks from Mandoos preserve magmatic incompatible element patterns with higher bulk abundances than its hanging-wall lavas. Footwall chlorite-rich rocks have overlapping to slightly higher Nb/Ta (14.3 ± 0.3) and Zr/Hf (X = 32.7 ± 1.5) ratios and less pronounced LREE/heavy (H)REE fractionation (La/Sm_{CN} X = 0.65 ± 0.13; Fig. 10).

Table 3. Whole-Rock Geochemistry for Hanging-Wall and Footwall Lavas of Mandoos (MD) and Shinas (SH)

	MD429-81.4	MD429-74.7	MD429-81.70	MD431-42.1	MD431-57.8	MD431-69.0	MD431-91.0 (1)	MD431-91.0 (2)	MD431-91.0 (3)	MD431-95.8
(wt %)	Hanging-wall volcanic (distal)									
SiO_2	53.80	43.24	62.50	50.24	46.23	53.80	65.63	64.42	58.51	60.11
Al_2O_3	14.10	12.84	11.91	15.04	13.56	14.10	12.57	12.65	12.87	13.23
Fe_2O_3	9.82	10.12	7.31	10.86	9.69	9.82	8.00	8.45	9.59	8.59
MnO	0.19	0.40	0.22	0.17	0.33	0.19	0.25	0.24	0.24	0.33
MgO	5.49	6.19	4.87	7.78	7.31	5.49	3.03	3.27	5.10	3.77
CaO	8.64	15.40	6.14	8.38	11.30	8.64	3.92	4.24	4.61	5.13
Na_2O	2.39	1.76	2.90	2.25	1.48	2.39	3.39	3.21	3.40	3.54
K_2O	0.68	1.05	0.77	0.26	0.20	0.68	0.86	0.79	0.92	1.36
TiO_2	0.44	0.38	0.72	0.40	0.37	0.44	0.78	0.77	0.77	0.81
P_2O_5	0.04	0.03	0.14	0.04	0.02	0.04	0.09	0.08	0.09	0.08
SO_3	0.88	0.03	0.08	0.59	0.05	0.88	0.23	0.14	0.23	0.07
LOI	3.46	8.50	2.38	3.88	9.37	3.46	1.20	1.70	3.60	2.89
Total	99.91	99.94	99.92	99.90	99.91	99.91	99.94	99.96	99.93	99.92
(µg/g)										
Cu	39	13	19	54	67	29	13	19	31	23
Zn	67	48	70	59	54	54	63	65	80	77
Pb	0.8	0.5	0.8	0.6	0.6	3.3	2.9	3.0	0.6	1.4
Li	20	11	23	7	16	15	16	17	13	14
Sc	27	33	25	36	43	31	26	26	40	29
V	145	223	132	234	266	124	105	101	273	140
Cr	4	18	2	21	21	10	7	4	15	4
Co	17	28	13	31	34	24	17	16	24	18
Ni	3.6	13.1	1.9	17.5	17.9	11.7	5.5	6.1	10.5	2.4
Ga	11.9	11.1	11.9	11.7	15.7	14.1	12.4	12.3	12.7	12.2
Ge	1.2	1.6	1.3	1.2	1.7	1.6	1.6	1.5	1.4	1.5
As	0.8	4.8	1.4	0.4	0.8	10.2	5.6	6.9	3.4	5.8
Se	0.16	0.12	0.22	0.07	0.14	0.18	0.06	0.13	0.08	0.13
Rb	12.0	15.0	7.4	2.8	3.1	11.0	8.7	7.9	9.3	15.8
Sr	78	87	78	162	105	89	92	85	97	100
Y	19.0	23.2	33.1	12.9	20.4	28.0	24.3	23.9	14.8	25.2
Zr	35.8	14.5	45.1	14.8	18.7	54.5	51.5	49.5	16.8	52.5
Nb	0.58	0.18	0.78	0.18	0.24	0.94	0.85	0.84	0.21	0.88
Mo	0.3	0.2	0.4	0.1	0.1	0.5	0.5	0.5	0.2	0.6
Ag	0.02	0.01	0.03	0.01	0.02	0.03	0.03	0.03	0.01	0.03
Cd	0.0	0.2	0.1	0.1	0.1	0.0	0.1	0.1	0.0	0.0
In	0.1	0.0	0.1	0.1	0.1	0.1	0.1	0.1	0.1	0.1
Sn	0.4	0.1	0.5	0.3	0.3	0.5	0.5	0.4	0.2	0.6
Sb	0.1	0.1	0.1	0.0	0.1	0.1	0.1	0.1	0.1	0.1
Te	0.02	bdl	0.05	0.01	bdl	0.38	0.03	bdl	0.02	0.12
Cs	0.13	0.29	0.06	0.05	0.05	0.26	0.16	0.14	0.13	0.24
Ba	41.2	25.1	44.4	12.4	11.4	49.2	66.3	57.5	27.1	65.5
La	1.32	0.69	2.24	0.61	1.01	2.13	1.82	1.88	0.71	1.82
Ce	3.40	1.80	5.70	1.70	2.80	5.80	5.20	5.20	1.90	5.10
Pr	0.68	0.35	1.13	0.34	0.51	1.00	0.89	0.89	0.36	0.90
Nd	3.97	2.30	6.58	2.10	3.19	5.68	5.14	5.08	2.22	5.11
Sm	1.52	1.02	2.53	0.91	1.34	2.22	1.99	1.94	0.93	2.02
Eu	0.59	0.38	0.87	0.39	0.55	0.77	0.73	0.73	0.39	0.74
Gd	2.50	2.03	4.16	1.66	2.39	3.57	3.14	3.10	1.67	3.21
Tb	0.43	0.40	0.72	0.29	0.44	0.64	0.57	0.54	0.30	0.58
Dy	2.98	2.96	5.02	2.01	3.01	4.35	3.87	3.72	2.11	3.93
Ho	0.65	0.73	1.13	0.44	0.68	0.96	0.85	0.85	0.50	0.90
Er	1.94	2.28	3.30	1.31	1.97	2.78	2.45	2.46	1.54	2.70
Yb	1.88	2.27	3.00	1.26	1.90	2.64	2.44	2.41	1.61	2.70
Lu	0.28	0.35	0.44	0.19	0.28	0.37	0.38	0.35	0.24	0.41
Hf	1.21	0.55	1.48	0.57	0.71	1.78	1.71	1.62	0.62	1.72
Ta	0.042	0.013	0.055	0.012	0.019	0.063	0.061	0.058	0.014	0.063
W	0.07	0.12	0.14	0.04	0.09	0.22	0.19	0.20	0.09	0.14
Tl	0.03	0.03	0.03	bdl	0.01	0.04	0.04	0.04	0.02	0.06
Bi	0.01	0.02	0.02	0.01	0.02	0.02	0.02	0.02	0.02	0.02
Th	0.114	0.047	0.138	0.049	0.065	0.167	0.152	0.147	0.060	0.156
U	0.120	0.052	0.180	0.030	0.041	0.237	0.207	0.208	0.047	0.242
#Mg	53	55	57	59	60	53	43	43	51	47

Table 3. (*Cont.*)

	MD150-40.3	MD150-88.7	MD150-105.8	MD174-39.4	MD174-73.15	MD174-84.7	MD174-92.2	MD178-90.6	MD178-92.0 (1)	MD178-92.0 (2)	MD174-96.0
(wt %)	Hanging-wall volcanic (proximal)										Dolerite
SiO_2	44.75	48.90	60.54	48.98	51.01	51.94	51.25	56.62	47.41	52.97	56.46
Al_2O_3	15.53	13.75	13.97	15.21	14.24	13.40	12.82	13.41	12.57	14.16	13.75
Fe_2O_3	9.70	10.65	8.68	11.78	13.49	12.50	9.68	10.79	10.92	11.02	11.88
MnO	0.08	0.17	0.17	0.22	0.15	0.27	0.09	0.24	0.16	0.22	0.16
MgO	9.91	11.00	4.39	9.84	8.05	8.23	3.85	6.16	8.59	6.41	5.00
CaO	6.67	8.59	2.68	6.76	7.00	5.74	1.99	5.36	11.10	6.41	5.27
Na_2O	1.03	1.68	3.37	1.89	1.55	2.56	5.04	2.80	1.74	2.54	2.63
K_2O	0.49	1.01	1.19	0.44	0.29	0.26	0.11	1.13	1.08	1.63	0.24
TiO_2	0.40	0.61	0.78	0.62	0.52	0.90	0.70	0.60	0.49	0.74	0.88
P_2O_5	0.03	0.04	0.09	0.08	0.03	0.10	0.08	0.05	0.06	0.08	0.08
SO_3	5.15	0.32	0.81	0.19	0.44	0.62	0.39	0.13	0.07	0.56	0.74
LOI	6.19	3.18	3.18	3.87	3.14	3.37	13.92	2.60	5.70	3.17	2.81
Total	99.91	99.90	99.85	99.89	99.89	99.87	99.89	99.89	99.89	99.90	99.91
(µg/g)											
Cu	46	74	36	38	75	68	380	26	14	28	91
Zn	56	71	89	78	57	230	89	58	49	70	62
Pb	0.6	0.5	2.0	0.7	0.7	0.6	1.2	1.5	0.8	1.1	0.7
Li	16	8	11	16	10	13	8	20	13	15	7
Sc	37	38	29	38	40	35	31	34	32	37	30
V	224	258	148	300	307	344	156	339	219	398	154
Cr	21	151	2	55	3	1	1	37	145	6	1
Co	27	36	17	37	32	49	23	28	33	28	20
Ni	16.8	48.6	1.7	43.4	7.0	8.1	0.2	23.2	43.5	16.1	bdl
Ga	13.2	14.1	21.9	15.9	14.3	15.5	13.8	11.7	12.4	14.5	15.3
Ge	1.8	1.3	1.4	2.0	1.4	1.4	1.5	1.3	1.4	1.5	1.5
As	1.1	2.1	9.4	2.7	bdl	5.3	0.7	6.0	4.5	4.9	bdl
Se	0.12	0.13	0.11	0.14	0.12	0.14	0.15	0.09	0.11	0.04	0.14
Rb	7.1	10.1	12.5	4.5	2.8	3.6	0.4	11.0	8.6	18.3	1.9
Sr	109	87	345	187	114	94	73	92	76	78	100
Y	12.7	15.8	22.4	26.2	13.6	27.0	32.4	16.3	17.3	14.9	28.1
Zr	16.7	26.1	55.5	30.3	20.6	44.5	55.6	29.3	21.5	34.2	55.7
Nb	0.22	0.35	0.93	0.38	0.32	0.67	0.96	0.51	0.30	0.61	0.92
Mo	0.2	0.1	0.6	0.2	0.3	0.2	0.4	0.3	0.2	0.4	0.4
Ag	0.04	0.02	0.03	0.02	0.02	0.02	0.03	0.02	0.01	0.02	0.04
Cd	0.1	0.1	0.2	0.1	0.3	0.1	0.1	0.0	0.1	0.2	0.1
In	0.1	0.1	0.1	0.1	0.1	0.1	0.1	0.1	0.1	0.1	0.1
Sn	0.3	0.4	0.5	1.4	0.2	0.6	0.8	0.3	0.2	0.3	0.6
Sb	0.0	0.0	0.2	0.1	0.0	0.2	0.0	0.1	0.1	0.1	0.0
Te	0.01	bdl	0.02	0.15	0.01	0.03	0.01	0.02	0.08	bdl	0.02
Cs	0.10	0.12	0.11	0.04	0.02	0.05	0.02	0.17	0.11	0.21	0.01
Ba	38.5	18.7	216.6	23.7	40.8	21.8	24.5	73.4	25.4	47.0	53.1
La	0.65	0.90	1.70	1.56	0.57	2.21	1.82	1.04	1.05	1.06	1.82
Ce	1.90	2.70	4.90	5.30	1.70	6.40	5.70	2.90	2.80	3.10	5.50
Pr	0.37	0.51	0.87	0.88	0.31	1.13	1.01	0.53	0.49	0.55	0.96
Nd	2.25	2.99	4.99	5.28	1.85	6.36	5.95	2.99	2.82	3.13	5.39
Sm	0.98	1.20	1.93	2.02	0.87	2.39	2.40	1.18	1.07	1.28	2.19
Eu	0.40	0.49	0.61	0.76	0.37	0.90	0.81	0.45	0.43	0.49	0.77
Gd	1.67	1.98	3.00	3.40	1.57	3.70	3.94	1.96	1.83	1.96	3.50
Tb	0.30	0.36	0.53	0.58	0.29	0.64	0.72	0.36	0.35	0.35	0.63
Dy	2.11	2.48	3.61	3.96	2.11	4.31	5.12	2.51	2.44	2.39	4.20
Ho	0.46	0.56	0.79	0.90	0.48	0.95	1.14	0.58	0.57	0.52	0.97
Er	1.38	1.70	2.37	2.53	1.45	2.76	3.49	1.75	1.74	1.53	2.86
Yb	1.39	1.64	2.26	2.35	1.46	2.58	3.47	1.72	1.84	1.58	2.71
Lu	0.21	0.25	0.32	0.35	0.22	0.39	0.54	0.27	0.29	0.23	0.41
Hf	0.62	0.90	1.79	1.03	0.75	1.48	1.89	0.98	0.73	1.12	1.74
Ta	0.016	0.025	0.064	0.028	0.024	0.048	0.067	0.034	0.022	0.045	0.066
W	0.08	0.04	0.11	0.08	0.07	0.03	0.08	0.06	0.06	0.09	0.05
Tl	0.02	0.03	0.07	0.02	0.02	0.03	bdl	0.04	0.03	0.08	bdl
Bi	0.01	0.02	0.01	0.02	0.01	0.02	0.02	0.01	0.02	0.02	0.02
Th	0.060	0.070	0.170	0.084	0.075	0.116	0.171	0.091	0.055	0.108	0.170
U	0.061	0.073	0.177	0.051	0.069	0.104	0.185	0.101	0.069	0.102	0.133
#Mg	67	67	50	62	54	57	44	53	61	54	45

Table 3. (*Cont.*)

	MDP2-8-1	MDP2-9-1	MDP2-6-4	MDP2-7-2	MDP2-7-5	MD431-117.0	MDP1-6.7	MDP2-7-3	MD431-121.7	MDP2-6-7	MDP3-2-1
(wt %)	Footwall volcanic with chlorite-pyrite alteration										
SiO_2	61.58	62.89	49.15	51.80	71.00	49.89	45.37	50.69	54.74	52.45	54.37
Al_2O_3	15.53	15.95	16.84	15.35	8.74	14.42	15.83	16.13	14.17	15.81	12.95
Fe_2O_3	6.96	5.01	13.59	13.23	7.16	15.06	20.88	13.06	12.40	12.33	12.04
MnO	0.15	0.20	0.46	0.42	0.18	0.24	0.23	0.45	0.20	0.48	0.01
MgO	4.57	4.43	11.05	8.88	5.55	9.49	8.07	9.37	8.30	8.20	0.59
CaO	1.43	1.31	2.41	2.75	2.26	7.85	3.38	2.72	7.12	2.58	0.50
Na_2O	3.02	3.77	1.24	1.60	0.82	1.72	2.54	2.00	1.73	2.20	1.06
K_2O	1.49	0.73	1.42	2.51	1.05	0.18	0.81	2.52	0.26	2.67	0.53
TiO_2	1.18	1.21	1.18	1.17	0.51	0.90	1.66	1.31	0.79	1.35	0.45
P_2O_5	0.15	0.17	0.16	0.16	0.09	0.09	0.23	0.15	0.06	0.15	0.03
SO_3	3.80	3.81	2.37	1.90	2.52	0.04	0.82	1.42	0.11	1.53	16.59
LOI											
Total	99.87	99.48	99.86	99.77	99.89	99.87	99.82	99.82	99.87	99.74	99.12
(µg/g)											
Cu	90	320	190	110	130	160	80	100	170	230	7,410
Zn	340	3,870	470	310	300	110	550	560	80	760	120
Pb	47.3	22.9	2.1	5.6	9.5	1.1	3.4	9.0	0.8	1.7	5.6
Li	8	14	22	14	13	6	9	14	12	16	7
Sc	31	28	35	30	12	39	35	37	38	34	17
V	336	298	340	333	186	343	354	371	395	335	178
Cr	4	2	2	3	15	3	1	2	4	1	2
Co	37	30	31	28	15	37	25	34	32	29	69
Ni	11.0	5.2	5.7	6.0	2.4	16.0	4.5	6.2	13.7	5.6	5.0
Ga	12.5	9.2	15.9	16.0	6.3	15.4	24.1	17.7	15.4	15.0	7.0
Ge	1.3	1.3	1.6	1.7	1.4	1.7	2.0	1.6	1.6	1.5	1.9
As	77.2	37.4	4.9	10.3	31.7	16.2	13.3	20.8	bdl	11.7	45.4
Se	0.26	0.19	0.12	0.01	0.00	0.12	0.12	0.21	0.16	0.17	4.65
Rb	4.3	2.4	4.1	7.0	2.1	1.1	13.6	7.4	1.9	7.3	1.5
Sr	56	74	27	35	18	104	94	38	91	44	44
Y	28.5	27.5	34.0	27.0	13.9	30.0	36.4	33.8	17.9	25.6	7.0
Zr	59.7	60.7	64.2	62.2	22.2	38.9	84.1	70.2	36.8	69.4	16.8
Nb	1.50	1.49	1.63	1.58	0.58	0.61	2.41	1.77	0.65	1.69	0.37
Mo	2.0	12.7	0.1	0.1	0.3	0.4	0.4	0.1	0.4	0.3	3.9
Ag	0.17	0.18	0.08	0.06	0.06	0.02	0.04	0.08	0.03	0.08	0.28
Cd	1.4	20.0	0.3	0.4	0.8	0.1	0.1	2.3	0.1	1.2	0.2
In	0.1	0.1	0.1	0.1	0.1	0.1	0.4	0.1	0.1	0.1	0.3
Sn	0.9	0.6	0.9	0.8	0.3	0.5	3.3	1.0	0.3	0.8	0.4
Sb	0.8	0.4	0.1	0.1	0.1	0.2	0.3	0.1	0.0	0.1	0.3
Te	bdl	0.04	0.06	bdl	0.06	0.02	0.94	0.01	0.21	bdl	3.40
Cs	0.02	0.04	0.01	0.02	0.02	0.02	0.26	0.01	0.01	0.01	0.02
Ba	87.2	62.6	57.8	120	49.6	29.2	30.9	129	43.6	138	36.7
La	2.35	2.82	2.85	3.15	1.71	2.25	4.06	2.93	1.06	2.73	0.47
Ce	7.30	8.40	8.40	7.70	3.70	5.60	11.50	8.90	3.20	8.30	1.30
Pr	1.32	1.50	1.46	1.27	0.64	1.09	1.93	1.61	0.56	1.41	0.24
Nd	7.28	8.31	8.20	7.00	3.45	6.45	10.68	9.00	3.24	7.81	1.40
Sm	2.70	2.87	2.96	2.46	1.20	2.47	3.62	3.33	1.33	2.68	0.58
Eu	0.96	0.88	1.16	0.90	0.44	0.93	1.33	1.13	0.55	0.97	0.14
Gd	3.97	4.15	4.45	3.65	1.86	4.06	5.25	4.73	2.09	3.82	0.86
Tb	0.71	0.69	0.80	0.63	0.33	0.72	0.89	0.84	0.39	0.66	0.16
Dy	4.83	4.58	5.20	4.30	2.22	5.21	5.94	5.55	2.74	4.29	1.13
Ho	1.04	0.99	1.15	0.97	0.49	1.16	1.32	1.22	0.63	0.91	0.25
Er	2.97	2.74	3.40	2.97	1.45	3.45	3.77	3.56	1.93	2.55	0.74
Yb	2.83	2.47	3.15	2.94	1.48	3.42	3.55	3.44	1.90	2.27	0.78
Lu	0.39	0.37	0.46	0.46	0.21	0.51	0.52	0.51	0.28	0.31	0.11
Hf	1.75	1.84	1.93	1.90	0.66	1.31	2.50	2.11	1.21	2.07	0.59
Ta	0.102	0.104	0.115	0.109	0.041	0.043	0.170	0.118	0.045	0.120	0.025
W	0.23	0.14	0.38	0.32	0.29	0.17	0.24	0.24	0.08	0.26	0.08
Tl	0.56	0.12	0.01	0.02	bdl	0.02	0.02	0.02	0.01	0.17	0.06
Bi	0.02	0.02	0.02	0.02	0.02	0.02	0.01	0.02	0.02	0.02	0.02
Th	0.170	0.168	0.177	0.180	0.085	0.109	0.240	0.197	0.116	0.193	0.038
U	2.182	3.938	0.230	0.385	0.157	0.199	0.198	0.320	0.091	0.365	0.374
#Mg	57	64	62	58	61	56	44	60	58	58	10

Table 3. (*Cont.*)

	MD150-126.7	MD430-127.7	MD150-141.3	MDP2-4-1	MD430-126.0	MD430-129.0	MDP2-4-3	MD430-131.0	MDP3-1-1	SH57-32.5	SH57-39	SH57-50
(wt %)	Footwall volcanic with quartz-sulfide alteration									Hanging-wall volcanic		
SiO_2		66.40	47.14	53.19	48.69	61.41		52.54	55.20	48.46	50.65	49.64
Al_2O_3		10.97	19.09	1.90	15.32	2.97		18.92	18.56	16.69	15.49	14.86
Fe_2O_3		8.54	14.21	16.11	14.40	12.28		10.03	10.13	11.06	12.66	14.38
MnO		0.03	0.28	0.02	0.11	0.02		0.05	0.14	0.14	0.21	0.60
MgO		5.56	15.20	0.61	9.30	0.42		6.79	10.00	10.13	6.76	6.63
CaO		0.53	0.64	0.48	8.04	1.10		1.01	0.91	4.88	5.74	4.56
Na_2O		0.47	0.24	0.09	1.57	0.32		0.96	0.56	2.63	2.82	3.35
K_2O		0.41	0.07	0.02	0.29	0.11		0.67	0.22	0.63	1.35	1.35
TiO_2		0.69	1.10	0.03	0.54	0.11		1.03	1.17	0.71	0.64	0.63
P_2O_5		0.07	0.10	0.10	0.03	0.02		0.10	0.14	0.06	0.07	0.05
SO_3		6.25	1.62	26.20	1.59	20.64		7.77	2.81	0.05	0.02	0.02
LOI										4.39	3.46	3.80
Total		99.92	99.66	98.76	99.89	99.40		99.87	99.84	99.84	99.87	99.86
(µg/g)												
Cu		180	770	11,670	120	5,570	0	490	600	210	170	42
Zn		50	190	170	110	40	0	60	350	58	53	230
Pb	1.1	1.5	0.4	50.0	1.3	4.8	29.8	1.8	2.0	2.1	1.0	1.5
Li	7	15	7	19	6	7	18	3	10	19	11	7
Sc	27	17	37	1	45	2	1	25	30	44	41	41
V	272	174	331	76	347	32	111	241	300	346	287	294
Cr	5	1	5	11	6	9	13	2	3	33	24	35
Co	38	85	38	71	39	178	51	112	26	37	34	64
Ni	4.8	2.9	10.9	8.7	8.8	3.2	7.7	4.2	5.0	28.3	23.6	35.9
Ga	14.6	7.3	17.5	2.7	15.5	1.4	2.8	9.3	13.4	17.0	12.5	13.9
Ge	2.1	1.3	2.9	2.0	1.9	2.1	1.9	1.6	1.3	1.3	1.2	1.1
As	1.7	4.5	0.1	181.8	bdl	31.8	192.0	10.4	7.0	0.4	0.6	0.3
Se	0.30	1.44	0.31	6.56	0.07	6.70	6.25	2.36	0.24	0.03		0.06
Rb	0.2	1.6	0.2	0.1	2.6	0.4	0.2	1.6	0.6	4.8	16.5	24.4
Sr	29	40	21	75	92	16	24	74	40	196	296	166
Y	14.0	10.1	12.0	2.8	12.7	4.2	3.4	8.2	15.5	19.4	20.3	14.3
Zr	37.0	22.7	32.2	2.4	20.0	6.8	3.2	25.5	57.4	52.7	42.2	40.5
Nb	1.33	0.90	1.18	0.08	0.33	0.30	0.11	1.19	1.43	1.56	1.16	1.18
Mo	0.3	1.0	1.2	6.1	0.2	39.9	3.7	0.9	5.4	0.3	0.5	0.4
Ag	0.04	0.02	0.02	0.57	0.02	0.24	0.45	0.06	0.08	0.04	0.02	0.02
Cd	0.1	0.1	0.1	0.7	0.1	0.1	1.8	0.1	0.5	0.3	0.1	0.2
In	0.0	0.0	0.1	2.2	0.1	0.1	3.1	0.1	0.0			
Sn	0.7	0.2	0.5	0.9	0.3	0.3	0.8	0.4	0.7	0.5	0.3	0.8
Sb	0.0	0.1	0.0	1.3	0.0	0.3	1.5	0.1	0.1	0.0	0.1	0.1
Te	0.21	1.47	0.11	1.58	0.02	1.23	0.82	1.10	3.30	bdl	bdl	bdl
Cs	0.01	0.05	0.01	0.01	0.01	0.01	0.01	0.03	0.02	0.10	0.51	0.86
Ba	6.0	29.0	6.9	28.6	38.6	8.0	13.9	28.0	14.4	70.4	49.8	89.4
La	1.67	0.58	1.63	0.44	0.58	0.72	0.62	0.89	1.40	2.16	1.87	1.60
Ce	5.00	1.90	5.00	0.70	1.60	1.30	1.00	3.00	4.70	5.91	4.79	4.45
Pr	0.88	0.35	0.84	0.15	0.29	0.26	0.21	0.56	0.85	0.94	0.80	0.71
Nd	4.90	2.15	4.47	0.80	1.80	1.29	1.07	3.09	4.77	4.87	4.21	3.50
Sm	1.48	0.88	1.42	0.27	0.86	0.37	0.31	1.03	1.62	1.74	1.48	1.29
Eu	0.37	0.16	0.29	0.15	0.39	0.09	0.18	0.26	0.33	0.64	0.57	0.47
Gd	2.23	1.15	1.98	0.39	1.51	0.51	0.43	1.26	2.24	2.48	2.25	1.77
Tb	0.36	0.22	0.31	0.06	0.29	0.09	0.08	0.21	0.39	0.47	0.42	0.33
Dy	2.53	1.55	2.06	0.44	2.07	0.65	0.54	1.36	2.66	3.31	3.05	2.33
Ho	0.54	0.38	0.44	0.10	0.48	0.15	0.12	0.30	0.59	0.72	0.68	0.51
Er	1.70	1.19	1.26	0.29	1.44	0.46	0.37	0.86	1.72	2.26	2.13	1.45
Yb	1.53	1.46	1.18	0.30	1.50	0.51	0.37	0.85	1.82	2.34	2.24	1.55
Lu	0.25	0.21	0.17	0.04	0.23	0.08	0.06	0.12	0.31	0.35	0.36	0.22
Hf	1.17	0.70	1.14	0.07	0.75	0.19	0.09	0.99	1.76	1.48	1.16	1.08
Ta	0.094	0.062	0.084	bdl	0.022	0.021	bdl	0.081	0.096	0.139	0.106	0.100
W	0.24	0.11	0.11	0.06	0.12	0.13	0.06	0.07	0.11	2.09	1.14	0.40
Tl	bdl	0.02	bdl	0.74	0.02	0.40	0.35	0.03	0.00	4.04	10.93	7.12
Bi	0.01	0.01	0.02	0.02	0.02	0.02	0.01	0.01	0.01	0.00	0.00	0.00
Th	0.110	0.066	0.089	0.048	0.076	0.112	0.072	0.064	0.160	0.304	0.248	0.219
U	1.090	0.220	0.142	0.492	0.069	0.204	0.563	0.195	0.426	0.223	0.257	0.170
#Mg		58	69	8	57	7		59	67	64	51	48

Table 3. (*Cont.*)

	SH57-50	SH70-35	SH70-56	SH70-73	SH70-135	SH63-126.5	SH63-47	SH63-51.5	SH63-56.5A	SH63-56.5B
(wt %)	Hanging-wall volcanic			Dolerite			Matrix-supported breccia (MSB)			
SiO_2	49.64	48.18	46.83	48.00	48.80	49.12	57.53	66.57	55.09	68.21
Al_2O_3	14.86	15.38	15.17	15.30	14.77	14.55	2.91	6.94	21.85	9.53
Fe_2O_3	14.38	14.16	13.34	12.67	12.57	12.42	14.95	9.76	11.34	8.41
MnO	0.60	0.15	0.20	0.19	0.16	0.18	0.01		0.08	0.01
MgO	6.63	8.08	9.49	9.01	9.31	10.07	1.81	0.67	9.55	2.36
CaO	4.56	8.98	8.52	8.25	9.93	6.56	0.03	0.04	0.15	0.08
Na_2O	3.35	1.66	1.64	1.61	1.35	2.15				
K_2O	1.35	0.56	1.06	0.89	0.20	0.79	0.01	0.03	0.02	0.06
TiO_2	0.63	0.56	0.60	0.57	0.57	0.57	0.10	0.19	0.92	0.25
P_2O_5	0.05	0.04	0.04	0.04	0.05	0.05	0.01	0.03	0.02	0.09
SO_3	0.02	0.04	0.02	0.04	0.04	0.18	21.18	14.49	0.83	10.35
LOI	3.80	2.02	2.95	3.31	2.13	3.25				
Total	99.86	99.82	99.86	99.87	99.87	99.87	98.55	98.72	99.83	99.35
(µg/g)										
Cu	42	75	40	82	92	81	13,692	11,080	380	5,460
Zn	230	270	49	51	42	49	347	1,020	240	290
Pb	1.5	0.8	0.6	1.2	0.7	2.4	14.9	12.7	0.9	8.4
Li	7	6	7	12	4	10	7	8	17	12
Sc	41	44	41	47	43	43	3	4	27	7
V	294	292	282	284	270	294	64	117	339	224
Cr	35	71	85	72	74	74	5	8	17	18
Co	64	38	31	34	29	32	243	201	53	114
Ni	35.9	36.9	39.7	36.5	36.3	37.5	4.8	10.0	13.7	7.4
Ga	13.9	13.7	13.6	13.7	13.6	12.1	5.0	8.2	13.0	7.1
Ge	1.1	1.1	1.3	0.9	1.0	1.2	2.1	1.6	0.8	1.2
As	0.3	0.4	0.3	0.3	0.2	1.5	59.5	32.5	2.2	40.2
Se	0.06	0.05	0.01	0.04	0.05	0.21	0.18	0.77	0.05	bdl
Rb	24.4	4.8	8.6	6.0	1.7	3.9	0.1	0.1	0.1	0.1
Sr	166	108	102	97	80	85	11	50	23	118
Y	14.3	14.4	13.1	14.5	13.3	14.3	1.5	1.9	3.9	2.9
Zr	40.5	34.4	29.8	32.6	30.0	30.0	4.2	7.3	30.5	7.3
Nb	1.18	0.94	1.00	0.97	0.90	0.90	0.09	0.08	0.32	0.09
Mo	0.4	0.4	0.3	0.5	0.5	0.5	64.3	57.1	2.5	18.3
Ag	0.02	0.02	0.02	0.02	0.02	0.02	1.52	0.74	0.05	0.34
Cd	0.2	0.1	0.0	0.1	0.1	0.1	4.3	8.2	6.0	1.6
In										
Sn	0.8	0.3	0.2	0.3	0.2	0.6	0.7	0.8	0.5	0.4
Sb	0.1	0.2	0.1	0.1	0.0	0.2	1.7	1.0	0.3	0.6
Te	bdl	bdl	bdl	bdl	bdl	0.02	bdl	bdl	bdl	0.84
Cs	0.86	0.04	0.06	0.04	0.07	0.07	0.00	0.00	0.02	0.01
Ba	89.4	32.6	45.3	38.9	20.6	40.6	1.0	1.4	2.1	2.9
La	1.60	1.42	1.23	1.41	1.24	1.31	0.25	0.34	0.43	0.78
Ce	4.45	3.87	3.30	3.74	3.34	3.39	0.63	1.01	1.14	1.97
Pr	0.71	0.62	0.52	0.60	0.54	0.52	0.14	0.22	0.22	0.45
Nd	3.50	3.17	2.72	3.05	2.71	2.84	0.75	1.19	1.13	2.44
Sm	1.29	1.14	1.00	1.12	0.99	1.03	0.27	0.32	0.37	0.57
Eu	0.47	0.43	0.41	0.41	0.41	0.41	0.15	0.17	0.10	0.29
Gd	1.77	1.63	1.54	1.61	1.51	1.56	0.27	0.31	0.51	0.51
Tb	0.33	0.32	0.28	0.31	0.29	0.30	0.05	0.05	0.09	0.09
Dy	2.33	2.21	2.02	2.27	2.02	2.16	0.30	0.33	0.62	0.44
Ho	0.51	0.48	0.47	0.50	0.46	0.48	0.06	0.08	0.14	0.10
Er	1.45	1.52	1.42	1.51	1.41	1.51	0.17	0.20	0.41	0.26
Yb	1.55	1.48	1.49	1.64	1.47	1.57	0.18	0.24	0.53	0.29
Lu	0.22	0.21	0.22	0.24	0.21	0.25	0.03	0.04	0.08	0.04
Hf	1.08	0.97	0.88	0.93	0.87	0.86	0.14	0.24	0.98	0.25
Ta	0.100	0.082	0.087	0.082	0.077	0.074	0.005	0.007	0.024	0.008
W	0.40	0.82	2.03	0.76	0.52	2.06	0.56	2.56	0.55	1.44
Tl	7.12	6.97	6.49	2.15	0.89	5.58	214	430	9.83	84.9
Bi	0.00	0.00	0.00	0.00	0.00	0.00	0.00	0.00	0.00	0.00
Th	0.219	0.208	0.191	0.210	0.192	0.192	0.036	0.029	0.090	0.035
U	0.170	0.173	0.269	0.163	0.138	0.142	1.030	1.347	1.264	1.349
#Mg	48	53	58	58	59	62	19	13	63	37

Notes: MD431-91 is a composite sample collected at an upper (1) and lower (3) volcanic glass rim, whereas (2) is in between; similarly, MD178-92 (1) and (2) are located above and below a volcanic glass rim

Abbreviations: bdl = below detection limit, LOI = loss on ignition

Table 3. (*Cont.*)

	SH63-72	SH63-88	SH63-115	SH63-138.5	SH69-40	SH69-59	SH69-121.5
(wt %)	Clast-supported breccia (CSB)						
SiO_2	56.55	53.01	55.71	48.95	58.90	60.06	56.99
Al_2O_3	4.34	10.82	12.55	16.63	6.05	2.93	11.72
Fe_2O_3	15.73	17.80	17.05	19.40	15.07	14.30	17.88
MnO	0.03	0.12	0.14	0.23	0.03	0.04	0.12
MgO	3.56	9.48	9.18	10.31	4.28	2.47	9.16
CaO	0.15	0.13	0.30	0.48	0.06	0.03	0.33
Na_2O			0.12	0.26			0.05
K_2O	0.02	0.01	0.03	0.30	0.02	0.01	0.01
TiO_2	0.19	0.42	0.72	0.64	0.13	0.05	0.43
P_2O_5	0.02	0.02	0.06	0.05	0.01	0.01	0.06
SO_3	19.09	7.53	3.68	2.26	15.05	18.77	3.08
LOI							
Total	99.68	99.33	99.54	99.50	99.59	98.66	99.83
(µg/g)							
Cu	890	5,590	3,680	3,920	1,940	7,330	810
Zn	1,750	250	90	90	1,600	5,400	200
Pb	35.1	6.0	3.2	1.7	21.1	48.6	2.3
Li	7	8	8	14	6	6	5
Sc	6	19	24	31	8	3	23
V	93	159	223	217	115	57	165
Cr	6	4	6	10	12	24	9
Co	82	136	83	69	91	113	83
Ni	11.7	9.5	6.3	16.5	6.5	7.8	8.6
Ga	4.2	9.0	9.8	11.7	6.9	6.2	10.6
Ge	2.3	1.6	1.6	1.5	1.6	2.0	1.5
As	64.4	18.1	9.5	1.5	50.7	58.3	4.7
Se	bdl	0.22	0.35	0.08	0.15	4.32	0.03
Rb	0.1	0.1	0.2	1.3	0.3	0.0	0.0
Sr	5	4	13	17	8	3	4
Y	1.9	3.6	8.0	9.7	1.3	1.5	5.3
Zr	7.1	19.4	23.9	28.7	4.5	2.8	19.2
Nb	0.09	0.22	0.26	0.38	0.09	0.07	0.23
Mo	13.6	119	17.0	2.7	30.8	35.3	3.7
Ag	0.50	0.31	0.12	0.10	0.69	1.45	0.04
Cd	8.5	0.7	0.2	0.1	10.8	18.9	0.5
In							
Sn	0.3	0.4	0.7	0.7	1.7	0.4	0.3
Sb	2.3	0.3	0.4	0.1	15.4	2.4	0.2
Te	0.75	0.15	bdl	bdl	0.14	bdl	0.92
Cs	0.00	0.01	0.01	0.08	0.05	0.00	0.01
Ba	1.5	3.2	3.2	21.1	1.2	1.7	12.0
La	0.41	0.40	0.65	1.73	0.15	0.33	0.47
Ce	1.09	0.92	2.04	2.90	0.38	0.73	1.64
Pr	0.22	0.19	0.39	0.61	0.08	0.16	0.32
Nd	1.30	0.98	2.32	3.09	0.48	0.84	1.93
Sm	0.39	0.37	0.78	0.93	0.14	0.25	0.62
Eu	0.34	0.13	0.27	0.33	0.05	0.07	0.17
Gd	0.43	0.47	1.26	1.27	0.16	0.24	0.74
Tb	0.06	0.09	0.20	0.22	0.03	0.04	0.13
Dy	0.34	0.69	1.41	1.65	0.22	0.28	0.86
Ho	0.07	0.14	0.30	0.36	0.05	0.06	0.19
Er	0.24	0.40	0.89	1.59	0.14	0.17	0.57
Yb	0.19	0.53	0.91	1.08	0.15	0.14	0.54
Lu	0.03	0.06	0.20	0.16	0.03	0.02	0.08
Hf	0.21	0.58	0.81	0.87	0.16	0.08	0.62
Ta	0.007	0.015	0.023	0.033	0.009	0.005	0.016
W	0.60	0.37	1.55	2.24	3.14	3.10	0.67
Tl	733.2	20.3	68.1	2.48	59.77	341.6	4.66
Bi	0.00	0.01	0.00	0.00	0.00	0.00	0.00
Th	0.029	0.070	0.069	0.146	0.034	0.032	0.055
U	0.940	0.597	0.857	0.411	1.045	1.360	0.333
#Mg	33	53	53	52	38	27	51

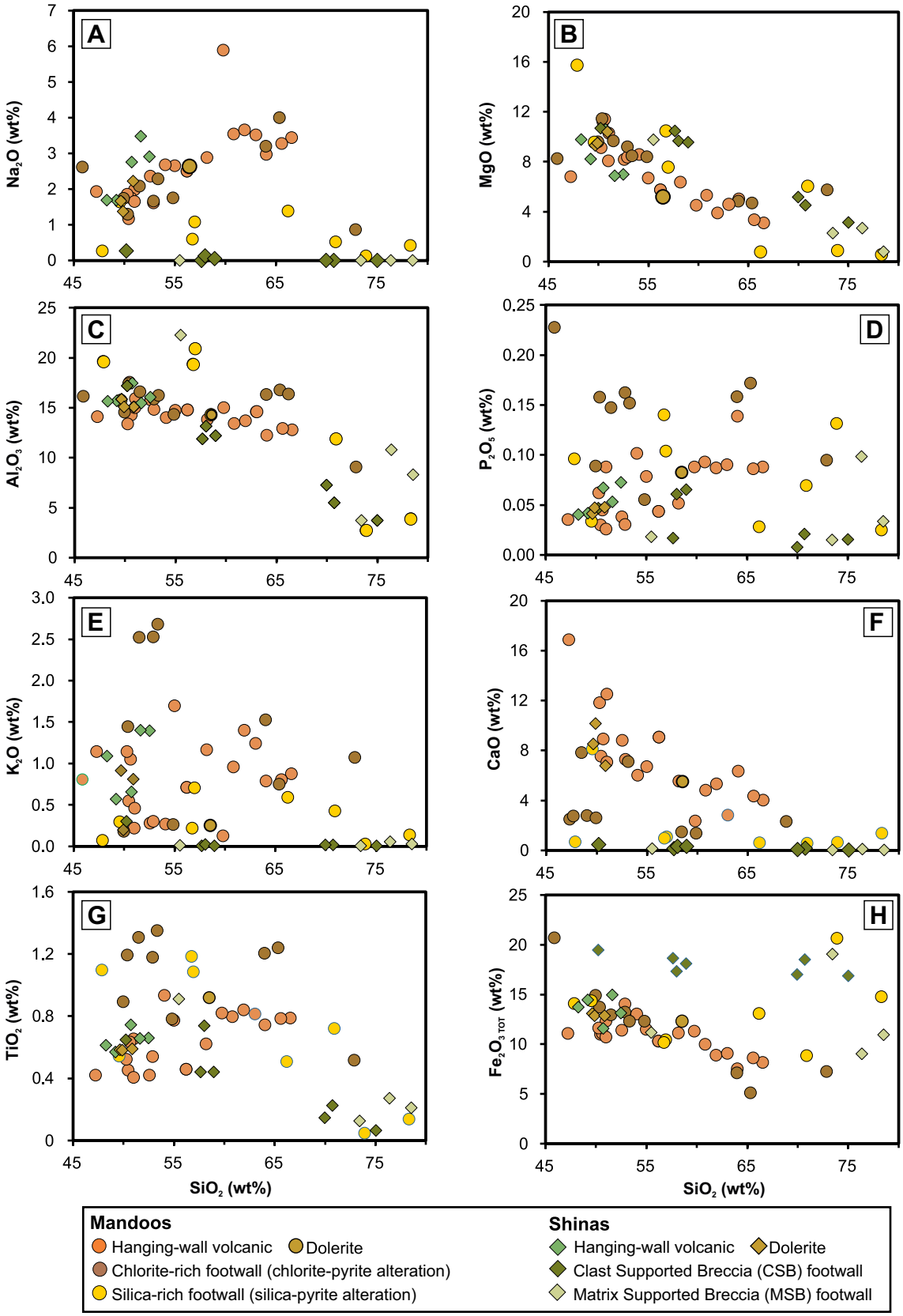

Fig. 9. (A-H) Major element Harker diagrams of the Mandoos and Shinas deposit volcanic rocks.

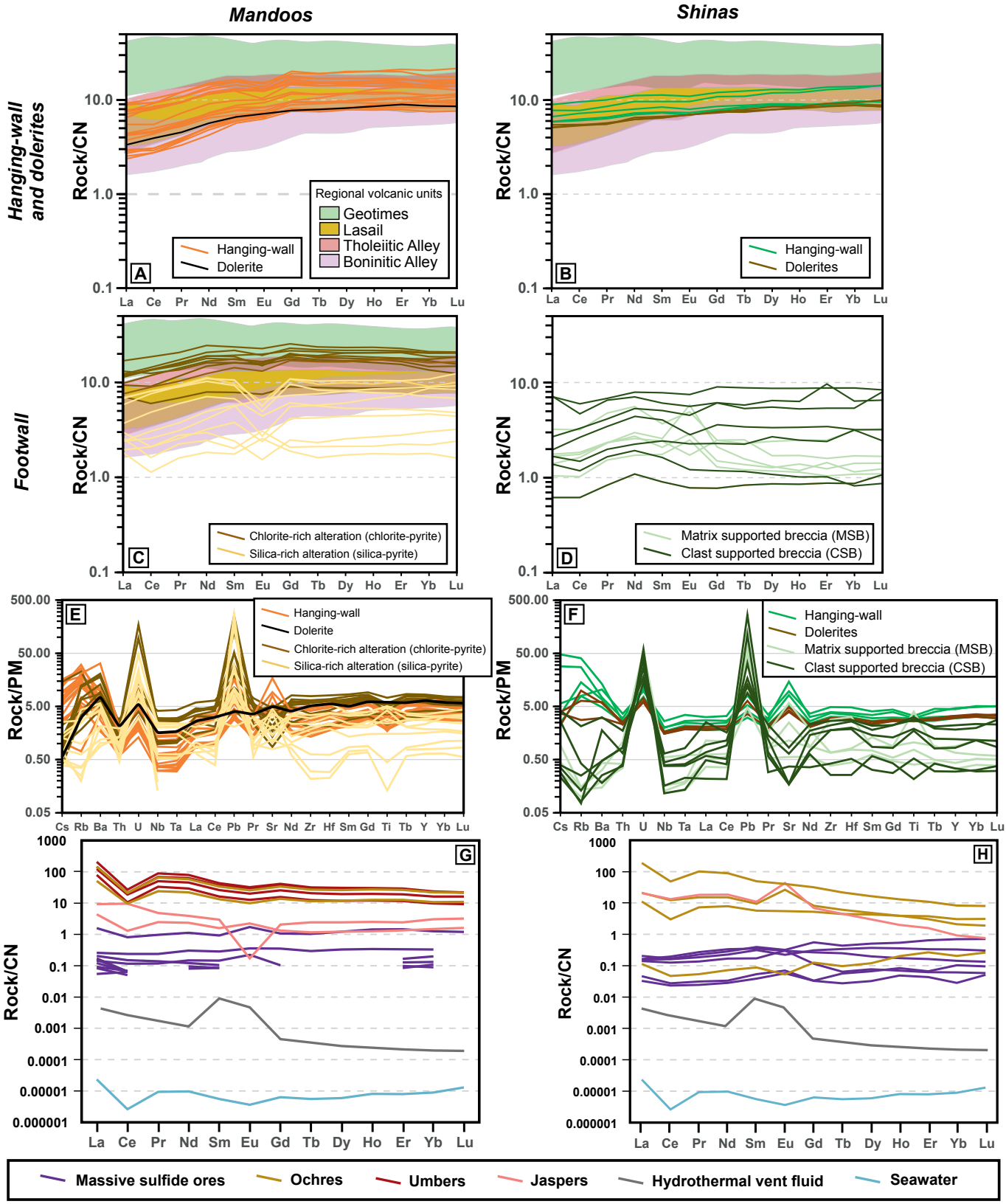

Fig. 10. (A-D) Chondrite (CN)-normalized rare earth element plots (Palme et al., 2014), showing compositional envelopes for the Samail lavas based on data by Godard et al. (2003, 2006), Kusano et al. (2012, 2014), and Belgrano et al. (2019). (E, F) Primitive mantle (PM)-normalized (Palme and O'Neill, 2014) multielemental plots for Mandoos and Shinas lavas. (G, H) Chondrite-normalized rare earth element plots for Mandoos and Shinas massive sulfide ores and metalliferous sediments; seawater and vent fluid from Li and Schoonmaker (2014).

At Shinas, the matrix-supported breccia has higher SiO_2 (Fig. 9, the lower value representing the large basalt clast in Fig. 7F), compared to the clast-supported breccia, which forms a distinctive trend at higher Fe due to its jasper I matrix. Base metal concentrations increase upward toward the ores, being lower in the deeper clast-supported breccia (X = 4,808 µg/g) than in the matrix-supported breccia (X = 8,136 µg/g). Incompatible element abundances consistently decrease with alteration toward the massive ore (Table 3).

Massive sulfide ores

Bulk compositions of massive sulfide ores, ochres, umbers, and jaspers are shown in Table 4.

Mandoos ores straddle the Cu, Cu-Zn, and Zn-Cu fields in the Pb-Cu-Zn classification diagram (App. 6). Excluding Zn-rich ores, average base metal concentrations decrease from Cu (X = 0.70 wt %) to Zn (X = 0.2 wt %) and Pb (X = 82 µg/g). Mandoos massive sulfide ores have low SiO_2, CaO, Al_2O_3, MgO, and alkalis except for a carbonate-cemented breccia.

Shinas ores are SiO_2 rich with high Cu (X = 3.9 wt %), low Zn (X = 274 µg/g), and very low Pb (X = 71 µg/g) grades, plotting in the Cu and Cu-Zn fields toward the Cu-rich apex (App. 6); the oxidized chalcocite ore has very high Cu (up to 28 wt %). Bulk low concentrations in Al_2O_3, MnO, MgO, CaO, and Sr are consistent with the absence of carbonates (Table 4).

Trace element concentrations for Mandoos pyritic ores show higher enrichment in Mn and Te compared to the ores from Shinas, which is more enriched in Cu + Co + Mo (Table 4). Mandoos Zn ores have distinctively higher Ba, Sr, Cd, Mn, Mo, and Ga and lower Co and As concentrations (Table 4). The REE concentrations for all massive sulfides are very low, except in Mandoos carbonate-cemented breccia (Fig. 10). Chondrite-normalized patterns show predominantly positive Eu anomalies (Eu* = 0.68–2.15) and faint negative Ce anomalies (Ce* = 0.46–1.02). Mandoos ores show distinctive LREE enrichment (La/Sm_{CN} X_{MD} = 1.57) relative to those from Shinas, which are uniformly depleted in LREEs (X_{SH} = 0.67).

Jaspers, umbers, and ochres

The umbers and ochres display high Fe_2O_3, a wide range of SiO_2 and CaO, and MnO concentrations one order of magnitude higher than the massive sulfide ores (Table 4). Higher CaO, Sr, Ba, and SO_3 in the umbers is consistent with the occurrence of carbonates and sulfates, which are eventually base metal bearing (Table 4).

Jaspers show MnO and Fe_2O_3 abundances within the lower range of the sulfide ores and concentrations for other major elements below 1 wt %. The Mandoos pyrolusite-rich jasper represents an Fe-poor Mn ore, with higher Sr, Mo, and Ba concentrations and low base metal grades. Sulfide-bearing jaspers have low SiO_2 and high Cu and As, similar to the sulfide ores (Table 4).

Rare earth element patterns are distinctive for each lithological group. The umbers and ochres have high REEs ($2–207_{X_{CN}}$), coherent patterns characterized by negative Ce anomalies (Ce* = 0.18–0.64), subtle LREE enrichments, and gently negative sloped patterns with mild negative Eu anomalies (Fig. 10). The oxidized sulfide and gossan in Shinas have REE contents identical to that of the massive sulfide ores. One ochre from Shinas has a pattern akin to jasper II, which originally crosscut the ores (Fig. 7B). All jaspers display slight LREE enrichments (La/Sm_{CN} 1.89–3.12) and positive Eu anomalies, like those of the sulfide ores; only the Mn jasper shows a pronounced negative Eu anomaly.

The oxidation profile in Shinas shows distinct enrichments downhole: the ochres are enriched in Te, Cr, Ga, Se, Ni, Pb, and Sb. The underlying gossan has ore-like REE patterns and more restricted enrichment in Cr, Se, Zn, and Ag, whereas the oxidized (chalcocite) ore shows mild Ni + Se enrichment (Table 4).

Mine assay data

Statistical parameters are listed in Table 1, and binary plots can be found in Appendix 7; Figure 11 depicts downhole variations for selected drill cores.

Mandoos massive sulfide ores have an average Fe grade close to pyrite ideal composition, contrasting with Shinas, which comprises high proportions of quartz-rich sulfide ores (silica massive sulfide); similar relationships characterize footwall rocks. Copper grades in the massive sulfides are higher in Shinas where they show no correlation with Zn ($r^2 \sim 0.01$; Apps. 7, 8), whereas Zn grades are consistently higher in Mandoos (Table 1) and increase with Cu ($r^2 = 0.3$). The Cu-Pb-Zn classification diagram (App. 6) reveals a spectrum between Cu- and Zn-rich ores for Mandoos and a wider extent of Zn enrichment for Shinas compared to our samples. Different Au grades in silica-sulfide and massive sulfide ores in Shinas (Table 1) result in a weighted average grade for the orebody of 0.63 µg/g (≤4.4 µg/g). Shinas ores are more Au rich compared to Mandoos (X = 0.18 µg/g, ≤2.1 µg/g; Table 1) where Au grades correlate with increasing Cu (r^2= 0.36; Apps. 7, 8). The extended database for Shinas shows that Au grades increase with Pb, Ag, and As (Apps. 7, 8).

Assessment of downhole metal grade variations in the thickest massive sulfide accumulation in Mandoos (Fig. 11A) shows that Cu grades are below <1 wt % in the lower third of the ore lens, peak to ~6 wt % beneath an Fe sediment level, and steeply decrease upward to <0.1 wt %. Zinc grades are more scattered and faintly increase at the top. Gold distribution follows a pattern similar to that of Cu. Figure 11B additionally shows that Cu grades drop sharply (<1 wt % Cu) beneath the massive ores and are coupled with Zn + Au variations leading to gold/base metal ratios <<1. Shinas Cu grades increase throughout the footwall and remain constant or decrease upward in the silica-rich and massive sulfide, respectively (Fig. 11D, E). Gold, Pb, and As increase steadily upward leading to gold/base metal ratios >1 in the (silica-)massive ores.

Outlying Cu concentrations (≤33.9 wt % Cu; Table 1) in both deposits are related to secondary Cu + Au enrichment as is observed in the sampled drill core SH70 (Fig. 11C). Nevertheless, even where gossan and Fe sediments are absent (e.g., Fig. 11B), Cu + Au and Cu/Zn enrichments are observed at the top of the ores. In Shinas, Mn concentrations decrease from the Fe sediments to the gossans, which can be distinguished by their higher Fe/Mn ratio, gold (X = 0.88 ± 1.49 µg/g, ≤11.70 µg/g), and low base metal grades (Table 1; Fig. 11C, D). Nevertheless, some Fe sediments have high Au grades (X = 0.10 ± 0.50 µg/g, ≤5.3 µg/g).

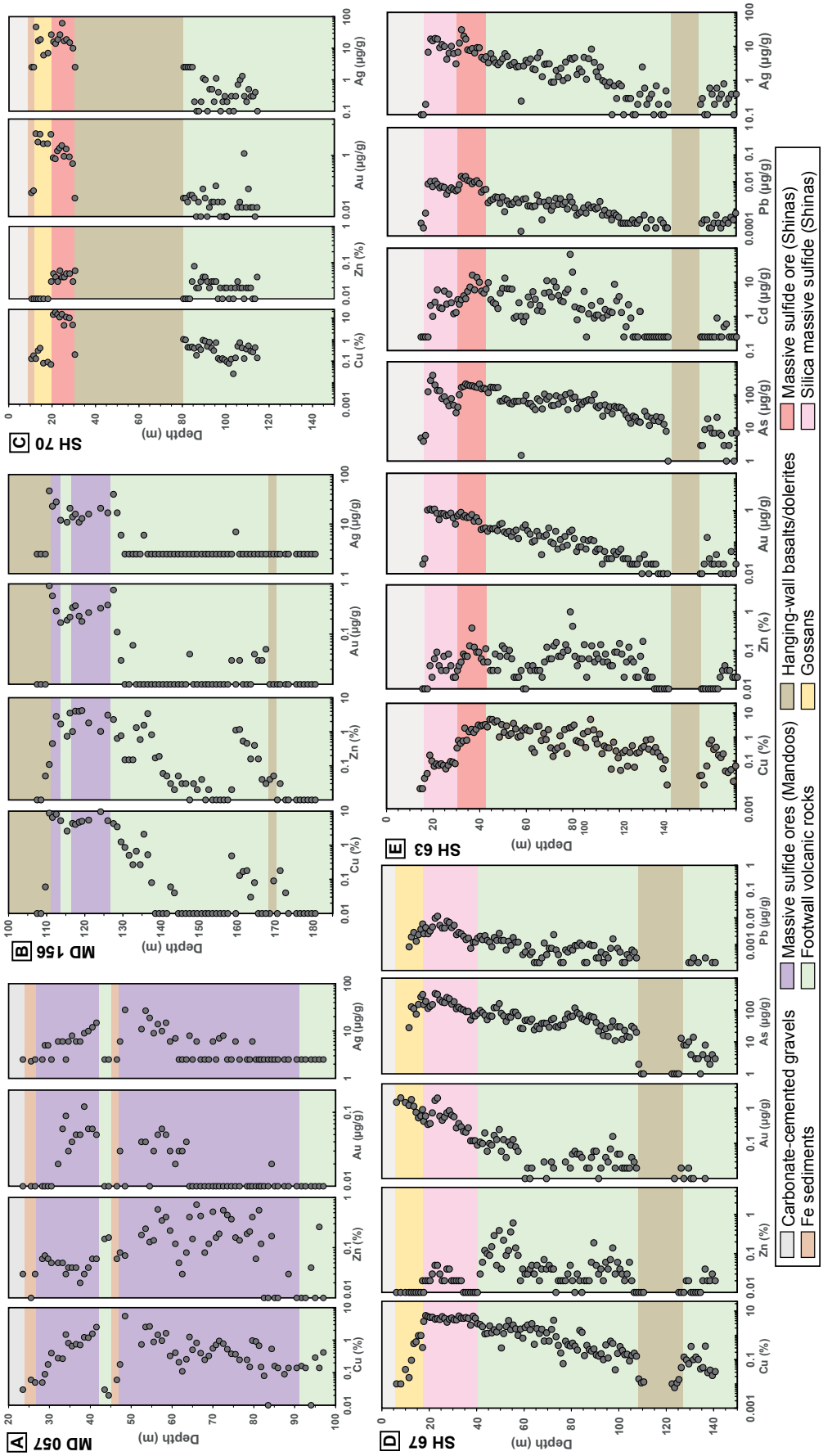

Fig. 11. Downhole metal variations in selected drill cores for Mandoos (A, B) and Shinas (C-E). Additional plots are provided in Appendix 7.

Table 4. Whole-Rock Geochemical Composition of Ores and Metalliferous Sediments of Mandoos (MD) and Shinas (SH)

	MDNP-1	MD178-128.8	MDP3-4-1	MDP1-1-1	MD174-79.0	MD429-109.1	MD431-107.0	MD431-108.0	MD431-109.7	MD431-110.5
	Massive sulfide									
(wt %)	Zn-rich		Carbonate-rich				Pyrite breccias			
SiO_2	13.05	15.55	3.04	0.39	12.25	-	17.02	18.74	17.07	14.46
Al_2O_3	6.41	1.95	1.32	0.14	0.38	-	0.05	0.07	0.05	0.06
Fe_2O_3	4.94	29.48	30.63	37.97	32.58	-	29.58	29.96	29.88	31.79
MnO	0.06	0.02	0.26	0.01	0.01	-	0.01	0.01	0.02	0.01
MgO	0.35	0.21	0.11		0.42	-	0.04	0.04	0.04	0.00
CaO	1.75	0.59	19.53	0.03	0.04	-	0.02	0.02	0.03	0.04
Na_2O		0.13		0.07	0.09	-		0.05	0.10	0.07
K_2O	0.06	0.05	0.03	0.01	0.05	-	0.01	0.01	0.01	0.01
TiO_2	0.02				0.01	-				
P_2O_5			0.04			-				
SO_3	37.81	49.81	44.21	60.76	53.81	-	52.10	49.84	52.25	52.96
Sum	64.43	97.77	99.17	99.36	99.64	-	98.82	98.75	99.44	99.41
(µg/g)										
Cu	30,870	9,650	6,550	4,980	2,200	-	11,010	11,790	4,420	5,380
Zn	322,940	12,280	610	1,060	140	-	580	250	920	320
Pb	34.2	116.2	34.9	53.3	43.7	21.4	153.6	220.0	53.2	92.0
Li	0.3	4.2	0.1	0.0	7.2	5.8	2.6	4.3	1.5	1.0
Sc										
V	66	34	23	9	9	56	62	67	21	54
Cr	0.8	4.3	8.2	0.8	4.5	4.6	11.2	9.3	3.5	4.7
Co	0.7	33.4	225.6	42.1	106.5	422.6	14.4	88.4	9.8	29.4
Ni		7.9	7.2	8.1	4.7	3.7	10.6	15.1	1.6	9.6
Ga	166.3	12.5	1.5	2.6	2.2	8.8	12.0	6.4	9.2	6.2
Ge	0.8	6.4	4.5	5.5	6.0	6.4	6.0	5.3	4.9	4.1
As	60	476	324	1,024	245	265	304	281	343	274
Se	1.97	3.76	11.57	6.09	43.28	25.85	2.04	5.73	1.76	2.46
Rb	0.28	0.32	0.34	0.03	0.61	0.04	0.08	0.14	0.06	0.05
Sr	13.3	90.7	20.0	0.5	4.5	0.6	0.5	0.6	0.8	0.5
Y	0.5	0.1	3.7	0.0	0.2	0.1	0.1	0.3	0.1	0.1
Zr	1.0	0.1	0.4	0.1	0.2	0.1	0.2	0.3	0.1	0.1
Nb	0.02		0.01		0.01	0.02	0.02	0.04	0.01	
Mo	108.3	26.5	17.6	8.1	3.4	1.6	8.0	3.3	2.5	4.0
Ag	1.69	0.37	1.06	0.19	0.24	0.23	0.87	0.96	0.64	0.87
Cd	2,278	53.4	2.4	3.7	1.2	0.3	3.1	2.1	4.4	1.2
In	21.0	0.6	0.9	3.1	1.5	2.4	9.2	16.6	5.2	7.0
Sn	3.36	0.31	0.37	2.55	18.64	5.69	23.41	24.27	6.44	8.98
Sb	27.31	5.55	1.80	6.58	7.64	2.04	7.52	6.12	6.74	4.27
Te	0.40	3.44	14.00	27.46	5.79	21.78	10.93	15.39	3.09	28.58
Cs	0.04	0.02	0.02		0.02			0.02		
Ba	2.2	35.0	0.8	0.1	6.3	0.1	0.3	0.7	0.3	0.3
La	0.06	0.03	0.38	0.01	0.04	0.04	0.03	0.05	0.02	0.02
Ce	0.15	0.04	0.50	0.04	0.04	0.04	0.07	0.09	0.03	0.04
Pr	0.02		0.09				0.01	0.01		
Nd	0.13	0.03	0.49	0.03	0.04	0.04	0.06	0.05	0.03	0.03
Sm	0.04		0.14		0.01	0.01	0.02	0.02		
Eu	0.02		0.10				0.01			
Gd	0.07		0.22		0.02	0.02	0.02	0.03		
Tb	0.01		0.04							
Dy	0.08	0.01	0.31		0.02	0.02	0.02	0.03	0.01	0.01
Ho	0.02		0.08							
Er	0.06		0.24		0.02	0.01	0.02	0.03		
Yb	0.06	0.01	0.21		0.02	0.02	0.02	0.03		
Lu			0.03							
Hf	0.03		0.01							
Ta										
W	0.25	0.12	0.04	0.04	0.02	0.04	0.13	0.05	0.10	0.08
Tl	0.16	7.77	3.13	3.64	1.76	0.34	2.73	5.07	2.53	4.20
Bi	0.013	0.013	0.013	0.019	0.015	0.014	0.014	0.017	0.016	0.014
Th			0.005					0.024		
U	0.021	0.660	1.648	1.381	0.027	0.043	0.320	0.126	0.053	0.092

Table 4. (*Cont.*)

	MD178-110.5	MDP2-2A	MDP2-2B	MD178-134.2	MD429-104.0	MD174-62.15	MD 150.114.1	MDNP -3	SH63-23	SH63-34
	Umber						Jasper		Massive sulfide	
(wt %)	HW	FW			Ochre		Mineralized	Mn-rich	Silica-rich	
SiO_2	52.18	48.04	36.32	43.06	19.14	26.26	37.26	35.04	36.17	45.12
Al_2O_3	3.07	3.84	3.36	2.28	2.20	3.71	0.55	0.36	0.11	0.19
Fe_2O_3	26.82	28.92	37.22	31.54	53.85	58.18	23.07	0.77	24.96	21.51
MnO	2.18	0.74	0.48	0.22	0.44	0.40	0.01	59.59		
MgO	1.72	2.34	2.06	1.43	1.91	2.38	0.00	0.21		0.06
CaO	8.52	13.54	6.52	1.11	10.10	2.80	0.18	0.34	0.01	0.02
Na_2O	0.80		0.31					0.78	0.01	
K_2O	0.47	0.34	0.34	0.07	0.07	0.14	0.03	0.21		0.01
TiO_2	0.15	0.17	0.17	0.06	0.06	0.13	0.01	0.02		
P_2O_5	0.95	1.36	0.92	0.90	1.39	1.51	0.15	0.18		0.01
SO_3	2.76	0.50	11.99	14.76	9.99	4.01	36.97	1.32	38.56	31.40
Sum	99.61	99.79	99.68	95.43	99.15	99.52	98.23	98.81	99.82	98.32
(µg/g)										
Cu	1,500	180	180	41,990	5,650	1,250	15,770	130	1,240	16,200
Zn	1,130	550	550	1,510	1,150	840	340	120	370	160
Pb	75.6	40.7	35.1	271.7	106.5	95.6	26.5	0.5	109.4	44.9
Li	21.2	11.2	13.2	6.6	9.5	14.6	6.2	2.6	1.5	3.4
Sc	4.6	4.1	5.2	2.3	4.7	2.1		0.4		
V	165	343	778	571	931	408	63	371	3	4
Cr	15.6	83.7	70.3	71.3	95.2	51.9	15.9	16.2	6.9	7.0
Co	27.6	5.3	8.5	48.9	76.7	114.8	33.5	101.7	7.1	213.2
Ni	185.4	72.1	99.4	73.1	130.2	35.1	8.4	169.2	3.2	2.2
Ga	3.9	11.5	11.6	48.9	49.5	13.9	2.5	12.8	1.8	0.8
Ge	2.8	2.9	6.0	8.7	6.3	4.0	4.3	2.0	3.3	3.5
As	383	67	166	322	229	204	491	84	114	95
Se	0.20	0.10	0.20	1.33	0.78	18.85	4.05	0.11	0.09	0.48
Rb	4.37	10.71	13.25	1.83	5.07	0.91	0.16	0.58	0.02	0.06
Sr	116	117	62	36	60	51	2.3	447	1.4	5.9
Y	60.0	40.9	55.9	28.0	57.3	27.0	2.4	2.0	0.1	0.2
Zr	33.9	27.3	34.0	14.4	30.9	12.1	2.7	1.5	0.1	0.1
Nb	2.74	1.83	2.40	1.09	2.35	0.91	0.18	0.13	0.01	0.01
Mo	0.4	1.2	1.4	14.7	13.4	10.5	83.1	248.0	26.4	60.9
Ag	0.02	0.02	0.02	0.33	0.02	0.60	0.59	0.00	4.83	0.89
Cd	2.7	0.1	0.0	0.4	0.0	3.9	1.5	0.2	2.5	1.5
In	0.6	1.3	0.7	4.8	4.3	2.9	2.1	0.0	-	-
Sn	2.27	3.24	3.70	3.13	3.98	1.99	1.64	1.15	0.98	0.53
Sb	1.16	0.77	1.31	4.43	2.82	1.61	5.15	1.28	4.25	2.39
Te	0.33	0.56	0.83	1.43	5.81	6.20	1.98	0.02	0.05	
Cs	0.26	0.68	0.89	0.11	0.35	0.04		0.02	0.00	0.01
Ba	78.8	27.1	28.5	9.1	25.4	17.1	1.5	742.5	0.2	0.7
La	50.07	29.25	34.58	18.80	34.97	12.10	1.04	2.21	0.03	0.04
Ce	16.50	11.60	12.90	6.50	12.90	6.00	0.80	5.90	0.08	0.12
Pr	8.22	4.68	6.33	3.12	6.08	2.22	0.23	0.45	0.01	0.03
Nd	34.13	19.72	27.08	12.70	25.29	9.51	1.02	1.70	0.07	0.14
Sm	6.62	3.94	5.59	2.47	5.14	2.04	0.24	0.45	0.03	0.05
Eu	1.89	1.17	1.74	0.74	1.49	0.58	0.13	0.01	0.02	0.02
Gd	8.38	5.24	7.49	3.20	6.89	2.83	0.27	0.42	0.02	0.06
Tb	1.20	0.78	1.09	0.47	1.01	0.43	0.04	0.09	0.00	0.01
Dy	7.80	4.89	7.08	3.02	6.61	3.02	0.31	0.62	0.02	0.05
Ho	1.70	1.11	1.57	0.68	1.52	0.71	0.07	0.14	0.00	0.01
Er	4.81	3.12	4.51	1.93	4.34	2.07	0.22	0.40	0.01	0.03
Yb	3.96	2.73	3.73	1.63	3.70	1.79	0.25	0.51	0.01	0.02
Lu	0.54	0.40	0.55	0.23	0.53	0.27	0.04	0.08	0.00	0.00
Hf	0.66	0.58	0.69	0.25	0.60	0.21	0.05	0.04		0.00
Ta	0.159	0.116	0.140	0.057	0.129	0.050	0.011		0.001	0.000
W	0.55	1.15	1.62	2.13	1.64	0.92	0.17	1.70	0.92	0.88
Tl	0.12	0.08	0.11	0.41	0.07	0.33	8.84	1.35	283.14	432.70
Bi	0.017	0.015	0.014	0.011	0.013		0.014	0.016	0.004	0.003
Th	2.189	1.712	1.828	0.706	1.633	0.606	0.137	0.046	0.001	0.002
U	0.728	0.883	0.692	4.092	2.657	2.837	1.245	5.585	0.548	1.065

Table 4. (*Cont.*)

	SH63-39	SH63-43.5	SH70-20.9	SH70-22.5	SH70-19	SH70-11.3	SH70-13.5	SH69-4	SH70-14	SH63-26
	Massive Sulfide									
(wt %)	Silica-rich		Cu-rich (chalcocitic)		Gossan	Ochre			Jasper II	
SiO_2	36.41	37.10	7.85	17.04	31.80	57.05	53.87	49.92	92.66	76.09
Al_2O_3	0.26	2.47	0.19	0.09	0.08	2.38	2.90	0.93	0.24	0.53
Fe_2O_3	23.18	22.86	20.95	27.35	44.39	36.12	34.41	42.25	5.18	20.22
MnO					0.03	1.70	0.57	0.27	0.01	0.00
MgO	0.10	0.98	0.05		1.35	0.70	1.65	0.77	0.11	0.11
CaO	0.03	0.03	0.01	0.01	20.91	0.27	4.89	4.78	0.14	0.16
Na_2O						0.06	0.05	0.03	0.02	0.04
K_2O	0.01	0.01	0.01			0.33	0.13	0.03	0.02	0.02
TiO_2	0.01	0.03				0.26	0.04	0.01	0.01	0.01
P_2O_5			0.03	0.01	0.03	0.42	0.08	0.46	0.02	0.25
SO_3	36.83	33.02	42.69	43.86	0.76	0.31	0.45	0.27	1.32	1.30
Sum	96.82	96.49	71.77	88.36	99.34	99.60	99.03	99.71	99.72	98.73
(µg/g)										
Cu	30,580	34,230	280,500	114,530	840	1,460	6,850	840	1,950	350
Zn	410	190	260	240	650	110	150	30	40	38
Pb	61.7	22.3	87.1	100.4	80.5	195.6	92.6	30.4	-	22.3
Li	7.1	6.7	0.1	1.5	0.7	15.1	10.0	9.5	-	12.9
Sc		0.4				5.3	1.7		-	0.6
V	5	49	11	9	1,947	364	343	255	-	166
Cr	0.9	2.2	0.2	0.9	111.3	49.3	11.5	16.3	-	36.5
Co	207.6	205.8	284.2	268.1	175.9	34.9	110.7	1.6	-	4.6
Ni	6.3	3.4	13.4	13.5	3.1	28.0	16.4	7.8	-	2.4
Ga	1.6	4.2	0.9	1.2	0.7	19.8	8.6	3.2	-	15.4
Ge	2.6	3.4	2.4	3.6	3.9	4.2	2.5	2.8	-	2.0
As	134	136	141	236	213	44	209	22	-	19
Se	0.37	0.88	1.14	0.44	2.09		1.62	0.04	-	0.10
Rb	0.13	0.09	0.00	0.03	0.05	10.34	1.87	0.19	-	0.17
Sr	4.2	3.7	0.6	1.1	854	875	163	1,105	-	168
Y	0.6	0.9	0.1	0.1	1.3	15.9	6.6	6.0	-	2.9
Zr	1.0	2.0	0.5	0.2	0.6	56.3	3.6	2.2	-	2.3
Nb	0.02	0.03	0.01	0.01	0.01	4.56	0.26	0.06	-	0.14
Mo	109.0	148.5	118.2	64.5	14.5	5.7	74.7	3.4	-	4.8
Ag	1.60	1.02	3.04	4.90	5.86	0.08	3.69	0.07	-	0.17
Cd	4.4	7.2	2.3	1.5	1.5	0.4	1.4	0.2	-	0.3
In	-	-	-	-	-	-	-	-	-	-
Sn	0.89	0.97	1.04	0.61	2.40	2.67	2.83	0.11	-	1.91
Sb	3.62	1.45	6.23	7.77	3.40	6.70	12.55	1.39	-	1.22
Te	0.05	3.52	0.64	2.67	2.00	adl	4.73		-	0.15
Cs	0.03	0.01	0.00	0.01	0.01	0.81	0.29	0.02	-	0.01
Ba	0.8	0.4	0.3	0.8	27.8	146.9	232.0	29.8	-	3.3
La	0.04	0.05	0.01	0.01	0.03	45.37	2.67	5.06	-	4.96
Ce	0.10	0.10	0.02	0.01	0.03	29.59	1.84	7.50	-	8.14
Pr	0.02	0.02	0.00	0.00	0.00	9.44	0.68	1.42	-	1.70
Nd	0.10	0.12	0.01	0.01	0.03	38.62	3.43	6.57	-	8.05
Sm	0.05	0.06	0.01	0.01	0.01	7.55	0.87	1.44	-	1.67
Eu	0.01	0.02	0.00	0.00	0.00	2.35	0.32	1.56	-	2.53
Gd	0.06	0.11	0.01	0.01	0.03	6.54	1.07	1.68	-	1.42
Tb	0.01	0.02	0.00	0.00	0.00	0.82	0.17	0.23	-	0.17
Dy	0.09	0.13	0.02	0.01	0.03	4.17	1.08	1.22	-	0.76
Ho	0.02	0.03	0.00	0.00	0.01	0.73	0.22	0.22	-	0.11
Er	0.06	0.11	0.01	0.01	0.04	1.80	0.62	0.50	-	0.26
Yb	0.06	0.12	0.02	0.00	0.03	1.38	0.51	0.35	-	0.15
Lu	0.01	0.02	0.00	0.00	0.01	0.20	0.08	0.05	-	0.02
Hf	0.02	0.06	0.01	0.00	0.00	1.30	0.09	0.03	-	0.03
Ta	0.001	0.002	0.000	0.001	0.002	0.331	0.019	0.003	-	0.009
W	1.61	0.44	0.60	1.55	3.69	35.81	8.11	8.85	-	22.55
Tl	110.55	161.05	179.24	452.70	10.04	114.03	169.23	7.01	-	20.48
Bi	0.004	0.003	0.003	0.002	0.004	0.004	0.004	0.003	-	0.003
Th	0.017	0.013	0.008	0.002	0.007	4.173	0.213	0.042	-	0.115
U	0.863	1.086	0.415	0.289	2.952	1.560	0.761	1.656	-	2.839

Abbreviations: blanks = below detection limit, - = not analyzed, adl = above upper detection limit, FW = footwall, HW= hanging-wall, LOI = loss on ignition

Sphalerite Geothermometry

We applied the empirical sphalerite geothermometer of Keith et al. (2014), which has been successfully employed to constrain the temperature of hydrothermal fluids in VMS/SMS deposits. Analyses with Cu > 2 wt % were excluded, since they reflect chalcopyrite microinclusions/exsolutions (Keith et al., 2014). Some high-Fe inclusions in pyrite from Shinas fall within the sediment-covered field and were also excluded from the geothermometric calculations (App. 4; Keith et al., 2014). All other sphalerite analyses fall within the sediment-starved basins field, where Fe/Zn ratios increase systematically with hydrothermal fluid temperatures (Keith et al., 2014). Sphalerite from Mandoos ores yielded average temperatures of 252 ± 29°C, which overlap with those obtained for the footwall (X = 242 ± 9°C). Sphalerite from Shinas ranges from 246 ± 18°C (lower FeS mol %) to higher temperatures of 285 ± 52°C for early inclusions with higher FeS mol %.

Isotope Geochemistry

Neodymium-strontium isotope measurements provide constraints on the volcanostratigraphic positioning of each deposit (Table 5). Mandoos samples were selected from drill core MD150 (Fig. 2): (1) from the hanging wall ~17.6 m above the ore (MD150-88.7) and at the interface with the massive sulfide (MD150-105.8) and (2) from the mildly silicified footwall 14.8 m below the massive sulfide (MD150-126.7). Samples from Shinas hanging wall (MD57-50) and dolerite (SH70-135) were also analyzed (Fig. 6).

Interaction with seawater at low to moderate water/rock ratios (W/R ≤ 1,000) preserves Nd isotope compositions due to the low concentration of Nd in seawater but causes $^{87}Sr/^{86}Sr$ shifts toward increasingly radiogenic compositions (Fig. 12). Footwall rocks in both deposits show decreases in alkalis and REE concentrations relative to typical MORB abundances, featuring negative Ce anomalies indicative of seawater interaction. While the Mandoos chlorite-rich footwall preserves magmatic-like REE patterns, the extent of leaching in Shinas breccias suggests that Nd isotope compositions are unlikely to reflect original magmatic ratios; therefore, measurements were not attempted.

Figure 12 shows distinct $\varepsilon_{Nd_{initial\,(i)}}$ values for both deposits: Mandoos has a more radiogenic and homogeneous sig-

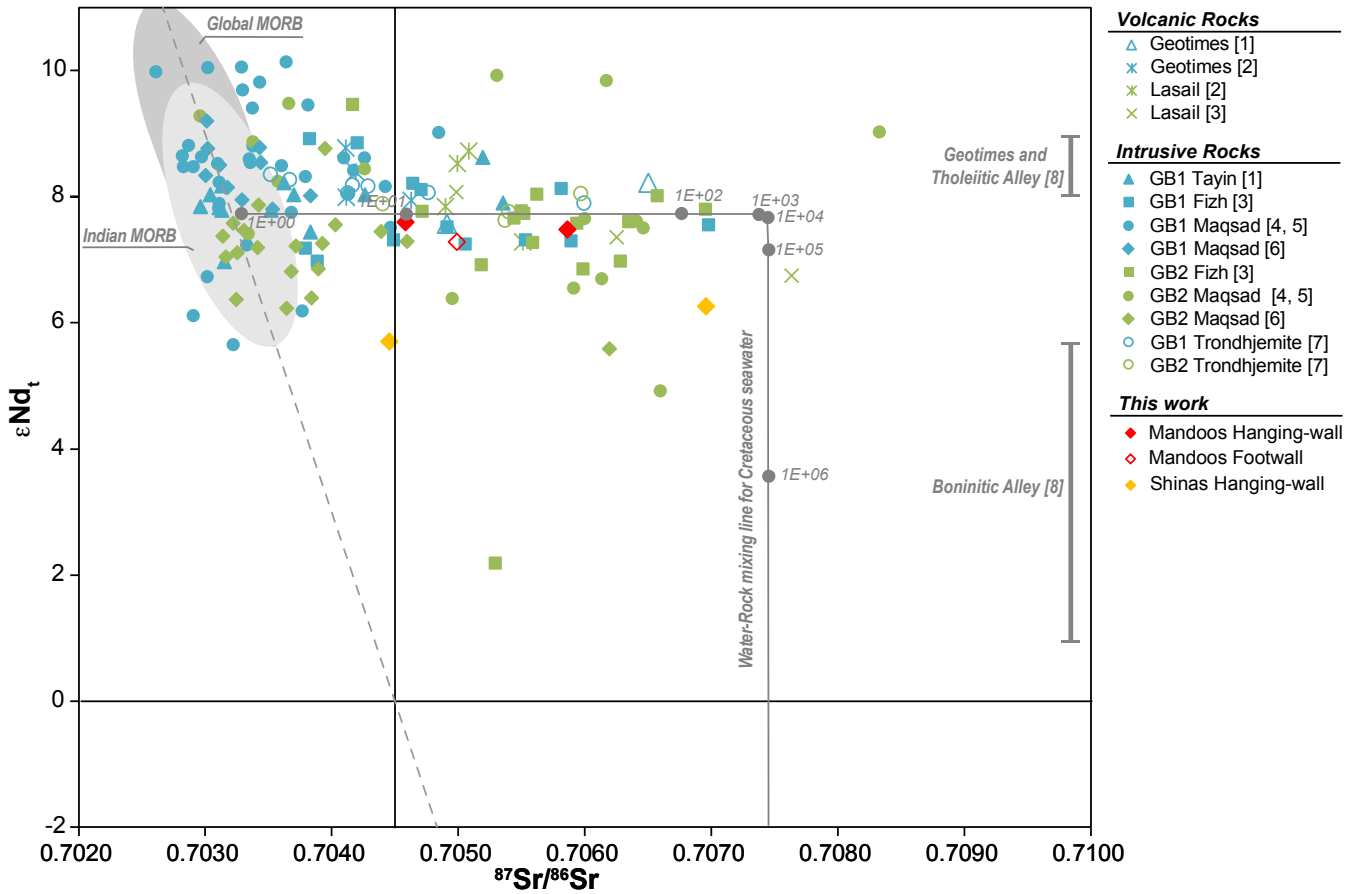

Fig. 12. ε_{Nd_t} versus Sr isotope ratios showing the water/rock mixing line following McCulloch et al. (1981) departing from average Indian mid-ocean ridge basalt (MORB). Values for Sr and Nd concentrations in seawater from Li and Schoonmaker (2014) and for Cretaceous $^{87}Sr/^{87}Sr$ seawater from Jones and Jenkyns (2001). The ε_{Nd} for Indian Ocean seawater is from Goldstein and Hemming (2014) and for global and Indian MORB from White and Klein (2014). Data sets for Oman rocks recalculated to 95 Ma: 1 = McCulloch et al. (1981), 2 = Godard et al. (2006), 3 = Tsuchiya et al. (2013), 4, 5 = Benoit et al. (1996, 1999), 6 = Nicolle et al. (2016), 7 = Haase et al. (2016), 8 = ε_{Nd_i} range for Geotimes (LV1), Tholeiitic Alley (LV2), and Boninitic Alley (UV2) from Kusano et al. (2017).

Table 5. Isotopic Data for Mandoos (MD) and Shinas (SH)

Sample	Unit	$^{143}Nd/^{144}Nd$	2σ	Nd (μg/g)	Sm (μg/g)	$^{147}Sm/^{144}Nd$	$^{143}Nd/^{144}Nd_i$	ε_{Nd_i}	$^{87}Sr/^{86}Sr$	2σ	Rb (μg/g)	Sr (μg/g)	$^{87}Rb/^{86}Sr$
MD-150-88.7	Hanging-wall volcanic	0.513056	4	2.99	1.20	0.243	0.512905	7.6	0.704580	5	10.8	87	0.349
MD-150-105.8	Hanging-wall ore interface	0.513045	3	4.99	1.93	0.234	0.512900	7.5	0.705859	5	12.5	345	0.102
MD-150-126.7	Footwall	0.513003	4	4.90	1.48	0.183	0.512889	7.3	0.704987	5	0.2	29	0.020
SH70-135	Dolerite dikes	0.512946	5	2.71	0.99	0.222	0.512808	5.7	0.704452	7	1.7	80	0.059
SH57-32.5	Hanging-wall volcanic	0.512971	6	4.87	1.74	0.216	0.512837	6.3	0.706955	4	4.8	196	0.068

nature (7.3–7.6) relative to Shinas, which displays lower ε_{Nd_i} values (5.7–6.3). The $^{87}Sr/^{86}Sr$ ratios for Mandoos are higher (0.705859) at the interface between the massive sulfide and the hanging-wall lavas and lower (0.704580) above the ore. The hanging-wall lavas in Shinas show more radiogenic $^{87}Sr/^{86}Sr$ (0.706955) than the dolerite (0.704452), consistent with the degree of alteration recorded in each rock type and the occurrence of Fe-Mn carbonate veins in the lavas. The ε_{Nd_i} values for the dolerite dikes are identical to those of the hanging-wall lavas, supporting, along with remaining evidence, that the dikes are the feeders to the hanging-wall sequence.

Discussion

Volcanostratigraphy of the Mandoos and Shinas VMS deposits

Distinguishing V1 from V2 lavas based on several discriminant diagrams proposed in the literature (Fig. 13A-D) is relatively straightforward because of their distinct enrichment in incompatible elements. In contrast, assigning the exact V2 unit (Lasail, Tholeiitic, and Boninitic Alley) is often difficult because they all show depleted features (Belgrano et al., 2019). For example, the interpretation of Zr/Hf and Nb/Ta ratios (Godard et al., 2006) has become increasingly challenging as more data becomes available leading to increasing overlaps in the compositional fields of V2 units (see Belgrano and Diamond, 2019; e.g., Fig. 13D). Samail lavas show MORB-like Dy/Yb ratios in the Geotimes unit (~1.1; White and Klein, 2014) down to 0.8 in the Boninitic Alley, reflecting the progressive depletion of the more incompatible HREEs in the source throughout time. Concurrently, LREE contents decrease from Geotimes (La/Sm $X = 0.8 \pm 0.1$) to Lasail ($X = 0.6 \pm 0.1$) and later increase in the Tholeiitic ($X = 0.7 \pm 0.2$) and Boninitic (Fig. 13E) Alley units ($X = 0.8 \pm 0.2$) because of contributions from hydrous melting of subduction (Kusano et al., 2017) or metamorphic sole-derived (Ishikawa et al., 2005) components. Clinopyroxene chemistry has also been successfully used to distinguish lava units (Fig. 13F; Alabaster et al., 1982; Gilgen et al., 2014; Belgrano and Diamond, 2019; Belgrano et al., 2019).

Mandoos deposit: The chlorite-altered footwall in Mandoos has higher incompatible element abundances, which places it within the lower range of the Geotimes unit. The low Cr/Y ratios ($X = 0.2 \pm 0.3$) and Zr-Ti-V contents indicate these rocks are more depleted than typical Geotimes. Integrating our data with samples from Gilgen et al. (2014) and Belgrano et al. (2019), the Mandoos footwall samples consistently plot near the Geotimes-Alley boundary, as discussed in Belgrano et al. (2019; Fig. 13A-D). This places the formation of Mandoos at the onset of the postaxial stage.

The hanging-wall lavas have low incompatible element abundances, consistent with the V2 volcanism in Samail (Fig. 10). Additionally, clinopyroxenes fall in the Tholeiitic Alley field, except for a few microlites from Mandoos that plot within the Lasail field. The LREE depletion and flat middle (M)REE-HREE segments in Mandoos hanging-wall lavas are within the reported range of Lasail and Tholeiitic Alley units. Low Cr/Y ($X = 1.6 \pm 2.7$) and high Ti/Zr or Ti/V ($X = 21 \pm 12$) are consistent with a moderately depleted, oxidized source

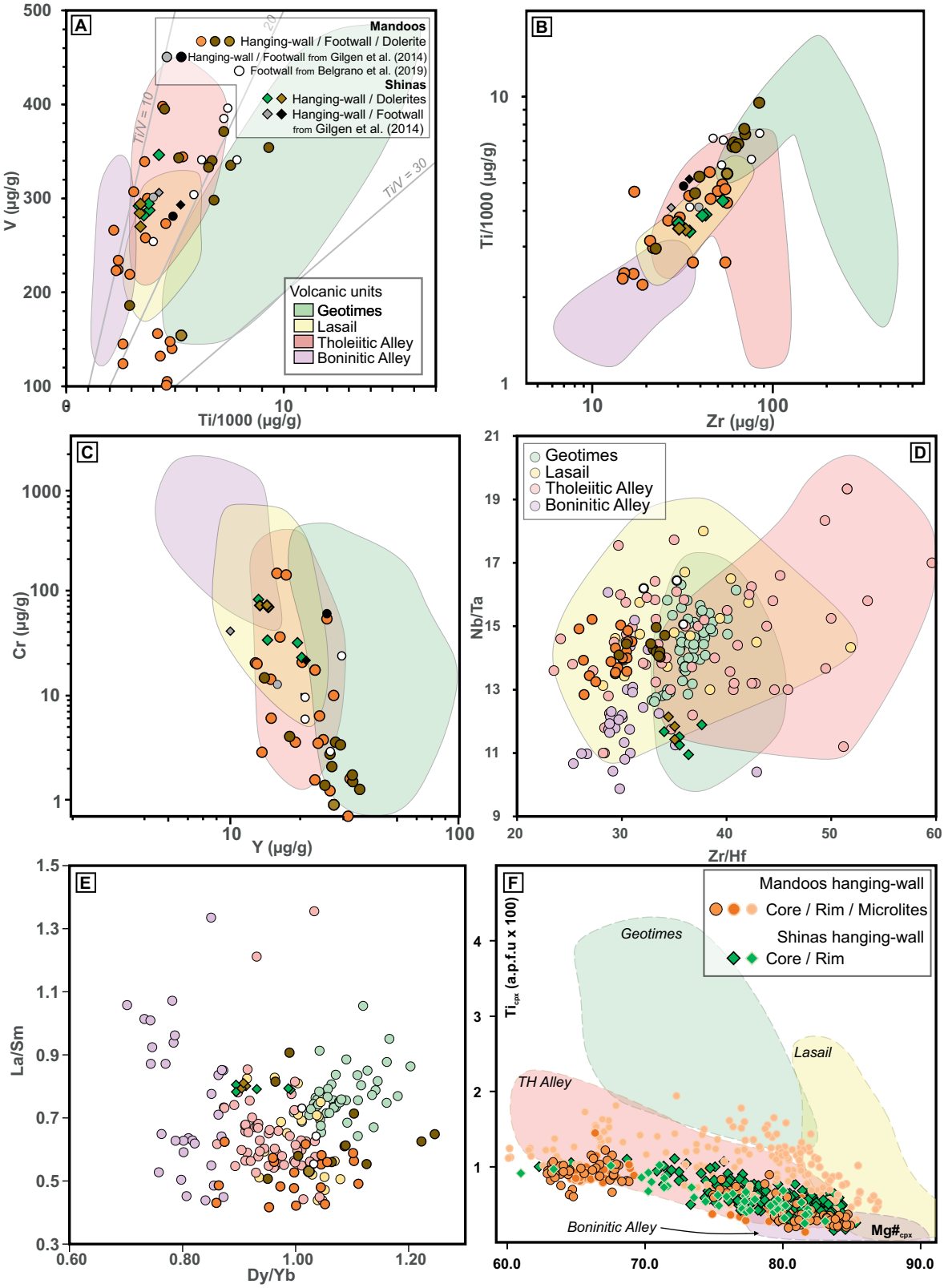

Fig. 13. Discriminant diagrams for the Samail lavas based on whole-rock geochemistry. (A) Ti-V plot after Shervais (1982). (B) Ti-Zr plot after Alabaster et al. (1982). (C) Cr-Y plot after Pearce (1980). (D) Nb/Ta vs. Zr/Hf plot after Godard et al. (2006). (E) La/Sm vs. Dy/Yb diagram using data from Godard et al. (2003, 2006), Kusano et al. (2012, 2014), and Belgrano et al. (2019). Fields in diagrams (A-C) after Belgrano et al. (2019). (F) Clinopyroxene Ti-#Mg discriminant diagram adapted from Alabaster et al. (1982); fields for Oman lavas compiled by Belgrano et al. (2019). Abbreviations: a.p.f.u. = atoms per formula unit Cpx = clinopyroxene, TH = tholeiitic.

zone. The thick hanging-wall sequence shows intercalation of lavas with different degrees of LREE depletion that correlate with decreasing Ti and increasing #Mg in pyroxene, supporting an interfingering of variably depleted lavas. Most discriminant diagrams are inconclusive in distinguishing a Tholeiitic Alley versus Lasail affiliation. Therefore, based on pyroxene chemistry and regional constraints (Belgrano et al., 2019) we assign Mandoos hanging-wall to the Tholeiitic Alley unit, as proposed by Gilgen et al. (2014).

Shinas deposit: Although the Shinas footwall rocks are too altered to preserve magmatic geochemical signatures, it is plausible to infer a Tholeiitic Alley affiliation considering recent geologic mapping (Belgrano et al., 2019).

Clinopyroxenes in the hanging wall fall in the Tholeiitic Alley field (Fig. 13F), consistent with the Dy/Yb-La/Sm diagram that suggests transitional features toward the uppermost Boninitic Alley unit, in agreement with Belgrano et al. (2019). The dilution of source-controlled element abundances (HFSE, HREE) is consistent with the plotting of Shinas lavas at high Cr/Y (X = 4.1 ± 2) and lower Ti-Zr (Fig. 13A, B). The lower Ti/V ratios (X = 12.4 ± 0.6) indicate magma generation within an oxidized, metasomatized source zone. The Shinas hanging-wall lavas lie within the lowest Nb/Ta ratios recorded in Oman lavas at Zr/Hf close to MORB, consistently supporting its transitional character between the Alley units.

Isotopic constraints for regional magmatism: The ε_{Nd_i} for the Tholeiitic Alley unit lies within the range of other Samail rocks (~8–9; Kusano et al., 2017), whereas the Boninitic Alley has a significantly lower range (0.94–5.7; Kusano et al., 2017; Fig. 12). The ε_{Nd_i} values for Mandoos lavas are homogeneous and suggest that the hanging-wall and footwall lavas were extracted from a similar reservoir, within the range of Geotimes, Lasail, and Tholeiitic Alley volcanics or GB1 intrusive rocks. The higher $^{87}Sr/^{86}Sr$ ratios at the lava-ore interface may be explained by focused seawater circulation during cooling of the lavas.

The ε_{Nd_i} values for Shinas volcanic rocks are at the lowermost range of Indian MORB and within the reported range (upper limit) of the Boninitic Alley lavas (Kusano et al., 2017). Such compositions require the involvement of evolved isotopic components, absent in V1 and early V2 magmatism (Godard et al., 2006), which Kusano et al. (2017) related to the incorporation of sediment-derived melts at the source. The occurrence of postobduction Fe-Mn carbonate veins in Shinas hanging wall may significantly increase $^{87}Sr/^{86}Sr$ isotope ratios. However, isotopic exchange of the lavas with seawater under open-source conditions should have resulted in higher $^{87}Sr/^{86}Sr$ shifts compared with the much less altered dikes, which should lie closer to its magmatic $^{87}Sr/^{86}Sr$ ratios. The dolerite dike $^{87}Sr/^{86}Sr$ ratios lie close to many fresh GB2 cumulates, for which highly radiogenic $^{87}Sr/^{86}Sr$ has been attributed to contamination of the source zone by seawater instead of postcrystallization hydrothermal alteration (Benoit et al., 1999).

Our data support a continuous nature for the V1-V2 transition and V2 stage. The Shinas lavas mark the onset of significant modification of the volcanism geochemical features, due to incorporation of evolved (unradiogenic Nd) isotope components in the source zone or en route to the surface.

Genetic model for the Mandoos and Shinas deposits

The Mandoos and Shinas deposits have a semilenticular morphology within a half-graben paleotopography, suggesting their growth was controlled by synvolcanic faults (Figs. 2, 6). These, and other features discussed below, are typical of SMS deposits. Based on the SMS current inventory, it is possible to draw some constraints on the Mandoos and Shinas hydrothermal systems.

The high tonnage (~8 Mt) and size of the Mandoos deposit differs from most VMS deposits in the Samail ophiolite, usually below 3 Mt, and is comparable only to Lasail, Ghuzayn-3 (Gilgen et al., 2014), and the Al Hadeetha deposit (Alara Resources, 2016). The orebody is also larger than most estimates for SMS, with median sizes of ~70,000 t and only eight known deposits above 2 Mt (Hannington et al., 2011). The Mandoos size therefore suggests a protracted period of hydrothermal activity. The tonnage of the Shinas orebody (~0.85 Mt) is comparable to the average VMS deposits in Oman (Gilgen et al., 2014), other ophiolites, or SMS deposits (Hannington et al., 2005; Schardt and Large, 2009). Considering the amount of time estimated to build an ~2 Mt modern SMS such as TAG (5–10 k.y.; Hannington et al., 1998), a deposit such as Mandoos would require at least ~20,000 up to 100,000 years (Schardt and Large, 2009). Shinas should represent a relatively short-lived hydrothermal system that could build up during a period of ~5,000 years.

The different sizes of Mandoos and Shinas could also conceivably result from distinct hydrothermal fluid discharge rates during a broadly similar time span. This would imply distinct permeability conditions at the hydrothermal discharge zones (Schardt and Large, 2009). Considering the constraints imposed by numerical simulations on VMS deposit formation, the smaller Shinas deposit could have formed as a higher-temperature, Cu ± Au-rich system, enabled by lower-permeability conditions. The large area, tonnage, and Zn grades of Mandoos suggest higher-permeability conditions, e.g., along multiple upflow zones where hydrothermal mounds build up under lower-temperature conditions.

In the following sections we discuss the evolution of each system based on the data available for each deposit.

Mandoos deposit: The ores from Mandoos show several features similar to those observed in SMS systems that should represent primary textures preserved since the time of formation of a sulfide mound (Tornos et al., 2015, and references therein), namely (1) pyritized annelid tube-worm burrows, (2) framboidal pyrite, (3) bladed and colloform/banded pyrite and marcasite, and (4) rounded, colloform pyrite-chalcopyrite and other early formed Fe-Cu sulfide intergrowths (Fig. 4). These represent remnants of hydrothermal spires and chimney fragments (Oudin and Constantinou, 1984), occasionally recovered during mining works (R. Willis, pers. commun., 2015).

Pyrite framboids typically develop under low-temperature conditions (Butler and Rickard, 2000), and their formation at Mandoos may have occurred during early stages, while precipitation of banded/colloform pyrite may have taken place during quenching of ore fluids reaching the sea floor (Hannington and Scott, 1988). Marcasite, wurtzite, and Cu-Fe sulfides are observed in association with these early hy-

drothermal structures. Marcasite indicates mixing of acidic hydrothermal fluids with seawater, leading to abrupt pH and redox changes (Murowchick and Barnes, 1986). Wurtzite in Zn-Cu ores is the stable ZnS polytype at lower sulfur fugacity conditions, commonly found in the inner part of sulfide chimneys (Hannington and Scott, 1988).

Mineralized jaspers and Mn jasper fragments are found below the massive sulfides or as fragments within sulfide breccias (Fig. 3H). This suggests that formation of a jasper cap occurred early on, enabling the buildup of the hydrothermal system, until its rupture took place during later ore-forming events (Robertson and Boyle, 1983; Petersen et al., 2014).

During the main ore-forming event, early formed textures were replaced or recrystallized under higher-temperature conditions, including (1) recrystallization of framboidal/colloform pyrite to idiomorphic pyrite, (2) pseudomorphic replacement of wurtzite to sphalerite, (3) replacement of fukuchilite/cubanite by chalcopyrite, often leaving nonstoichiometric, metastable phases (see App. 4C; Zhao et al., 2014), and (4) brecciation and cementation of recrystallized pyrite by chalcopyrite. Sphalerite geothermometry places the main ore stage up to ~390°C. During this stage, chalcopyrite precipitation was dominant, along with pyrite, quartz, and minor sphalerite.

The ore breccias at Mandoos are heterometric, poorly sorted, and often cemented by fine-grained pyrite sands (Galley and Koski, 1997). Although no anhydrite was found, these features argue for mound collapse during the waning stage, leading to retrograde dissolution of anhydrite intergrown with the sulfide assemblages below 150°C (Hannington et al., 1998). The compositional trend of chlorite cementing the ores is typical of diagenetic chlorites (Bourdelle and Cathelineau, 2015) and likely records the transition from hydrothermal to diagenetic temperature conditions during crumbling and lithification of the sulfide breccias. Thinner ores (~1 m) include rounded sulfide clasts, suggesting they may represent mound talus. The trend toward Cu-rich late sulfides (bornite, covellite, spionkopite; Fig. 4C, E, G; App. 4) is attributed to oxidation of chalcopyrite during late seawater influxes, upgrading the Cu grades of the ores. The multiphased quartz veining and late zeolite/carbonate infills may also result from these seawater-dominated hydrothermal fluids, although a relationship with postobduction carbonate veining (as seen in the hanging-wall lavas) cannot be excluded (Richter and Diamond, 2022).

Hydrothermal alteration proximal to the orebody comprises strong silicification with pyrite dissemination and quartz-sulfide veins where the presence of Al-rich phyllosilicates implies intense leaching of the host rock under high water/rock ratios by acidic hydrothermal fluids. These halos are enclosed by intense chloritization with disseminated pyrite and jasper veinlets—a common zoning in active (e.g., TAG) and fossil systems (Galley and Koski, 1997; Hannington et al., 1998; Hannington, 2014). The presence of chlorite- and silica-rich alteration in the open pit and the distal southeast orebody suggests that this deposit represents a large hydrothermal field with more than one sulfide mound. Although hydrothermal alteration in Mandoos is pervasive, the stockwork system is poorly developed, especially compared to Shinas. Several features may have contributed to this: (1) the existence of several feeders (oceanic faults) efficiently focusing fluids directly to the sea floor, (2) no resealing of the deposit following the early rupture of the jasper cap, (3) deposit formation predominantly above the sea floor via sulfide mound growth and collapse, and (4) great water depths preventing boiling of hydrothermal fluids. Deep-seated fossil systems often have incipiently developed stockworks consistent with the great water depths estimated for the Samail volcanism (3–4 km; Belgrano et al., 2021).

Metalliferous sediments are usually found surrounding sulfide mounds and form from hydrothermal fluid exhalation into the seawater column, followed by particle oxidation and deposition (Tornos et al., 2015; Murton et al., 2019). Mandoos sulfide ores are found grading to, and interbedded with, metalliferous sediments characterized by seawater-like REE patterns. Such signatures are the result of oxidation of exhalated sulfide particles into the seawater, from which oxyanions, including REEs, are scavenged (Lode et al., 2015). This implies that the formation of umbers interbedded with the ores was synchronous with the massive sulfide ore-forming processes. Hydrothermal fluids are characterized by high Ba contents, often precipitating Ca and Ba sulfates (Tornos et al., 2015). Our data show that ore-related umbers have higher Ba/Mn than those in the hanging-wall sequence, unrelated to ore-forming processes. Such compositional differences can be further explored to vector hydrothermal activity in the Samail (e.g., Lode et al., 2015).

Submarine weathering of massive sulfide ores may produce ochres via sulfide oxidation and leaching of metals (Murton et al., 2019). At Mandoos, ochres occur overlying or completely replacing massive sulfide ores. The presence of breccia-like textures, sulfide relics, and seawater-like REE patterns suggest that Mandoos ochres resulted from sea-floor weathering of the massive sulfides rather than postobduction weathering. Although atacamite may precipitate from saline groundwaters in hyperarid climates (Reich et al., 2008), the ochre geochemistry and the lack of sulfate phases suggest it formed during seawater-induced oxidation of the massive sulfides (Hannington, 1993). Estimated times for ochre formation in the TAG hydrothermal field is ~20,000 years (Hannington, 1993). Considering that Mandoos ochres are scarce and the massive sulfides are well-preserved, it follows that the Mandoos deposit was quickly covered by the hanging-wall lavas and effectively preserved from further oxidation.

Shinas deposit: Primary ore venting-related textures, like those observed in Mandoos, are seldom preserved at Shinas and are chiefly restricted to faint colloform arrangements in the sulfide clasts. The near-complete recrystallization of the sulfides in the ores strongly suggests that the system evolved under a high-temperature, efficiently focused fluid-flow regime. The occurrence of pyrite laths in the ores suggests pseudomorphic replacement of a pyrrhotite precursor (Fig. 8B), likely preceding the main ore stage (i.e., formation of the matrix-supported breccia + massive ores). Pyrrhotite and high-FeS mol % sphalerite are typical of massive sulfide deposits in sedimented ridges, where reducing conditions are established during interaction of hydrothermal fluids with the host sediments (e.g., Keith et al., 2014). Because Shinas is hosted exclusively within a volcanic sequence, the occurrence of this assemblage suggests that low f_{S_2}-f_{O_2}

conditions prevailed locally. In the early stages, the formation of the jasper I matrix cementing clasts of the footwall volcanic sequence (clast-supported breccia; Fig. 7H) could have limited the system permeability, thus promoting relatively low f_{S_2}-f_{O_2} conditions in the system. Sphalerite thermometry for Fe-rich inclusions places this early stage between 240° and 370°C; it is recorded as quartz-chlorite-pyrite alteration in the clast-supported breccia clasts and left no remarkable record in the jasper matrix cementing the clasts.

The vertical transition between the deep-seated chalcopyrite + pyrite + quartz vein network that coalesces upward to form the matrix of the matrix-supported breccia represents the stockwork of the main ore-forming stage and is typical of proximal discharge areas (Galley and Koski, 1997; Hannington, 2014). The chaotic textures in the shallower matrix-supported breccia unit (Fig. 7F, G) suggest that the onset of the main ore-forming event occurred under a highly dynamic regime. As indicated by the presence of jasper I-bearing clasts in the shallow matrix-supported breccia (Fig. 7F, G) the main ore-forming event was possibly induced by mulltistaged fault displacements and hydrothermal fluids discharge.

The main ore stage led to the intense silicification recorded in the matrix-supported breccia, with complete breakdown of primary igneous phases, and quartz precipitation from the hydrothermal fluids. The abundance of Al-rich phyllosilicates (beidellite) in the matrix-supported breccia indicates intensive leaching under high water/rock ratios by acidic hydrothermal fluids (e.g., Richards et al., 1989; Hannington et al., 1998). The rare chlorite aggregates preserved in the matrix-supported breccia large basalt clasts (Fig. 7F) show higher #Mg relative to the underlying clast-supported breccia where #Mg decreases with depth. This trend of increasing #Mg toward the massive sulfide ore is uncommon (Richards et al., 1989; Gisbert et al., 2022) and may be interpreted as resulting from iron partitioning into sulfides in equilibrium with chlorite or seawater entrainment at the venting site and mixing with the hydrothermal fluids. The final evolutionary stage of the system is represented by the late formation of jasper II, which crosscuts all lithologies and locally overlies the orebody.

The oxidation horizon in Shinas features a downward, steep (~5 m) transition from ochres with seawater-like REE composition, covering much of the deposit. Ochres are underlain by a gossan (Fig. 11C) devoid of seawater REE signatures and are followed by oxidized Cu-rich ores. The ochres attest to seawater-induced oxidation and, therefore, a significant period between the cessation of hydrothermal activity and the covering of the deposit by hanging-wall lavas.

Metal enrichments during hydrothermal and oxidation processes

Primary controls on metal endowments: The first-order constraint to the metal endowment of VMS/SMS systems is the composition of the source zone, which largely reflects the tectonic setting. Metals are mostly added to the hydrothermal fluids via leaching of the source zone, but there is growing evidence for metal inputs related to magmatic volatile degassing, especially in arc settings (e.g., Patten et al., 2020). Fluid composition, intensive variables, and the hydraulics of the hydrothermal system determine how metals are trapped and distributed within a deposit (Schardt and Large, 2009; Monecke et al., 2016).

Zone-refining processes can also control deposit-scale metal zonation. Assay logs (Fig. 11C, D) and correlation factors for Shinas ores (App. 8) show a covariation between Au, Ag, Pb, and As, which increase upward in the sequence, leading to high Au/base metal ratios in the ores. These features—the strong recrystallization of the ores, and the lack of correlations/spatial association between Cu and Zn at the deposit scale—are consistent with efficient zone-refining processes. In Mandoos there is no evidence for significant zone refining: Cu and Zn are not decoupled at the deposit scale, and Au distribution is tightly associated with Cu (Fig. 11; Table 1), suggesting Au was introduced during the main ore-forming stage.

Constraining the fertility of the source zone(s), as well as metal (and S) behavior during the magmatic stages (Patten et al., 2017) requires systematic analysis of chalcophile elements in volcanic suites. Such data are currently lacking for the Samail volcanic rocks; therefore, we perform a comparative assessment of metal enrichments in both deposits using TAG-normalized plots as a proxy for a mafic-hosted system wherein no magmatic volatile fluxes are recorded (Hannington et al., 1998). The plotted average compositions exclude oxidized ores from Shinas and Zn-rich ores from Mandoos, which are assessed separately (Fig. 14A-C); Cu, Zn, and Au mine assay (weighted) averages provide deposit-scale compositional ranges. Both deposits are depleted relative to TAG (0.01–0.8×) in Bi, Ge, Cd, Cr, Co, Ni, and Ga and show similar (0.8–1.6×) enrichments in Cu, Zn, Pb, and Ag, within the range of basalt-hosted VMS/SMS (Monecke et al., 2016). Differences between deposits include higher Te + As + Se ± Sb ± Ga (3–9×) in Mandoos and Au + Tl (1.5×, 82×) in Shinas. Other metals, although not enriched relative to TAG, are also distinct between deposits—namely, higher Mo in Shinas and Se in Mandoos.

Gold grades in Mandoos and Shinas (Table 1) are similar to most VMS deposits in Oman (Gilgen et al., 2014) or Cyprus (Patten et al., 2017), classifying them as gold-poor deposits (Mercier-Langevin et al., 2011). Higher Au grades in Oman are reported for the Rakha and Daris-3A deposits, hosted in the Boninitic Alley unit (Gilgen et al., 2014). SMS systems hosted in arc settings (Herzig and Hannington, 1995; Patten et al., 2020) form through leaching of rocks with higher gold backgrounds or direct magmatic-hydrothermal contributions (Mercier-Langevin et al., 2011; Fuchs et al., 2019). The higher Au + Tl grades in Shinas are consistent with a source with arc-influenced chemical composition (Monecke et al., 2016). The higher Cu grades in Shinas can be explained by its high-temperature evolution, where copper precipitated mostly in the subseafloor. Also, higher average Cu concentrations reported in Tholeiitic Alley lavas relative to Geotimes (X = 61 vs. 39 µg/g; Belgrano et al., 2019) likely favored higher Cu enrichment in Shinas. Source controls on metal endowment are further supported by the differences between the REE patterns of the sulfide ores, which mimic the footwall in each deposit. It follows that the footwall sequence may also represent a major source of metals for the hydrothermal system, in addition to those leached from the reaction zone at the gabbro-dike transition (Hannington, 2014; Richter and Dia-

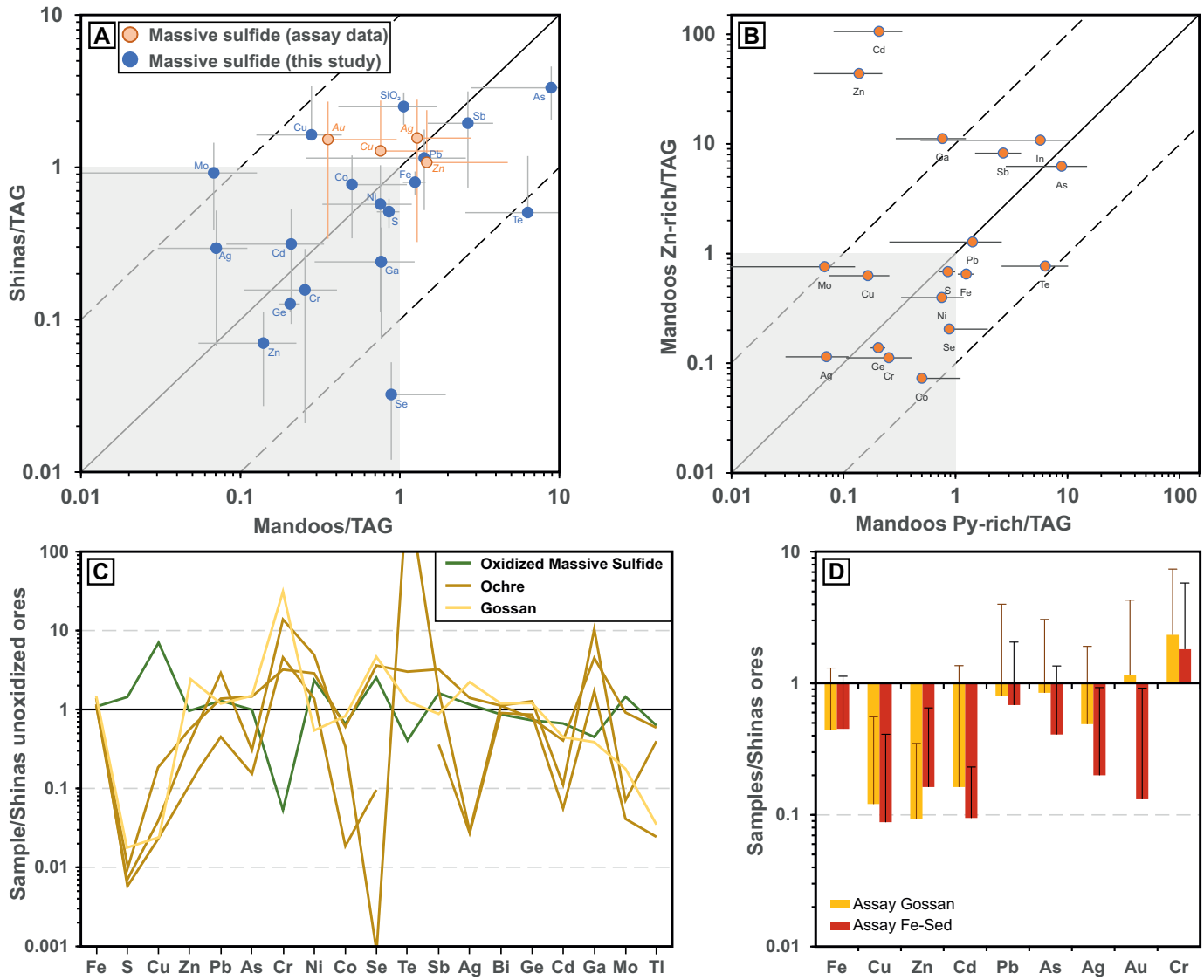

Fig. 14. (A,B) TAG-normalized plots for: (A) average, pyritic sulfide ores from Mandoos (excluding Zn-rich ores) and Shinas (excluding oxidized ores; Table 4) assay data for massive sulfide ores are also plotted (Table 1); and (B) Mandoos Zn-rich vs. Zn-poor (pyritic) ores (Table 4). (C, D) Enrichment/depletion plots for Shinas oxidation profile normalized to the average sulfide ore composition based on (C) inductively coupled plasma-mass spectrometry (ICP-MS) data (Table 4) and (D) mine assay data for massive sulfide ores (Table 1). TAG data from Herzig et al. (1998) and Monecke et al. (2016). Abbreviations: Py = pyrite, Sed = sediment.

mond, 2022). Higher gold grades in other Alley-hosted deposits could be explained by the addition of magmatic fluids and boiling near the sea floor. While high water depths (>3,000 m) estimated for Samail lavas preclude significant hydrothermal boiling (Belgrano et al., 2021), magmatic volatile addition remains to be verified at the deposit scale.

Considering the highly chalcophile character of Cu + Te + Se + Au (Patten et al., 2020), and that Te + Se + Cu indicates high-temperature fluids (Huston et al., 1995; Monecke et al., 2016), the Te-Se enrichment in Mandoos relative to the Cu-Au enrichment in Shinas is unexpected. Zone-refining processes in Shinas cannot account for these differences, since Te + Se are unlikely to be lost from pyrite during zone refining (Huston et al., 1995). Therefore, the higher Te + Se enrichment in Mandoos possibly reflects its basaltic (V1) source area. Assessment of potential magmatic-hydrothermal contributions needs further investigation from isotopic and high-resolution (laser ablation-ICP-MS) techniques. In contrast, Mandoos Zn-rich ores are enriched in Cd + Ga + Mo + Sb but depleted in Te + Se + Co (Se/S 8–13) relative to pyrite-rich ores, which is consistent with their lower-temperature formation.

Effects of oxidation processes: Metal variations for the oxidation profile in Shinas (Fig. 11C) normalized to fresh ores are shown in Figure 14C. The oxidation profile is capped by ochres showing multiple metal enrichments (Te << Se < Pb < Ni < Cr < Ga < Sb), whereas the underlying gossan and oxidized ores show more restricted enrichments in Zn < Cr < Ag < Se and Ni + Se, respectively (Fig. 14C). Furthermore, there is a steep upward Au enrichment in the oxidized ores and gossan (Fig. 11C), whereas deposit-scale assay data confirm sig-

nificant gold grades in the gossans and locally high grades in the Fe sediments (Table 1).

Both subaerial (Boyle, 2003) and seawater-induced oxidation (Herzig et al., 1991; Herzig and Hannington, 1995) can potentially upgrade base metal and gold grades to form chalcocite-rich ores. Ochre formation and related metal enrichments took place during seawater-induced oxidation of the ores. Despite the mineralogical similarities between ochres and gossans, the latter lack REE seawater-derived signatures, clearly resulting from subaerial oxidation. It is thus possible that the spatially associated Au + Cu upgrade in the ores initiated at the sea floor and was further enhanced during postobduction subaerial exposure.

Conclusions

Multiscale evidence gathered in this work shows that the factors controlling the size and metal endowment of the Mandoos and Shinas VMS deposits are volcanostratigraphy, hydrothermal venting style, and late oxidation processes.

The Mandoos deposit is among the largest VMS deposits in Oman (8 Mt at 1.8 wt % Cu, 0.6 wt % Zn, 0.18 g/t Au) and comprises a fault-controlled orebody preserving abundant vent-related features overlying an incipiently developed stockwork. Chlorite-altered halos preserve geochemical magmatic features and envelop quartz-pyrite alteration closer to the orebody. Shinas is a high-grade, ~1-Mt deposit (2.6 wt % Cu, 0.3 wt % Zn, 0.63 g/t Au) within the average size of typical ophiolite-hosted VMS deposits. It comprises a thin, highly recrystallized, quartz-rich massive sulfide lens overlying two pipe-like feeder zones of intensely altered, mineralized, and brecciated footwall.

The differences between these deposits result mostly from distinctive venting styles, possibly controlled by crustal permeability conditions: Mandoos developed along multiple upwelling zones resulting in the formation of a large hydrothermal field. The absence of significant zone refining, the pristine hydrothermal textures, and poorly developed stockwork suggest formation mainly above the sea floor via mound growth and collapse. At Shinas, the pervasive recrystallization of the ores, high Cu/Zn ratios, and occurrence of pyrrhotite pseudomorphs and Fe-rich sphalerite suggest a higher-temperature system evolving from low f_{S_2}/f_{O_2} conditions, locally sealed by jaspers, to a mound growth stage with widespread subseafloor brecciation/replacement and associated zone refining.

Mandoos formed at the onset of the postaxial stage (Geotimes-Tholeiitic Alley transition), and Shinas is hosted within the Alley units. The Shinas hanging-wall lavas have some of the lower ε_{Nd_i} and Nb/Ta ratios in Oman, consistent with extraction from a strongly modified mantle source during the late postaxial stage. Crucially, our data suggest a continuous and transitional nature for the volcanism phases in the Samail ophiolite.

Mandoos is enriched in Te + As + Se ± Zn ± Ga ± Sb relative to Shinas, where higher Cu + Au + Tl ± Mo grades possibly reflect leaching of protoarc-like lavas. REE patterns in the ores mimic the deposit footwall and can be used to constrain its volcanostratigraphic position. This indicates that the footwall sequence can also be an important source of metals, providing a first-order control on the metal enrichments of VMS deposits.

Finally, both deposits show the effects of significant secondary metal enrichment processes related to massive sulfide oxidation, leading to the formation of ores highly enriched in Au-Cu. Seawater-induced oxidation processes resulted in the formation of ochres with seawater-like REE patterns and multiple metal enrichments (Te << Se < Pb < Ni < Cr < Ga < Sb). Copper plus gold upgrading in the ores may have initiated during seawater-induced oxidation and was later enhanced by postobduction subaerial weathering, generating Au-rich gossans.

Acknowledgments

This work was financially supported by Fundação para a Ciência e Tecnologia (FCT) through the Instituto Publico/Ministério da Ciência, Tecnologia e Ensino Superior (I.P./MCTES) through national funds (Programa de Investimentos e Despesas de Desenvolvimento da Administração Central; PIDDAC)–Unidade de Investigação e Desenvolvimento de Base (UIDB/50019/2020). A. Cravinho is supported by a Fundação para a Ciência e a Tecnologia (FCT) Ph.D. Scholarship Program for Research Unit evaluated with excellent (PD/BD/142784/2018) and A.P. Jesus by a Horizon2020 research and innovation program under the Marie Slodowska-Curie grant agreement 894599. We are deeply thankful to Mawarid Mining LLC for the drill cores offered to GUtech, the access to Mandoos pit, and the discussions with Mawarid geologists (Abdulsamad Al-Rawahy, Rob Willis, Cameron Graves) and Haitham Al-Bahrani. We thank the Oman's Public Authority of Mining, namely Ibrahim Al Sawafi, for support with sample export from Oman. The authors are also grateful for the support from GUtech (Frederico Barata, Wakar Akram, Wiekert Wisser, and the late, dear Michaela Bernecker), Daniel Vermond, and Jamie Stewart and for fruitful discussions with C. Patten. This manuscript was significantly improved thanks to the comments, suggestions, and reviews from Tom Belgrano, Larryn Diamond, and Associate Editor Jonathan Cloutier. Careful editorial handling from Larry Meinert is greatly appreciated.

REFERENCES

Alabaster, T., and Pearce, J.A., 1985, The interrelationship between magmatic and ore-forming hydrothermal processes in the Oman ophiolite: Economic Geology, v. 80, no. 1, p. 1–16.

Alabaster, T., Pearce, J.A., and Malpas, J., 1982, The volcanic stratigraphy and petrogenesis of the Oman ophiolite complex: Contributions to Mineralogy and Petrology, v. 81, no. 3, p. 168–183.

Alara Resources, 2016, Maiden ore reserve: Al Hadeetha copper-gold project: www.alararesources.com/irm/PDF/f8e0940d-30cd-4ad5-a52f-89db5ad9bd47/MaidenOreReserveAlHadeethaCopperGoldProject.

Altomare, A., Cuocci, C., Giacovazzo, C., Moliterni, A., and Rizzi, R., 2008, QUALX: A computer program for qualitative analysis using powder diffraction data: Journal of Applied Crystallography, v. 41, no. 4, p. 815–817.

Barrat, J.A., Keller, F., Amossé, J., Taylor, R.N., Nesbitt, R.W., and Hirata, T., 1996, Determination of rare earth elements in sixteen silicate reference samples by ICP-MS after TM addition and ion exchange separation: Geostandards Newsletter, v. 20, no. 1, p. 133–139.

Barrat, J.A., Yamaguchi, A., Greenwood, R.C., Bohn, M., Cotten, J., Benoit, M., and Franchi, I.A., 2007, The Stannern trend eucrites: Contamination of main group eucritic magmas by crustal partial melts: Geochimica et Cosmochimica Acta, v. 71, no. 16, p. 4108–4124.

Belgrano, T.M., and Diamond, L.W., 2019, Subduction-zone contributions to axial volcanism in the Oman-U.A.E. ophiolite: Lithosphere, v. 11, no. 3, p. 399–411, doi: 10.5194/se-10-1181-2019.

Belgrano, T.M., Diamond, L.W., Vogt, Y., Biedermann, A.R., Gilgen, S.A., and Al-Tobi, K., 2019, A revised map of volcanic units in the Oman ophiolite:

Insights into the architecture of an oceanic proto-arc volcanic sequence: Solid Earth, v. 10, no. 4, p. 1181–1217.
Belgrano, T.M., Tollan, P.M., Marxer, F., and Diamond, L.W., 2021, Paleobathymetry of submarine lavas in the Samail and Troodos ophiolites: Insights from volatiles in glasses and implications for hydrothermal systems: Journal of Geophysical Research: Solid Earth, v. 126, no. 7, p. 399–411, doi: 10.1130/L1045.1.
Benoit, M., Polvé, M., and Ceuleneer, G., 1996, Trace element and isotopic characterization of mafic cumulates in a fossil mantle diapir (Oman ophiolite): Chemical Geology, v. 134, no. 1–3, p. 199–214.
Benoit, M., Ceuleneer, G., and Polvé, M., 1999, The remelting of hydrothermally altered peridotite at mid-ocean ridges by intruding mantle diapirs: Nature, v. 402, p. 514–518.
Bourdelle, F., and Cathelineau, M., 2015, Low-temperature chlorite geothermometry: A graphical representation based on a T-R^{2+}-Si diagram: European Journal of Mineralogy, v. 27, no. 5, p. 617–626.
Boyle, D.R., 2003, Preglacial weathering of massive sulfide deposits in the Bathurst mining camp; economic geology, geochemistry, and exploration applications: Economic Geology Monograph 11, p. 689–721.
Butler, I.B., and Rickard, D., 2000, Framboidal pyrite formation via the oxidation of iron (II) monosulfide by hydrogen sulphide: Geochimica et Cosmochimica Acta, v. 64, no. 15, p. 2665–2672.
Dilek, Y., and Furnes, H., 2011, Ophiolite genesis and global tectonics: Geochemical and tectonic fingerprinting of ancient oceanic lithosphere: Bulletin of the Geological Society of America, v. 123, no. 3–4, p. 387–411.
Einaudi, F., Pezard, P.A., Cochemé, J.J., Coulon, C., Laverne, C., and Godard, M., 2000, Petrography, geochemistry and physical properties of a continuous extrusive section from the Sarami Massif, Semail ophiolite: Marine Geophysical Research, v. 21, no. 3–4, p. 387–407.
Ernewein, M., Pflumio, C., and Whitechurch, H., 1988, The death of an accretion zone as evidenced by the magmatic history of the Sumail ophiolite (Oman): Tectonophysics, v. 151, no. 1–4, p. 247–274.
Fleet, A.J., and Robertson, A.H.F., 1980, Ocean-ridge metalliferous and pelagic sediments of the Semail Nappe, Oman: Journal of the Geological Society, v. 137, no. 4, p. 403–422.
Fuchs, S., Hannington, M.D., and Petersen, S., 2019, Divining gold in seafloor polymetallic massive sulfide systems: Mineralium Deposita, v. 54, no. 6, p. 789–820.
Galley, A.G., and Koski, R.A., 1997, Setting and characteristics of ophiolite-hosted volcanogenic massive sulfide deposits: Reviews in Economic Geology, v. 8, p. 221–246.
Gilgen, S.A., Diamond, L.W., Mercolli, I., Al-Tobi, K., Maidment, D.W., Close, R., and Al-Towaya, A., 2014, Volcanostratigraphic controls on the occurrence of massive sulfide deposits in the Semail ophiolite, Oman: Economic Geology, v. 109, no. 6, p. 1585–1610.
Gisbert, G., Tornos, F., Losantos, E., McClenaghan, S., Pons, J.M., Videira, J.C., and Brodbeck, M., 2022, Vectors to ore in replacive volcanogenic massive sulphide deposits of the northern Iberian Pyrite Belt: Major and trace element mineral chemistry: Ore Geology Reviews, v. 147, article 104963.
Godard, M., Dautria, J.M., and Perrin, M., 2003, Geochemical variability of the Oman ophiolite lavas: Relationship with spatial distribution and paleomagnetic directions: Geochemistry, Geophysics, Geosystems, v. 4, no. 6, doi: 10.1029/2002GC000452.
Godard, M., Bosch, D., and Einaudi, F., 2006, A MORB source for low-Ti magmatism in the Semail ophiolite: Chemical Geology, v. 234, no. 1–2, p. 58–78.
Goldstein, S., and Hemming, S., 2014, Long-lived isotopic tracers in oceanography, paleoceanography, and ice-sheet dynamics, *in* Holland, H.D., and Turekian, K.K., eds., Treatise on geochemistry, 2nd ed.: Oxford, Pergamom, p. 453–489.
Goodenough, K.M., Thomas, R.J., Styles, M.T., Schofield, D.I., and MacLeod, C.J., 2014, Records of ocean growth and destruction in the Oman-UAE ophiolite: Elements, v. 10, no. 2, p. 109–114.
Haase, K.M., Freund, S., Beier, C., Koepke, J., Erdmann, M., and Hauff, F., 2016, Constraints on the magmatic evolution of the oceanic crust from plagiogranite intrusions in the Oman ophiolite: Contributions to Mineralogy and Petrology, v. 171, no. 5, doi: 10.1007/s00410-016-1261-9.
Hannington, M., Jamieson, J., Monecke, T., Petersen, S., and Beaulieu, S., 2011, The abundance of seafloor massive sulfide deposits: Geology, v. 39, no. 12, p. 1155–1158.
Hannington, M.D., 1993, The formation of atacamite during weathering of sulfides on the modern seafloor: The Canadian Mineralogist, v. 31, p. 945–956.
——2014, Volcanogenic massive sulfide deposits, *in* Holland, H.D., and Turekian, K.K., eds., Treatise on geochemistry, 2nd ed.: Oxford, Elsevier,, p. 463–488.
Hannington, M.D., and Scott, S.D., 1988, Mineralogy and geochemistry of a hydrothermal silica-sulfide-sulfate spire in the caldera of axial seamount, Juan de Fuca Ridge: The Canadian Mineralogist, v. 26, p. 603–625.
Hannington, M.D., Galley, A.G., Herzig, P.M., Petersen, S., and Charles, K., 1998, Comparison of the TAG mound and stockwork complex with Cyprus-type massive sulfide deposits: Proceedings of the Ocean Drilling Program, Scientific Results, v. 158, p. 389–415.
Hannington, M.D., de Ronde, C.E.J., and Peterson, S., 2005, Sea-floor tectonics and submarine hydrothermal systems: Economic Geology 100th Anniversary Volume, p. 111–141.
Haymon, R.M., Koski, R.A., and Sinclair, C., 1984, Fossils of hydrothermal vent worms from Cretaceous sulfide ores of the Samail ophiolite, Oman: Science, v. 223, no. 4643, p. 1407–1409.
Haymon, R.M., Koski, R.A., and Abrams, M.J., 1989, Hydrothermal discharge zones beneath massive sulfide deposits mapped in the Oman ophiolite: Geology, v. 17, no. 6, p. 531–535.
Herzig, P.M., and Hannington, M.D., 1995, Polymetallic massive sulfides at the modern seafloor; a review: Ore Geology Reviews, v. 10, no. 2, p. 95–115.
Herzig, P.M., Hannington, M.D., Scott, S.D., Maliotis, G., Rona, P.A., and Thompson, G., 1991, Gold-rich sea-floor gossans in the Troodos ophiolite and on the Mid-Atlantic Ridge: Economic Geology, v. 86, no. 8, p. 1747–1755.
Herzig, P.M., Petersen, S., and Hannington, M.D., 1998, Geochemistry and sulfur-isotopic composition of the TAG hydrothermal mound, Mid-Atlantic Ridge, 26°N: Proceedings of the Ocean Drilling Program, Scientific Results, v. 158, p. 47–70.
Huston, D., 2000, Gold in volcanic-hosted massive sulfide deposits: Reviews in Economic Geology, v. 13, p. 401–426.
Huston, D.L., Sie, S.H., Suter, G.F., Cooke, D.R., and Both, R.A., 1995, Trace elements in sulfide minerals from eastern Australian volcanic-hosted massive sulfide deposits; Part I, Proton microprobe analyses of pyrite, chalcopyrite, and sphalerite, and Part II, Selenium levels in pyrite; comparison with delta 34 S values and implications for the source of sulfur in volcanogenic hydrothermal systems: Economic Geology, v. 90, no. 5, p. 1167–1196.
Ishikawa, T., Fujisawa, S., Nagaishi, K., and Masuda, T., 2005, Trace element characteristics of the fluid liberated from amphibolite-facies slab: Inference from the metamorphic sole beneath the Oman ophiolite and implication for boninite genesis: Earth and Planetary Science Letters, v. 240, no. 2, p. 355–377.
Ixer, R.A., Alabaster, T., and Pearce, J.A., 1984, Ore petrography and geochemistry of massive sulphide deposits within the Semail ophiolite, Oman: Transactions of the Institution of Mining and Metallurgy, v. 93, p. B114–B124.
Jones, C.E., and Jenkyns, H.C., 2001, Seawater strontium isotopes, oceanic anoxic events, and seafloor hydrothermal activity in the Jurassic and Cretaceous: American Journal of Science, v. 301, no. 2, p. 112–149.
Keith, M., Haase, K.M., Schwarz-Schampera, U., Klemd, R., Petersen, S., and Bach, W., 2014, Effects of temperature, sulfur, and oxygen fugacity on the composition of sphalerite from submarine hydrothermal vents: Geology, v. 42, no. 8, p. 699–702.
Kusano, Y., Adachi, Y., Miyashita, S., and Umino, S., 2012, Lava accretion system around mid-ocean ridges: Volcanic stratigraphy in the Wadi Fizh area, northern Oman ophiolite: Geochemistry, Geophysics, Geosystems, v. 13, no. 5, p. 1–25.
Kusano, Y., Hayashi, M., Adachi, Y., Umino, S., and Miyashita, S., 2014, Evolution of volcanism and magmatism during initial arc stage: Constraints on the tectonic setting of the Oman ophiolite: Geological Society, London, Special Publications, v. 392, p. 177–193.
Kusano, Y., Umino, S., Shinjo, R., Ikei, A., Adachi, Y., Miyashita, S., and Arai, S., 2017, Contribution of slab-derived fluid and sedimentary melt in the incipient arc magmas with development of the paleo-arc in the Oman ophiolite: Chemical Geology, v. 449, p. 206–225.
Li, C.-F., Li, X., Li, Q., Guo, J., and Li, X., 2011, Directly determining $^{143}Nd/^{144}Nd$ isotope ratios using thermal ionization mass spectrometry for geological samples without separation of Sm-Nd: Journal of Analytical Atomic Spectrometry, v. 26, no. 10, p. 2012–2022.
Li, C.-F., Li, X.-H., Li, Q.-L., Guo, J.-H., Li, X.-H., and Yang, Y.-H., 2012, Rapid and precise determination of Sr and Nd isotopic ratios in geological samples from the same filament loading by thermal ionization mass spectrometry employing a single-step separation scheme: Analytica Chimica Acta, v. 727, p. 54–60.

Li, Y.H., and Schoonmaker, J.E., 2014, Chemical composition and mineralogy of marine sediments, *in* Holland, H.D., and Turekian, K.K., eds., Treatise on geochemistry: Elsevier, p. 1–35.
Lode, S., Piercey, S.J., and Devine, C.A., 2015, Geology, mineralogy, and lithogeochemistry of metalliferous mudstones associated with the Lemarchant volcanogenic massive sulfide deposit, Tally Pond belt, central Newfoundland: Economic Geology, v. 110, no. 7, p. 1835–1859.
MacLeod, C.J., Johan Lissenberg, C., and Bibby, L.E., 2013, "Moist MORB" axial magmatism in the Oman ophiolite: The evidence against a mid-ocean ridge origin: Geology, v. 41, no. 4, p. 459–462.
McCulloch, M.T., Gregory, R.T., Wasserburg, G.J., and Taylor, H.P., 1981, Sm-Nd, Rb-Sr, and $^{18}O/^{16}O$ isotopic systematics in an oceanic crustal section: Evidence from the Samail ophiolite: Journal of Geophysical Research, v. 86, no. B4, p. 2721–2735.
Mercier-Langevin, P., Hannington, M.D., Dubé, B., and Bécu, V., 2011, The gold content of volcanogenic massive sulfide deposits: Mineralium Deposita, v. 46, no. 5, p. 509–539.
Monecke, T., Petersen, S., Hannington, M.D., Grant, H., and Samson, I.M., 2016, The minor element endowment of modern sea-floor massive sulfides and comparison with deposits hosted in ancient volcanic successions: Reviews in Economic Geology, v. 18, p. 245–306.
Mosser-Ruck, R., Pignatelli, I., Bourdelle, F., Abdelmoula, M., Barres, O., Guillaume, D., Charpentier, D., Rousset, D., Cathelineau, M., and Michau, N., 2016, Contribution of long-term hydrothermal experiments for understanding the smectite-to-chlorite conversion in geological environments: Contributions to Mineralogy and Petrology, v. 171, no. 11, p. 1–21.
Murowchick, J.B., and Barnes, H.L., 1986, Marcasite precipitation from hydrothermal solutions: Geochimica et Cosmochimica Acta, v. 50, no. 12, p. 2615–2629.
Murton, B.J., Lehrmann, B., Dutrieux, A.M., Martins, S., de la Iglesia, A.G., Stobbs, I.J., Barriga, F.J.A.S., Bialas, J., Dannowski, A., Vardy, M.E., North, L.J., Yeo, I.A.L.M., Lusty, P.A.J., and Petersen, S., 2019, Geological fate of seafloor massive sulphides at the TAG hydrothermal field (Mid-Atlantic Ridge): Ore Geology Reviews, v. 107, p. 903–925.
Nicolas, A., Bouldier, F., Ildefonse, B., and Ball, E., 2000, Accretion of Oman and United Arab Emirates ophiolite—discussion of a new structural map: Marine Geophysical Research, v. 21, no. 3–4, p. 147–179.
Nicolle, M., Jousselin, D., Reisberg, L., Bosch, D., and Stephant, A., 2016, Major and trace element and Sr and Nd isotopic results from mantle diapirs in the Oman ophiolite: Implications for off-axis magmatic processes: Earth and Planetary Science Letters, v. 437, p. 138–149.
Oudin, E., and Constantinou, G., 1984, Black smoker chimney fragments in Cyprus sulphide deposits: Nature, v. 308, no. 22, p. 349–353.
Palme, H., and O'Neill, H.St.C., 2014, Cosmochemical estimates of mantle composition, *in* Holland, H.D., and Turekian, K.K., eds., Treatise on geochemistry, 2nd ed.: Oxford, Elsevier, p. 1–39.
Palme, H., Lodders, K., and Jones, A., 2014, Solar system abundances of the elements, *in* Holland, H.D., and Turekian, K.K., Treatise on geochemistry, 2nd ed.: Oxford, Elsevier, p. 15–36.
Patten, C.G.C., Pitcairn, I.K., and Teagle, D.A.H., 2017, Hydrothermal mobilisation of Au and other metals in supra-subduction oceanic crust: Insights from the Troodos ophiolite: Ore Geology Reviews, v. 86, p. 487–508.
Patten, C.G.C., Pitcairn, I.K., Alt, J.C., Zack, T., Lahaye, Y., Teagle, D.A.H., and Markdahl, K., 2020, Metal fluxes during magmatic degassing in the oceanic crust: Sulfide mineralisation at ODP site 786B, Izu-Bonin forearc: Mineralium Deposita, v. 55, no. 3, p. 469–489.
Pearce, J.A., 1980, Geochemical evidence for the genesis and eruptive setting of lavas from Tethyan ophiolites: International Ophiolite Symposium, Ministry of Agriculture and Natural Resources, 1979, Cyprus: Proceedings, p. 261–272.
——1996, A users guide to basalt discrimination diagrams: Geological Association of Canada, Short Course Notes, v. 12, p. 79–113.
Petersen, S., Monecke, T., Westhues, A., Hannington, M.D., Gemmell, J.B., Sharpe, R., Peters, M., Strauss, H., Lackschewitz, K., Augustin, N., Gibson, H., and Kleeberg, R., 2014, Drilling shallow-water massive sulfides at the Palinuro volcanic complex, Aeolian island arc, Italy: Economic Geology, v. 109, no. 8, p. 2129–2158.
Reich, M., Palacios, C., Parada, M.A., Fehn, U., Cameron, E.M., Leybourne, M.I., and Zúñiga, A., 2008, Atacamite formation by deep saline waters in copper deposits from the Atacama Desert, Chile: Evidence from fluid inclusions, groundwater geochemistry, TEM, and ^{36}Cl data: Mineralium Deposita, v. 43, no. 6, p. 663–675.
Richards, H.G., Cann, J.R., and Jensenius, J., 1989, Mineralogical zonation and metasomatism of the alteration pipes of Cyprus sulfide deposits: Economic Geology, v. 84, p. 91–115.
Richter, L., and Diamond, L.W., 2022, Characterization of hydrothermal fluids that alter the upper oceanic crust to spilite and epidosite: Fluid inclusion evidence from the Semail (Oman) and Troodos (Cyprus) ophiolites: Geochimica et Cosmochimica Acta, v. 319, p. 220–253.
Rioux, M., Garber, J.M., Searle, M., Kelemen, P., Miyashita, S., Adachi, Y., and Bowring, S., 2021, High-precision U-Pb zircon dating of late magmatism in the Samail ophiolite: A record of subduction initiation: Journal of Geophysical Research: Solid Earth, v. 126, no. 5, p. 1–26.
Robertson, A.H.F., and Boyle, J.F., 1983, Tectonic setting and origin of metalliferous sediments in the Mesozoic Tethys Ocean, *in* Rona, P.A., Boström, K., Laubier, L., and Smith, K.L., eds., Hydrothermal processes at seafloor spreading centers: New York, Springer, New York, p. 595–663, doi: 10.1007/978-1-4899-0402-7.
Ross, P.-S., and Bédard, J.H., 2009, Magmatic affinity of modern and ancient subalkaline volcanic rocks determined from trace-element discriminant diagrams: Canadian Journal of Earth Sciences, v. 46, no. 11, p. 823–839.
Schardt, C., and Large, R.R., 2009, New insights into the genesis of volcanic-hosted massive sulfide deposits on the seafloor from numerical modeling studies: Ore Geology Reviews, v. 35, no. 3–4, p. 333–351.
Shervais, J.W., 1982, Ti-V plots and the petrogenesis of modern and ophiolitic lavas: Earth and Planetary Science Letters, v. 59, p. 101–118.
Staudigel, H., 2014, Chemical fluxes from hydrothermal alteration of the oceanic crust, *in* Holland H.D., and Turekian, K.K., eds., Treatise on geochemistry: Elsevier, p. 583–606.
Tornos, F., Peter, J.M., Allen, R., and Conde, C., 2015, Controls on the siting and style of volcanogenic massive sulphide deposits: Ore Geology Reviews, v. 68, p. 142–163.
Tsuchiya, N., Shibata, T., Yoshikawa, M., Adachi, Y., Miyashita, S., Adachi, T., Nakano, N., and Osanai, Y., 2013, Petrology of Lasail plutonic complex, northern Oman ophiolite, Oman: An example of arc-like magmatism associated with ophiolite detachment: Lithos, v. 156–159, p. 120–138.
White, W.M., and Klein, E.M., 2014, Composition of the Oceanic Crust, *in* Holland, H.D., and Turekian, K.K., Treatise on geochemistry, 2nd ed.: Oxford, Elsevier, p. 457–496.
Yokoyama, T., Makishima, A., and Nakamura, E., 1999, Evaluation of the coprecipitation of incompatible trace elements with fluoride during silicate rock dissolution by acid digestion: Chemical Geology, v. 157, no. 3–4, p. 175–187, doi: 10.1016/S0009-2541(98)00206-X.
Zhao, J., Brugger, J., Ngothai, Y., and Pring, A., 2014, The replacement of chalcopyrite by bornite under hydrothermal conditions: American Mineralogist, v. 99, no. 11–12, p. 2389–2397.

André Cravinho is currently a Ph.D. candidate at the University of Lisbon, Portugal. His project focuses on the genesis of the Neves-Corvo deposit, Iberian Pyrite Belt, Portugal, and aims to better understand the relationship between magmatism and the formation of VMS deposits in the Iberian Pyrite Belt. André received his B.Sc. (2015) and M.Sc. (2017) degrees from the University of Lisbon, with a focus on economic geology and mineral exploration. Most of his research has been on VMS deposits in Portugal and Oman. His research interests also include magmatic and magmatic-hydrothermal processes and associated ore-forming systems.